Enhancement of the Control and Diagnosis of Mechanical Failures of a Drive by Using Load Cycle Identification

Von der Naturwissenschaftlich-Technischen Fakultät

der Universität Siegen

Zur Erlangung des akademischen Grades

Doktor der Ingenieurswissenschaften

(Dr. –Ing.)

genehmigte Dissertation

von

M. Sc. Van Trang Phung

aus Hungyen, Vietnam

1. Gutachter: Prof. Dr.-Ing. Mario Pacas
2. Gutachter: Prof. Dr.-Ing. Steven Liu

Tag der mündlichen Prüfung: 15.12.2017

Acknowledgements

Van Trang Phung

Abstract

This work proposes a new method for the estimation of the load torque in mechatronics systems that are equipped with electrical drives and are characterized by repetitive mechanical cycles. The procedure examined in this research allows an enhancement of the control quality by using a feedforward controller based on the estimated load torque. A harmonic speed controller is also used for improving the velocity control. Its structure can also be integrated in the procedure for the identification of the torque. A second important contribution of this research is the utilization of the estimated load torque for the detection of failures in rolling bearings.

As the demanded load torque in many production machines is repetitive, and as such a periodic function of the shaft angle of the driven machine, it can be represented in terms of Fourier series. Hence, the estimation of the load torque can also be carried out through the calculation of the Fourier coefficients by using either a phenomenological approach or an empirical one. After sufficient online learning on the running mechatronics system at different operating speeds, sets of Fourier coefficients can be obtained by using a sliding-window method. The two methods allow the load torque estimation to be continuously conducted within the whole operational range of the repetitive mechanical system.

The estimated load torque is used for two purposes. First, it is utilized as a compensation signal in a feedforward control scheme to improve the quality of the velocity control by canceling speed oscillations originated from the angle-dependent load torque. Second, it is adapted in a diagnostic procedure for the detection of bearing faults. Since a faulty bearing causes changes on the load torque, its spectrum contains information related to the bearing failures. A diagnostic procedure is proposed that does not require any additional sensors than the usually installed in an electrical drive, and it is capable of detecting the two most commonly found types of bearing faults including single-point defects and generalized roughness fault.

Another approach examined in the frame of this work aims the enhancement of the control quality. This approach relies on the harmonic speed control. For this purpose, two structures for the speed control are proposed. One is known as harmonic speed control, where each harmonic in the spectrum of the speed error is regulated by a

proportional-integral (PI) controller. As previously mentioned, the proposed control structure can also be used for the online calculation of Fourier coefficients in the aforementioned load torque estimation procedure.

The second scheme is called PI-R speed controller, where the conventional PI speed controller is augmented by resonant (R) parts to control specific harmonics of the speed error. As the proposed speed controller separately manipulates harmonics of the speed error, it ensures a good dynamic tracking response of the speed control loop.

An implementation of the control scheme without mechanical encoder, a so called sensorless control scheme, complements the proposed methods. In this way the estimation of the load torque, the detection of the bearing faults, and the harmonic speed control can be carried out without mechanical encoder. A signal injection technique and an enhanced voltage model are used to estimate the rotor position of the driven machine. The utilized machine is a permanent magnet synchronous machine (PMSM) that can be operated in the sensorless field-oriented control scheme in the low-speed as well as in the high-speed regions. A combined angle estimator which is based on the signal injection technique and on the enhanced voltage model was developed for obtaining a smooth speed transition between the two speed regions.

Zusammenfassung

In dieser Arbeit wird eine neue Methode zur online Schätzung des Momentanwertes des Lastmomentes in mechatronischen Systemen vorgestellt. Das Verfahren lässt sich bei-Systemen anwenden, die mit elektrischen Antrieben ausgestattet sind und sich durch periodische mechanische Arbeitszyklen auszeichnen, wie sie in vielen Produktionsmaschinen vorzufinden sind.

Das im Rahmen dieser Arbeit untersuchte Verfahren ermöglicht eine Verbesserung der Regelgüte mithilfe von einer Störgrößenaufschaltung oder einer harmonischen Regelung. Ein zweiter wichtiger Beitrag dieser Forschung ist die Nutzung des geschätzten Lastmoments für die Erkennung von Fehlern bei Wälzlagern. Da das geforderte Lastdrehmoment in vielen Produktionsmaschinen repetitiv ist und deshalb als eine periodische Funktion der Winkelposition von der Antriebsmaschine dargestellt werden kann, ist seine Darstellung als Fourier-Reihe naheliegend. Daher erfolgt die Schätzung des Lastmoments durch die Berechnung der entsprechenden Fourier-Koeffizienten, die entweder nach einem phänomenologischen oder nach einem empirischen Ansatz gewonnen werden können. Nach genügenden online-Messungen bei verschiedenen Arbeitsgeschwindigkeiten des laufenden mechatronischen Systems erhält man Sätze von Fourier-Koeffizienten, die mit Hilfe einer Fensterintegration ermittelt werden. Die beiden Methoden erlauben die Schätzung des Lastmomentes kontinuierlich im gesamten Betriebsbereich des sich wiederholenden mechanischen Systems.

Das geschätzte Lastmoment dient zwei Zwecken: Erstens, kann es als Kompensationssignal in einer Störgrößenaufschaltung zur Verbesserung der Qualität der Geschwindigkeitsregelung verwendet werden. Auf diese Weise wird die durch die pulsierende Last hervorgerufene Welligkeit der Geschwindigkeit unterdrückt. Zweitens, kann es auch in einem Diagnoseverfahren zur Erkennung von Lagerfehlern genutzt werden. Da eine fehlerhafte Lagerung zu Veränderungen des Lastmomentes führt, enthält das Spektrum vom Drehmoment Informationen zu den Lagerschäden. Das vorgeschlagene Diagnoseverfahren erfordert keine zusätzlichen Sensoren, als die ohnehin in einem elektrischen Antrieb Installierten, und ist in der Lage, die zwei am häufigsten anzutreffenden Arten von Lagerfehlern einschließlich singulärer und breitbandiger Fehler zu erkennen.

Ein weiterer im Rahmen dieser Arbeit untersuchter Ansatz zielt auf die Verbesserung der Regelgüte, allerdings nicht mit Hilfe einer Störgrößenaufschaltung sondern vielmehr mit Verwendung einer harmonischen Drehzahlregelung. Zu diesem Zweck werden zwei Strukturen für die Drehzahlregelung vorgeschlagen. Eine, bekannt als harmonische Drehzahlregelung, wo jede Harmonische im Spektrum des Geschwindigkeitssignals mittels eines Proportional-Integral (PI) Reglers unterdrückt wird. Wie die vorgeschlagene Struktur kann ebenfalls für die online-Berechnung, der für die Lastmomentidentifikation notwendigen, Fourier-Koeffizienten verwendet werden.

Die zweite Struktur verwendet einen PI-R Regler, wo bei der herkömmliche PI-Regler durch einen Resonanten (R) Teil ergänzt wird, um die spezifischen Oberschwingungen des Fehlersignals auszuregeln. Da in der Regelstruktur die vorgeschlagenen Drehzahlregler einzelne Oberschwingung separat behandeln, kann der Antrieb dem vorgegebenen Drehzahlprofil sehr gut folgen.

Eine Implementierung der feldorientierten Antriebsregelung ohne Verwendung eines mechanischen Winkelgebers, eine sogenannte sensorlose Regelung ergänzt die vorgeschlagenen Methoden. Auf diese Weise kann die Schätzung des Lastmomentes, die Erkennung von Lagerfehlern und die harmonische Regelung ohne Verwendung eines mechanischen Gebers erfolgen. Eine Signal-Injektionstechnik und ein verbessertes Spannungsmodell werden verwendet, um die Rotorposition der Antriebsmaschine zu ermitteln. Die eingesetzte Maschine ist eine permanenterregte-Synchronmaschine (PMSM), die ohne mechanischen Geber, sowohl im unteren als auch im oberen Geschwindigkeitsbereich, feldorientiert geregelt betrieben werden kann. Eine kombinierte Winkelschätzung anhand der Injektionstechnik und des verbesserten Spannungsmodells wurde entwickelt, sodass ein reibungsloser Übergang zwischen den zwei Bereichen möglich wird.

Contents

Nomenclatures

Symbols

$\lvert r \rvert$	Absolute value
$\lvert \underline{r} \rvert$	Magnitude of a space phasor
B	Magnetic flux density
D	Diode
F	Friction force
g	Gravitational acceleration
K, k	Gain or parameter of the slider crank mechanism
n	Number of ball pairs carrying the load in a bearing
p	Number of pole pairs
S	Power semiconductor switch
S	Sector
s	Laplace variable
i, I	Current
j	Imaginary unit ($j^2 = -1$)
J	Moment of inertia
$\mathrm{Im}\{\underline{r}\}$	Imaginary part
$\mathrm{Re}\{\underline{r}\}$	Real part
d, q	Axis of a rotating coordinate system
L	Inductance
R	Resistance
$sgn()$	Signum function
T	Torque
T	Period
u, U	Voltage
z	Number of balls in a ball bearing
α, β	Axis of a stationary coordinate system
α	Load angle
β	Angle between the two adjacent rolling elements

γ	Angle between the real axis of a fixed coordinate and the real axis of a rotating coordinate
ψ	Flux linkage
φ	Angle between the connecting rod and the potential surface
ω	Angular velocity
λ	Parameter of the slider crank mechanism
μ	Friction coefficient
Δ	Increment of a variable

Matrices/ Vectors

$[\underline{r}]_{UVW}, [\underline{r}]_{\alpha\beta}, [\underline{r}]_{dq}$	Algebraic vectors of a space phasor in the $UVW-$ $\alpha, \beta-; d, q -$coordinate systems, respectively
$[T]$	Transformation matrix

Subscripts

$'e'$	Variables related to the estimated rotating reference frame
$'h'$	Variables and parameters corresponding to a high-frequency
$a_k, b_k, c_k (k \in N)$	Fourier coefficients
d_b, d_c, d_i, d_o	Diameters of the ball, the cage, the inner raceway, and the outer raceway of a ball bearing
e_{cos}, e_{sin}	Signals corresponding to the cosine- and sine- components in the one-dimension synchronous transformation
exc	Parameter of the horizontal slider-crank mechanism
$F_{Coulomb}, F_{stiction}$ $F_{viscous}, F_{Stribek}, F_{total}$	Friction forces
f_{ares}, f_{res}	Anti-resonant and resonant frequencies, respectively
f_{IRF}	Inner raceway characteristic fault frequency
f_{max}	Maximum frequency
f_n	Rotational frequency of the inner raceway
f_{ORF}	Outer raceway characteristic fault frequency
f_R	Characteristic frequency of the resonant part
G_c, G_{crod}	Centers of gravity of the crank and the connecting rod, respectively

$G_{c-id}(s), G_{c-iq}(s)$	Transfer functions of the closed current control loops corresponding to i_d and i_q, respectively
$G_{c-\omega}(s)$	Transfer function of the closed speed control loop
h_c, h_{crod}	Position of the centers of gravity of the crank and the connecting rod with respect to the potential surface
$J_{total}, J_{machine},$ $J_{coupling}, J_{mechanism}$	Total moment of inertia, moment of inertia of the machine, the coupling shaft and the slider crank mechanism
K_c	Coulomb constant
K_{err}	Induction error coefficient
K_{i_i}, K_{i_ω}	Gains of the PI current and speed controllers, respectively
K_R	Gain of the resonant part
K_v	Viscous constant
k_p, k_i	Gains of the PI-controller in the phase-locked loop
L_d, L_q	Inductance in the d- and q- axis of the machine
l	Parameter of the horizontal slider-crank mechanism
m_a, m_b, m_c	Equivalent masses in the horizontal slider-crank mechanism
m_{crank}, m_{slider}	Masses of the crank and the slider, respectively
N	Number of sections in one period 2π
$P_i (i \in N^*)$	Load exerted on a rolling element
P_{max}	Maximum ball load
P_r	Applied radial load torque
r_1, r_2	Parameters of the horizontal slider-crank mechanism
r_d, r_q	Real and imaginary parts of a space phasor in a rotational reference frame
r_U, r_V, r_W	Variables of a space phasor in the UVW coordinate system
r_α, r_β	Real and imaginary parts of a space phasor in a stator-fixed coordinate system
S_t	Stribek coefficient
T_D	Time delay of an inverter
T_{i_i}, T_{i_ω}	Time constants of the PI current and speed controllers, respectively
T_e	Electromagnetic torque
T_g, T_ω, T_f	Time constants of the low-pass filters
T_L, T_{load}	Load torque
$T_{Coulomb}, T_{inertia}$	Load torque components

$T_p, T_{viscous}$	
T_p	Cycle time of the space vector modulation
v_c, v_i, v_o	Tangential velocity of the cage, the inner raceway and the outer raceway
v_{RMS}	RMS value of the vibration velocity
T_σ	Delay due to the inverter and the current low-pass filter
T_s, T_{sd}, T_{sq}	Time constants of the machine
U_{dc}	DC-link voltage
x_U	Phase U
x_V	Phase V
x_W	Phase W
W_0	Weighted coefficient
$W_p, W_{p,crank}, W_{p,crod}$	Potential energy
z_d, z_q	Impedances in the d- and q- axis, respectively
β_{lp}	Bandwidth of a low-pass filter
$\Omega_c, \Omega_i, \Omega_o$	Mechanical angular speed of the cage, the inner raceway, and the outer raceway of a ball bearing
ω_m	Mechanical velocity of the machine
ω_{trans}	Transition angular velocity
γ_m	Mechanical angle of the machine
φ_k	Initial phase of the kth harmonic of the speed error
ψ_p	Pole flux
$\Delta\gamma_m$	Window resolution

Superscripts

$[A]^{-1}$	Inverse of a matrix
$[A]^T$	Transpose of a matrix
x^*	Reference value
x^k	The kth
Δf^{SB}	The width of the sideband
$\hat{u}_h$	The amplitude of the injected high-frequency voltage

Acronyms

AC	Alternating Current

ADC	Analog to Digital Converter
BPF	Band Pass Filter
DAC	Digital to Analog Converter
DC	Direct Current
DFT	Discrete Fourier Transform
DN	Decoupling Network
FOC	Field-Oriented Control
FFT	Fast Fourier Transform
LPF	Low Pass Filter
PC	Personal Computer
PI	Proportional-Integral
$PI-R$	Proportional-Integral Resonant
PLL	Phase-Locked Loop
$PMSM$	Permanent Magnet Synchronous Machine
SPM	Space Phasor Modulation
VSI	Voltage Source Inverter

1 Introduction

1.1 Motivation of the work

The term "mechatronics" was introduced in 1971 by Tetsuro Mori, an engineer of Yaskawa Electric Corporation, to indicate a system that includes a combination of mechanical and electrical parts [1]. The mechanical system, which can perform physical tasks, is driven by electric drives included in the electrical system. In such electric drives, <u>a</u>lternating <u>c</u>urrent (AC) machines are often selected due to their high power density, high efficiency over wide speed and torque ranges, flexible control algorithm and compactness [2]. The interaction between the mechanical system and the electric drives decides the operational qualities of the whole mechatronics system.

Nowadays, mechatronics systems are widely found in production machines and handling processes with a variety of mechanical configurations. The mechanical system is often designed in a unique way aiming to execute particular tasks. The operation of a high automatized production system is based on the distribution of the whole process in a sequential repetitive work schedule. The understanding of the mechanical configuration helps to improve the performance of the mechatronics drive, which then enhances the productivity of the production process.

In terms of control, a frequent requirement for the self-commission of the drive is the permanently updated quantitative information about the mechanical system parameters. In mechatronics systems, the information of the load torque is essential in the process of designing controllers because the load torque acts as a disturbance and needs to be rejected. The adverse effects of the load torque on the control quantities is noticeable especially in case it is changeable like that to be found in mechanical configuration characterized by repetitive cycles. In such systems, the load torque changes periodically according to the position of the shaft of the driven machine and results in oscillations in the speed response. The undesired speed oscillations diminish the quality of the position control loop and also the productivity of the processes. If the information about the load torque is available, it can be used as a compensation signal in the speed control loop to improve the speed response quality. Therefore, the estimation of the load torque is a crucial demand for the control of the mechatronics systems.

All components in a mechatronics system have their own lifetime. The components should be replaced if they do not offer normal functionalities; otherwise, they can cause serious failures. The failures can lead to an interruption of the process, an increase of investment and efforts for repair. To avoid these unwanted effects, condition monitoring should be conducted permanently or periodically to observe the physical states of components in the industrial installation. If a failure is detected in the early stage, the faulty component should be removed before causing an abrupt and costly shutdown.

There are different sources of failures in a mechatronics system, some of them come from the electrical parts while others relate to the mechanical systems. In a review on condition monitoring and fault diagnosis of electrical motors [3], bearing, stator and rotor are the three major components causing failures, where bearing is responsible for up to 40% -50% of all machine malfunctions. Hence, it is necessary to detect the bearing faults in an early stage to ensure a desirable reliability of the electric drives.

The detection of the bearing faults was exhaustively researched and validated by using different methods like those as proposed in [4][5][6]. Some of the available diagnostic methods require additional sensors rather than the usually installed in an electrical drive [5][7], while others can be conducted without demanding additional sensors. It is clear that the use of an additional sensor increases the cost for investment and effort for implementation. Therefore, this work is motivated by developing a new diagnostic method to detect bearing faults without demanding any complementary sensors.

In addition to the requirement of good operational quality, cost-reduction, reliability, and safety are also important factors when they come to the installation and operation of the drives. It is clear that the fewer components used to achieve a specific task, the more robustness of the control system and the greater the benefit-to-cost of the investment. This is one of the reasons why sensorless control has motivated extensive researches. The elimination of the angular transducer used for the measurement of the rotor position reduces installation and cables, decreases the need for maintenance and increases the robustness of the control systems, especially those being used in harsh environments.

This work also discusses how the sensorless control can be adapted for the electric drives to achieve the benefits obtained by the elimination of the angular transducers as already mentioned.

1.2   State of the art

The information about the load torque can be used for either mechanical analysis or performance improvement of mechatronics systems. In [8], it is considered as an input known *a priori* for an identification procedure, from which the mechanical parameters of a two-mass system are determined. Later, these parameters are used in an automatic tuning rule for a two degrees of freedom state-space speed controller. The load torque is also utilized to increase the robustness of the speed controller. In [9], it is used as a compensation signal in a feedforward control scheme designed for an induction machine. It was proven that the conventional PI speed controller augmented with the load torque compensation signal is not affected by the variation of the motor and mechanical parameters.

There are numerous ways to obtain the information about the load torque. The load torque can be measured by using sensors, however, these sensors lead to a higher overall cost and less robustness of the system. Alternatively, it can be estimated by using a disturbance observer whose gain selection can be done by applying a pole-placement method [10][11]. In [10], the authors developed a so-called fast disturbance observer by which the load torque in a two-inertia system can be estimated and used as a compensation signal in the speed control loop. The pole-placement method ensures good estimation accuracy if noise buried in the measurement is low and parameters of the system are well known. Otherwise, the estimation accuracy may be unsatisfactory.

The gain selection for the disturbance observer can also be done by using Kalman filter [12][13]. By this technique, the load torque is considered as a state variable and obtained as an output of the Kalman filter. The Kalman filter method is more robust against the noise in the measurement and the variation in the system parameters than the pole-placement method. However, it has a disadvantage related to the selection of the covariance matrixes, as there is no general rule for the matrixes selection.

As aforementioned, the feedforward control, where the load torque is added to the output of the speed controller, is often used to make the speed response free of negative effects from disturbances. Another approach that can be used to improve the speed response quality is the utilization of a new structure of the speed controller rather than the conventional PI controller. For example, in the case of the two-mass system, a two degrees of freedom state-space speed controller augmented with a pre-filter can be

adapted to give good reference tracking for step and dynamic commands as well as robust and fast load-torque rejection [14].

In the research area pertaining to the detection of bearing faults, there are two main groups of diagnostic methods: with and without the use of acceleration sensor. The sensor is used to measure vibration velocity on the bearing housing or machine frame, whose RMS value can be used to categorize the working condition of the bearing to be one of the four levels according to the ISO 10816 standard [15]. The vibration velocity can be further processed to obtain its spectral content to detect characteristic fault frequencies created by single-point defects or broadband effect generated by the generalized roughness fault [4][5]. This is an accurate and reliable diagnostic method, but it has a big disadvantage associated with the costly sensor.

Without the use of the acceleration sensor, the second diagnostic method relies on either the analysis of stator currents or frequency response. The stator currents based method was proposed and presented in [4]. The authors show that if there is a failure in the bearing of the machine, the air gap flux is modulated and the stator currents are generated at predictable frequencies, which are known as characteristic fault frequencies. By looking at the spectra of the stator currents, a failure in the bearing can be detected if there are considerable harmonics at the characteristic fault frequencies. This method was proven successful by detecting single-point defects.

For the case of generalized roughness fault, the method proposed in [4] is not applicable because it is only able to detect characteristic fault frequencies while the generalized roughness causes broadband effect at unpredictable frequencies. An alternative solution to this problem introduced in [16] uses the autoregressive model of the stator currents. In this method, the stator currents are first filtered to remove most of the significant frequency content unrelated to the bearing faults, then the frequency content of the filtered currents is modeled. A baseline is obtained while a healthy bearing is used. As the bearing health degrades, the deviation in the spectral content from its based line is reflexed in the mean spectral deviation. The value of the mean spectral deviation is used as a fault index. The authors shows that the fault index obtained by using the autoregressive model is a reliable indicator of a developing bearing fault. The autoregressive model method is capable of detecting both generalized roughness fault and single-point defects.

A few years ago, the Institute of Electric Drives and Power Electronics at the University of Siegen developed a diagnostic procedure based on frequency response [6]. This method has been applied in a non-rigid multi-mass system whose frequency response has to be calculated during the commissioning of the plant for reasons of safety and control. The method was proven to be able to detect both single-defects and generalized roughness faults without requiring additional sensors. Since the measurement of the required signals used for the calculation of frequency response can be carried out during the normal operation of the plant, the frequency response based method can serve as an online bearing fault diagnosis.

Due to the benefits resulting from the elimination of the angular transducer as already mentioned in section 1.1, sensorless control today is an interesting research area. Excellent papers concerning the sensorless control of electric drives can be found in literature. In summary, there are two categories of methods for the sensorless algorithm. The first category comprises the methods that model the machine by its state equations and is applicable for medium- and high-speed regions, where the operating speed is larger than 3% the rated speed. This approach is based on fundamental field wave model that can be implemented either open-loop structure, like the stator voltage model, or as closed loop observers [17][18][19]. The second category depends on the saliency in the spatial impedance of the motor; it is suitable for operating the machine at low-speed region and standstill [20][21]. A combined method to obtain a wide-speed range sensorless control was already studied and presented in [22].

1.3 Objectives of this work

This work focuses on the optimum control and diagnosis of mechanical failures of a drive characterized by repetitive cycles of production. One of the objectives of the work is dedicated to the identification of the load torque in such a drive by taking into account the periodicity of inherent to the system. As the load torque changes periodically, it can be represented in the form of Fourier series. After sufficient understanding on the repetitive phenomenon by using an identification-run algorithm, the load torque can be continuously estimated via the calculation of the Fourier coefficients. The estimated load torque can be used as a compensation signal in a feedforward control scheme to ensure the speed response free of oscillations.

Another solution to deal with the speed oscillations is the use of a new structure of the speed controller. The second objective of the work is to develop a so-called harmonic

speed controller where each harmonic in the spectrum of the speed error, i.e. the difference between the reference speed and the actual speed, is manipulated by a PI controller. An alternative scheme is proposed with a PI resonant speed controller, where resonant components are added to the conventional PI speed controller to remove specific harmonics of the speed error.

The third major objective of this work focuses on the detection of bearing faults by the identification of the load torque. As the movement of bearing balls over damaged areas located on one of the four main components of a bearing including an outer raceway, an inner raceway, a cage and balls creates load torque pulses, the spectrum of the load torque contains information associated with the bearing defects. Therefore, the analysis of the load torque can reveal the presence of a bearing failure. The diagnostic procedure does not require complementary sensors and is expected to be able to detect both single-point defects and generalized roughness fault.

The last objective of the work concerns the sensorless control of the drive to complement the proposed methods on the estimation of the load torque, the detection of the bearing faults and the harmonic speed control algorithm. A signal injection technique and an enhanced voltage model based method are used to drive a permanent magnet synchronous machine (PMSM) in the low- and high-speed regions, respectively. A combined field angle estimator from the injection technique and the enhanced voltage model method is developed to obtain a wide speed-range sensorless control.

1.4   Outline of the chapters

The structure of the dissertation is as follows. The motivation and the objectives of the work are described in **Chapter 1**. Theoretical fundamentals of the space phasor, coordinate transformations, mathematical model of a PMSM, two-level voltage source inverter (VSI), and space phasor modulation (SPM) are presented in **Chapter 2**. In **chapter 3**, field-oriented control (FOC) for the PMSM is presented. First, the principle of the FOC algorithm along with the design of the current and speed controllers is summarized. After that, harmonic speed control is presented. **Chapter 4** focuses on the sensorless control of the drive. **Chapter 5** is dedicated to the calculation of the load torque in a horizontal slider-crank mechanism, an example of mechatronics systems characterized by the repetitive phenomenon. From the load torque calculation, two methods for the estimation of the load torque, including a phenomenological method and an empirical one, are proposed. **Chapter 6** deals with the diagnosis of the rolling

bearing faults. The causes and effects of the bearing failures as well as a novel diagnostic procedure are presented. **Chapter 7** contains experimental results that are used to validate the operation of the proposed methods on the load torque estimation, the harmonic speed control, the sensorless control and the detection of the bearing faults.

2 Theoretical Fundamentals

2.1 The space phasor

The history of the space phasor dates back to the 1950's. It was first introduced by K. P. Kovács [23] and then developed further by J. Stepina [24] and I. Serrano [25]. The space phasor is a powerful tool used to describe the working of the three-phase systems, e.g. three-phase AC machines.

Under the assumption that there is no zero component in a three-phase system, i.e. the three instantaneous values $r_U(t)$, $r_V(t)$, and $r_W(t)$ of a three-phase quantity r satisfy

$$r_U(t) + r_V(t) + r_W(t) = 0 \tag{2.1}$$

the quantity r can be represented in a space phasor $\underline{r}(t)$ defined by

$$\underline{r}(t) = \frac{2}{3}\left(r_U(t) + \underline{a} \cdot r_V(t) + \underline{a}^2 \cdot r_W(t)\right) \cdot e^{j\gamma_i} \tag{2.2}$$

where $j^2 = -1$; $\underline{a} = e^{j\frac{2\pi}{3}} = -\frac{1}{2} + j\frac{\sqrt{3}}{2}$; $\underline{a}^2 = e^{j\frac{4\pi}{3}} = -\frac{1}{2} - j\frac{\sqrt{3}}{2}$. $\tag{2.3}$

It is still necessary to define the angle γ_i to complete the space phasor representation (2.2). For stator quantities, the angle $\gamma_i = \gamma_1$ is the position of the axis of the stator winding phase U with respect to a given reference frame. Normally $\gamma_1 = 0$ is chosen, and (2.2) can be rewritten as

$$\underline{r}(t) = \frac{2}{3}\left(r_U(t) + \underline{a} \cdot r_V(t) + \underline{a}^2 \cdot r_W(t)\right) \tag{2.4}$$

The instantaneous value in each phase can be obtained by making projection of the space phasor on the corresponding axis

$$r_U = \text{Re}\{\underline{r}\}; \quad r_V = \text{Re}\{\underline{r} \cdot \underline{a}^{-1}\}; \quad r_W = \text{Re}\{\underline{r} \cdot \underline{a}^{-2}\} \tag{2.5}$$

In the three-dimension coordinate system UVW, the variable r can be represented in the form of a three-element algebraic vector as follows

$$[\underline{r}]_{UVW} = [r_U, r_V, r_W]^T \tag{2.6}$$

Fig 2.1 shows an example of the space phasor $\underline{r}$ in a symmetric three-phase sinusoidal system. In this case, the phase of $\underline{r}$ with respect to the axis of the stator winding phase U is $\varepsilon = 40^0$.
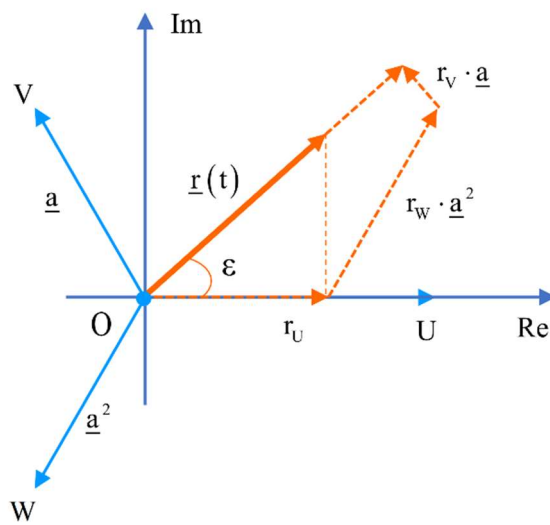

Fig 2.1. Representation of a space phase $\underline{r}$ with $\varepsilon = 40^0$

The space phasor can also be described in two-dimension coordinate systems. The first type of the two-dimension systems is known as α, β stationary coordinate, where the α-axis is in alignment with the U- axis of the UVW coordinate system.

The representation of the space phasor $\underline{r}$ in the stationary coordinate system is as follows

$$\underline{r} = \frac{2}{3}\left(r_U + \underline{a} \cdot r_V + \underline{a}^2 \cdot r_W\right) = r_\alpha + j \cdot r_\beta \tag{2.7}$$

with

$$r_\alpha = \text{Re}\{\underline{r}\} = \text{Re}\left\{\frac{2}{3}\left(r_U + \underline{a} \cdot r_V + \underline{a}^2 \cdot r_W\right)\right\}$$

$$= \text{Re}\left\{\frac{2}{3}\left(r_U + \left(-\frac{1}{2} + j\frac{\sqrt{3}}{2}\right) \cdot r_V + \left(-\frac{1}{2} - j\frac{\sqrt{3}}{2}\right) \cdot r_W\right)\right\} \quad (2.8)$$

$$= r_U$$

and

$$r_\beta = \text{Im}\{\underline{r}\} = \text{Im}\left\{\frac{2}{3}\left(r_U + \underline{a} \cdot r_V + \underline{a}^2 \cdot r_W\right)\right\}$$

$$= \text{Im}\left\{\frac{2}{3}\left(r_U + \left(-\frac{1}{2} + j\frac{\sqrt{3}}{2}\right) \cdot r_V + \left(-\frac{1}{2} - j\frac{\sqrt{3}}{2}\right) \cdot r_W\right)\right\} \quad (2.9)$$

$$= \frac{1}{\sqrt{3}}\left(r_V - r_W\right)$$

The second type of the two-dimension coordinate systems is known as d, q rotating reference frame. As shown in Fig 2.2, the d-axis of the rotating reference frame is shifted by a time-varying angle $\gamma(t)$ from the α-axis of the α, β coordinate system. The d, q reference frame owns a crucial advantage over the UVW- and the α, β-coordinate systems; that is, if the rotational velocity $\dot{\gamma} = d\gamma/dt$ is properly selected, i.e. $\dot{\gamma}$ is identical to the angular velocity of the space phasor $\underline{r}$, the space phasor $\underline{r}$ is observed in steady state as a DC-quantity in the d, q reference frame . As a result, the space phasor $\underline{r}$ can be conveniently manipulated within control schemes. In the d, q coordinate system, the space phasor $\underline{r}$ can be written as:

$$\underline{r}(t) = \text{Re}\{\underline{r}(t)\} + j\,\text{Im}\{\underline{r}(t)\} = r_d(t) + j\,r_q(t) \quad (2.10)$$

It is well worth noting that the space phasor representation as aforementioned is valid for any electrical and magnetic quantities, for example, current i, voltage u, magnetic flux density B, flux linkage ψ, etc.
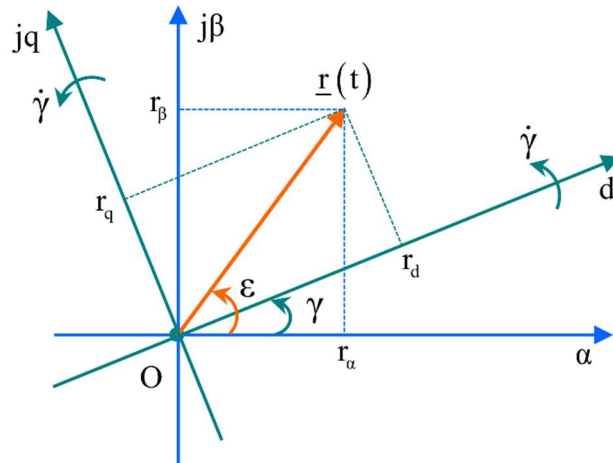
Fig 2.2. Representation of a space phasor $\underline{r}$ in the $\alpha, \beta -$ and the $d, q -$ coordinate systems

2.2 Coordinate transformations

As presented in section 2.1, the space phasor $\underline{r}$ can be described in one of the three coordinate systems: the UVW-, the α, β- and the d, q- coordinate systems. It is necessary to draw transformations between them.

According to (2.8) and (2.9) the transformation from the UVW- to the α, β- coordinate systems is as follows:

$$
\begin{bmatrix} r_\alpha \\ r_\beta \end{bmatrix} = \begin{bmatrix} 1 & 0 & 0 \\ 0 & \dfrac{\sqrt{3}}{3} & -\dfrac{\sqrt{3}}{3} \end{bmatrix} \cdot \begin{bmatrix} r_U \\ r_V \\ r_W \end{bmatrix}
\tag{2.11}
$$

Inversely, the transformation from the α, β - to the UVW- coordinate systems is given by:

$$
\begin{bmatrix} r_U \\ r_V \\ r_W \end{bmatrix} = \begin{bmatrix} 1 & 0 \\ -\dfrac{1}{2} & \dfrac{\sqrt{3}}{2} \\ -\dfrac{1}{2} & -\dfrac{\sqrt{3}}{2} \end{bmatrix} \cdot \begin{bmatrix} r_\alpha \\ r_\beta \end{bmatrix}
\tag{2.12}
$$

The block diagram representation of the transformations between the α, β- and the UVW- coordinate systems is depicted in Fig 2.3.

Fig 2.3. Symbol for the transformation of coordinates between the α, β- and the UVW- coordinates

Fig 2.2 shows that $r_\alpha + j \cdot r_\beta = |\underline{r}| \cdot e^{j\varepsilon}$ and $r_d + j \cdot r_q = |\underline{r}| \cdot e^{j(\varepsilon - \gamma)}$. Therefore, the transformation from the α, β coordinate system to the d, q reference frame is as follows:

$$
\begin{aligned}
r_\alpha + j \cdot r_\beta &= \left(r_d + j \cdot r_q \right) \cdot e^{j\gamma} \\
&= \left(r_d + j \cdot r_q \right) \left(\cos\gamma + j \cdot \sin\gamma \right) \\
&= \left(r_d \cdot \cos\gamma - r_q \cdot \sin\gamma \right) + j \cdot \left(r_d \cdot \sin\gamma + r_q \cdot \cos\gamma \right)
\end{aligned}
\tag{2.13}
$$

Comparing the real and the imaginary terms in (2.13) yields:

$$
\begin{bmatrix} r_\alpha \\ r_\beta \end{bmatrix} = [T] \cdot \begin{bmatrix} r_d \\ r_q \end{bmatrix}
\tag{2.14}
$$

where $[T] = \begin{pmatrix} \cos\gamma & -\sin\gamma \\ \sin\gamma & \cos\gamma \end{pmatrix}$

The inverse transformation of (2.14) is:

$$
\begin{bmatrix} r_d \\ r_q \end{bmatrix} = \begin{bmatrix} \cos\gamma & \sin\gamma \\ -\sin\gamma & \cos\gamma \end{bmatrix} \cdot \begin{bmatrix} r_\alpha \\ r_\beta \end{bmatrix} = [T]^{-1} \cdot \begin{bmatrix} r_\alpha \\ r_\beta \end{bmatrix}
\tag{2.15}
$$

Fig 2.4 shows the symbolical representation of the transformations between the α, β coordinate system and the d, q reference frame.
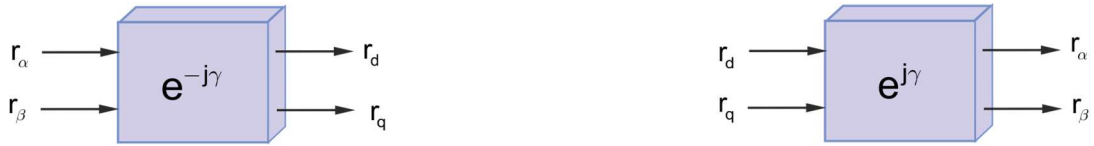
Fig 2.4. Symbol for the transformation of coordinates between the α, β- and the d, q-coordinates

2.3 Mathematical model of the Permanent Magnet Synchronous Machine

In recent years, synchronous machine equipped with permanent magnets has been selected for many industrial servo-drive applications due to the development of magnetic materials, digital signal processing units and power electronics. PMSM brings many advantages, such as high efficiency, high torque density, high overloading capabilities and a good dynamic performance because of low inertia and linear relationship between the electromagnetic torque and the current [26].

In this research work, a surface-mounted PMSM is selected for the electric drive. The mathematical description of the PMSM based on the fundamental field wave is presented in the following section for the purposes of modeling and control of the machine. Since permanent magnets are assembled on the rotor of the PMSM, the modeling relates to the stator quantities, including the stator voltage space phasor $\underline{u}$, the stator current space phasor $\underline{i}$ and the stator flux space phasor $\underline{\psi}$. The stator voltage equation in the α, β-coordinate system is as follows:

$$\underline{u} = R \cdot \underline{i} + \frac{d\underline{\psi}}{dt} \tag{2.16}$$

where R is the resistance of each one of the stator windings.

In the rotating d, q- reference frame, the real axis is chosen as the position of the rotor pole flux, i.e. with an angular displacement γ with regard to the α-axis of the stationary coordinate system as it is shown in Fig 2.5. This d, q rotating frame is known as the rotor-fixed one.
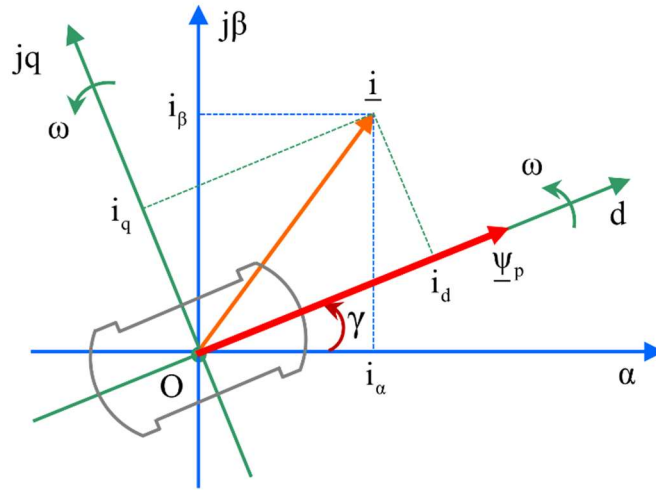
Fig 2.5. Rotor-fixed coordinate system

The stator flux in the rotor-fixed coordinate system is given by:

$$\psi_d = L_d \cdot i_d + \psi_p$$
$$\psi_q = L_q \cdot i_q$$

(2.17)

where ψ_p is the magnitude of the flux produced by the permanent magnets; L_d and L_q are the direct- and quadrature-axis inductances of the machine, respectively.

By combining (2.16) and (2.17), the stator voltage equations of the PMSM in the rotor-fixed reference frame become:

$$u_d = R \cdot i_d + L_d \cdot \frac{di_d}{dt} - \omega \cdot L_q \cdot i_q$$
$$u_q = R \cdot i_q + L_q \cdot \frac{di_q}{dt} + \omega \cdot L_d \cdot i_d + \omega \cdot \psi_p$$

(2.18)

where $\omega = d\gamma/dt$ is the field angular velocity.

The electromagnetic torque is generally calculated by the following equation [27]:

$$T_e = \frac{3}{2} \cdot p \cdot \mathrm{Im}\left(\underline{\psi}^* \cdot \underline{i}\right)$$

(2.19)

where $\underline{i}$ is the stator current space phasor, $\underline{\psi}^*$ denotes the conjugated space phasor of $\underline{\psi}$, and p is the number of pole pairs of the machine.

Since $\underline{\psi} = \psi_d + j \cdot \psi_q$, (2.19) can be rewritten as:

$$
\begin{aligned}
T_e &= \frac{3}{2} \cdot p \cdot \mathrm{Im}\left(\left(\psi_d - j \cdot \psi_q\right) \cdot \left(i_d + j \cdot i_q\right)\right) \\
&= \frac{3}{2} \cdot p \cdot \left(\psi_d \cdot i_q - \psi_q \cdot i_d\right) \\
&= \frac{3}{2} \cdot p \cdot \left(\psi_p \cdot i_q + i_d \cdot i_q \cdot \left(L_d - L_q\right)\right)
\end{aligned}
\tag{2.20}
$$

It can be seen in (2.20) that the electromagnetic torque consists of a main component given by $3/2 \cdot p \cdot \psi_p \cdot i_q$ and a reluctance component defined by $3/2p \cdot i_d \cdot i_q \cdot \left(L_d - L_q\right)$. In a surface-mounted PMSM, the direct and quadrature-axis inductances are approximately equal, $L_d \approx L_q$, since the permeability of the path that the flux crosses between the stator and the rotor is equal all around the stator circumference [28]. Therefore, the reluctance component can be ignored. Equation (2.20) can be rewritten as:

$$
T_e = \frac{3}{2} \cdot p \cdot \psi_p \cdot i_q
\tag{2.21}
$$

The relationship between the mechanical system and the electrical system provides a complete description of the machine.

$$
T_e - T_L = J \cdot \frac{d\Omega_m}{dt} = J \cdot \frac{1}{p} \cdot \frac{d^2\gamma}{dt^2}
\tag{2.22}
$$

where T_L is the load torque; J is the total inertia referred to the shaft of the machine; Ω_m is the mechanical angular velocity of the shaft.
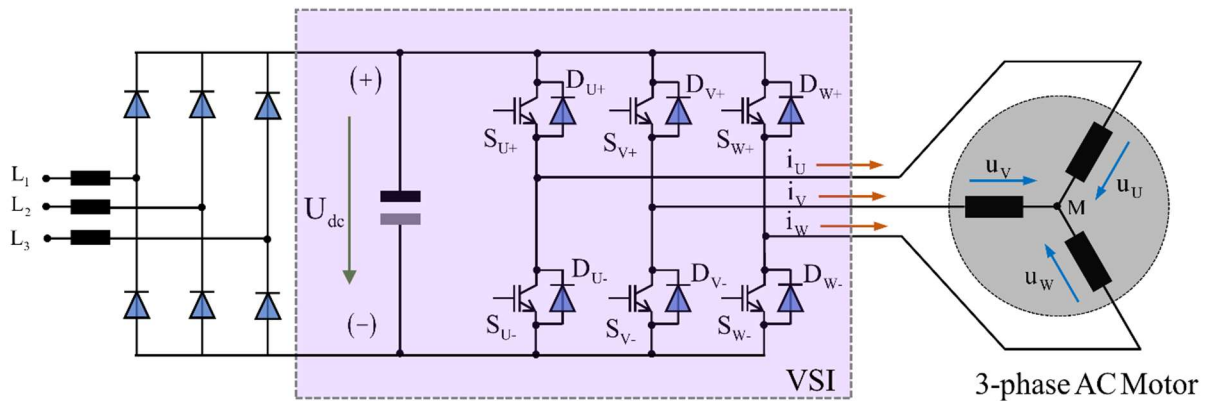
2.4   Voltage source inverter

Fig 2.6. Three-phase power inverter connected to AC-motor

The PMSM is fed by a voltage-source inverter (VSI). Fig 2.6 shows the topology of a two-level VSI. The VSI consists of three half bridges of power semiconductors, commonly Insulated Gate Bipolar Transistors (IGBTs), which are denoted by $S_{U+}|S_{U-}, S_{V+}|S_{V-}, S_{W+}|S_{W-}$ corresponding to phase U, V and W, respectively. The IGBTs have antiparallel free-wheeling power diodes with the notation $D_{U+}|D_{U-}, D_{V+}|D_{V-}, D_{W+}|D_{W-}$. The VSI is fed by a voltage source with the DC-link voltage U_{dc}. The VSI can convert the DC-link voltage into three-phase AC voltages by controlling the states of the power switches. The switching state of each phase is defined as [29]:

$(-)$, if the phase winding is connected to the negative potential, or

$(+)$, if the phase winding is connected to the positive potential of the DC-link voltage.

By combining the possible switching states of each phase, eight voltage space phasors $\underline{u}_0, \underline{u}_1, \underline{u}_2, \underline{u}_3, \underline{u}_4, \underline{u}_5, \underline{u}_6, \underline{u}_7$ can be obtained. The space phasor $\underline{u}_0$, where all outputs are connected to the negative potential, and $\underline{u}_7$, where all outputs are connected to the positive potential, are called zero voltage space phasors because their amplitudes are zero. The six remaining voltage space phasors divide the space into six equal sectors $S_1 \cdots S_6$ as shown in Fig 2.7.
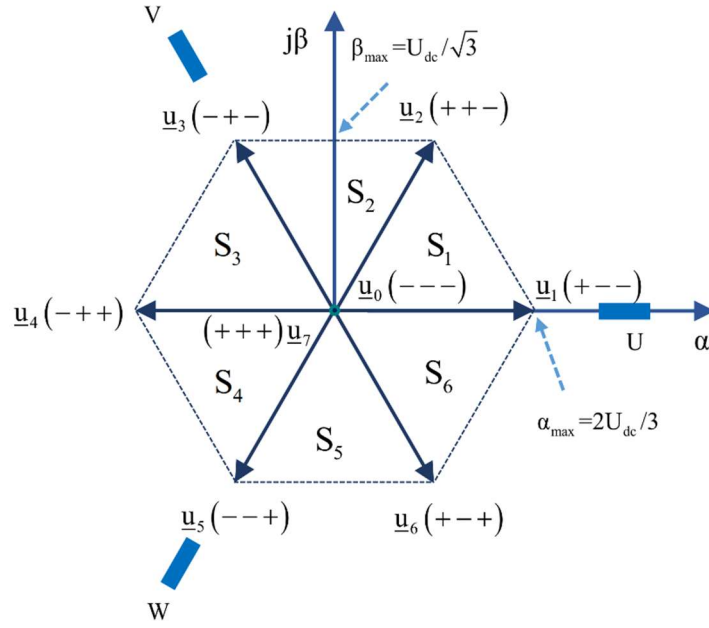
Fig 2.7. Voltage space phasors $\underline{u}_0 \cdots \underline{u}_7$ provided by a two-level VSI

2.5 Space phasor modulation

Some control schemes for electrical machines, which do not directly command the switching-states of a VSI (for example the field-oriented control), need to modulate the control output voltage signals. A common modulation method is the so-called s̲pace p̲hasor m̲odulation (SPM). The space phasor modulation technique applies the space phasor theory to each voltage phasor inside the hexagon-voltage-limits of the VSI.

As presented in section 2.4, six active and two zero voltage space phasors are possible in a two-level VSI. The space phasor modulation can synthetize a voltage space phasor $\underline{u}_s$ located inside one of the six sectors (S_1 to S_6) using the three nearest voltages space phasors of the VSI (two active space phasors and one zero space phasor).

Fig 2.8 shows as an example where the voltage space phasor $\underline{u}_s$ is located in sector S_1, and the generation of the SPM using the nearest voltage space phasors $\underline{u}_1, \underline{u}_2$ and $\underline{u}_0$ or $\underline{u}_7$. So, $\underline{u}_s$ can be calculated by means of:

$$\underline{u}_s = \frac{T_1}{T_p} \cdot \underline{u}_1 + \frac{T_2}{T_p} \cdot \underline{u}_2 + \frac{T_{0,7}}{T_p} \cdot \underline{u}_{0,7} \tag{2.23}$$

$$\frac{T_1}{T_p} = \frac{2}{\sqrt{3}} \frac{|u_s|}{U_{dc}} \sin\left(\frac{\pi}{3} - \gamma\right) \tag{2.24}$$

$$\frac{T_2}{T_p} = \frac{2}{\sqrt{3}} \frac{|u_s|}{U_{dc}} \sin(\gamma) \tag{2.25}$$

$$T_{0,7} = T_p - T_1 - T_2 \tag{2.26}$$

where $T_p = \frac{1}{f_s}$ with f_s is the switching frequency; T_1/T_p, T_2/T_p and $T_{0,7}/T_p$ are the duty cycles of the respective space phasors $\underline{u}_1$ and $\underline{u}_2$, and $\underline{u}_0$ or $\underline{u}_7$.
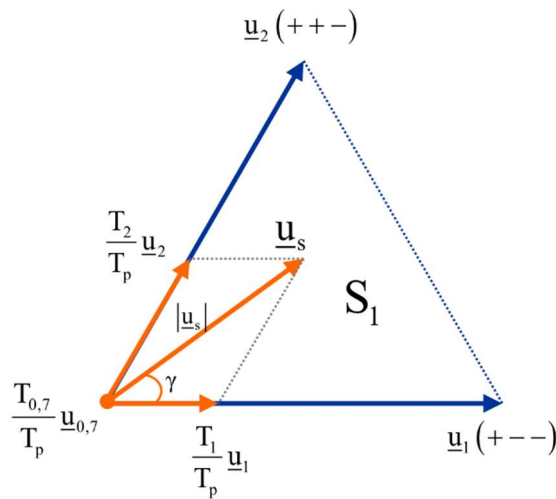

Fig 2.8. Example for the space phasor modulation

The selection of the zero phasors $\underline{u}_0$ or $\underline{u}_7$ is carried out by taking into account the switching losses; that is, the favorable sequence is to change every IGBT pair only one time within a period as depicted in Fig 2.9.

The procedure of the SPM is similar in the other five sectors. Details on the SPM can be found in [27].
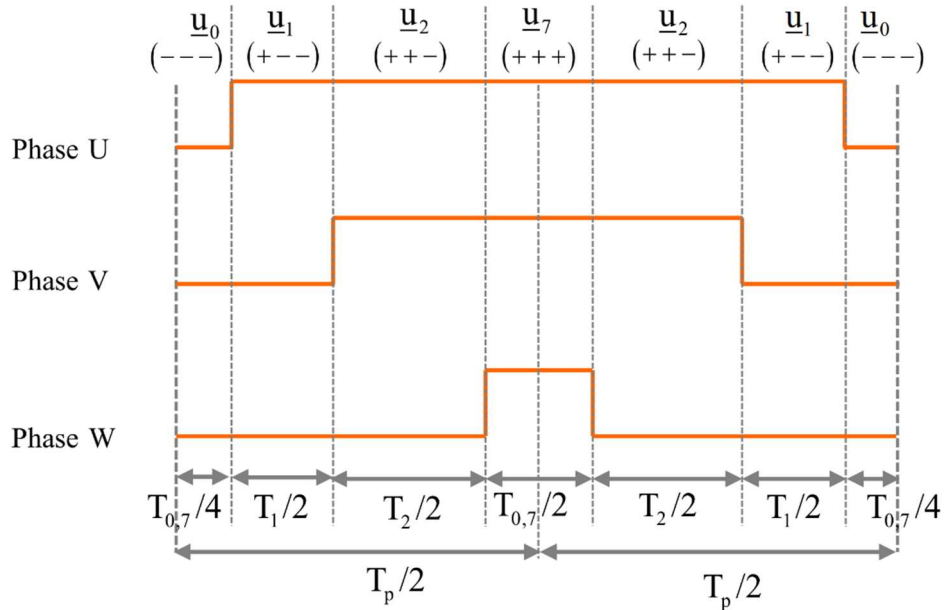
Fig 2.9. Switching patterns of the SPM in sector S_1

2.6 Summary of the chapter

This chapter provided the fundamental concepts used for this work. The chapter started out by introducing the space phasor, then the coordinate transformations. The mathematical model of a PMSM utilized in the electric drive was derived with respect to the fundamental field wave. The PMSM was supplied by a two-level VSI whose topology as well as a control algorithm technique known as the space phasor modulation were also presented.

3 Field-oriented Control of the Permanent Magnet Synchronous Machine

3.1 Field-oriented control of PMSM

Torque, or force, is the basic quantity of all drive applications. Torque depends on a product of a current and magnetic flux. The magnetic flux can be generated by permanent magnets or by a flux producing current. In separately excited DC machines, the control of the torque and the flux producing currents is independent and decoupled. As a result, very simple control algorithms were developed for the operation of separately excited DC machines installed in high performance quality systems already in the last century. However, separately excited DC machines have become less attractive in recent decades due to the considerable disadvantages associated with their brushes, sizes and maintenances, resulting in the widespread use of AC machines. In terms of control, it is difficult to have a complete separation between the torque and the flux producing current components in an AC machine like that in a DC machine, because the AC machine has multi-phase windings and voltage systems. The purpose of the field-oriented control (FOC) is to reestablish the decoupling of the torque and the flux producing current components. The theory of the FOC was introduced in [30][31]. Currently, the FOC is one of the most commonly used control algorithms in AC drives.

3.1.1 Principle of the field-oriented control

The principle of the FOC of a PMSM relies on the advantages obtained by representing electric and magnetic space phasors of the PMSM in the rotor-fixed coordinate system. As explained in section 2.3, if the real component of the stator current is kept at zero, the electromagnetic torque given by $T_e = 3/2 \cdot p \cdot \psi_p \cdot i_q$ is directly proportional to the permanent pole-flux ψ_p and the imaginary component i_q of the stator current. Because ψ_p is a constant, the electromagnetic torque can be controlled via the current component i_q.

The mathematical description of the PMSM given by (2.18) shows that the stator voltages in the d- and q- axis are coupled without the exception of standstill ($\omega = 0$). In fact, the voltage coupling has some drawbacks in particular for the design of current controllers. A more favorable rewritten form of (2.18) is commonly used by defining u_{d0} and u_{q0} as follows [32]:

$$u_{d0} = u_d + \omega \cdot L_q \cdot i_q = R \cdot i_d + L_d \cdot \frac{di_d}{dt}$$

$$u_{q0} = u_q - \omega \cdot L_d \cdot i_d - \omega \cdot \psi_p = R \cdot i_q + L_q \cdot \frac{di_q}{dt}$$

(3.1)

A possible realization of a FOC-scheme according to the mathematical model (3.1) is depicted in Fig 3.1. Normally, the control is operated with a zero flux producing current component, i.e. $i_d^* = 0$.
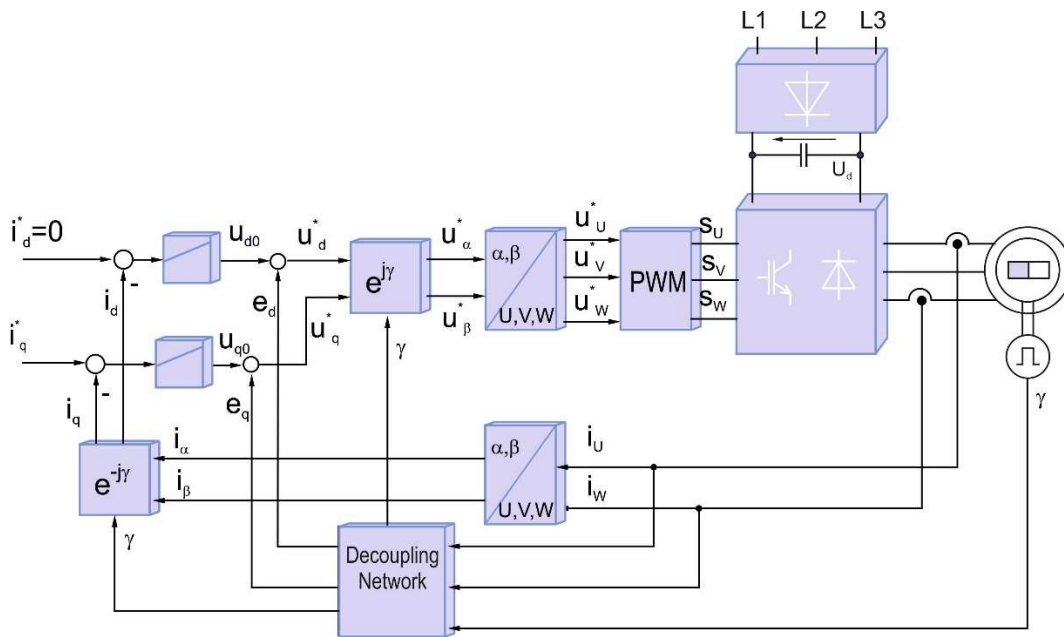

Fig 3.1. Field-oriented control scheme for the PMSM

The actual measured phase currents are transformed to the rotor-fixed coordinate system and are compared to the corresponding demanded current components. The rotor position angle γ is used for the coordinate transformations and can be obtained by utilizing either an angular transducer installed in the machine or an angle observer. With regard to the d- and q- axis separation, the output voltages u_{d0} and u_{q0} from the PI current controllers are considered as fictive quantities as shown in Fig 3.1, from which the decoupling circuit depicted in Fig 3.2 calculates the real demanded voltage components u_d and u_q. The demanded stator voltage phasor is then generated by the space phasor modulation technique and is fed to the stator windings.
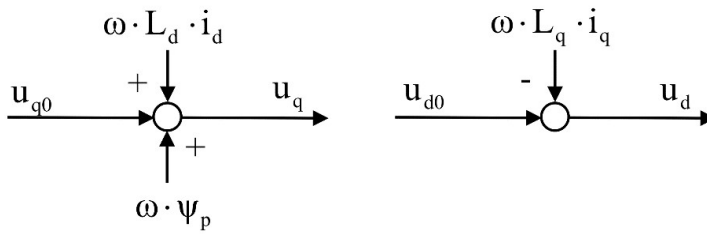
Fig 3.2. Decoupling network (DN)

The FOC of the PMSM can be extended with a superimposed velocity control as depicted in Fig 3.3. The control has cascade structure with two control loops. The outer cascade allows for the control of the actual mechanical speed Ω_m to track the reference speed Ω_m^*, where a PI speed controller is usually adopted. The speed controller has a moderate sampling rate and determines the reference torque producing current component i_q^*.
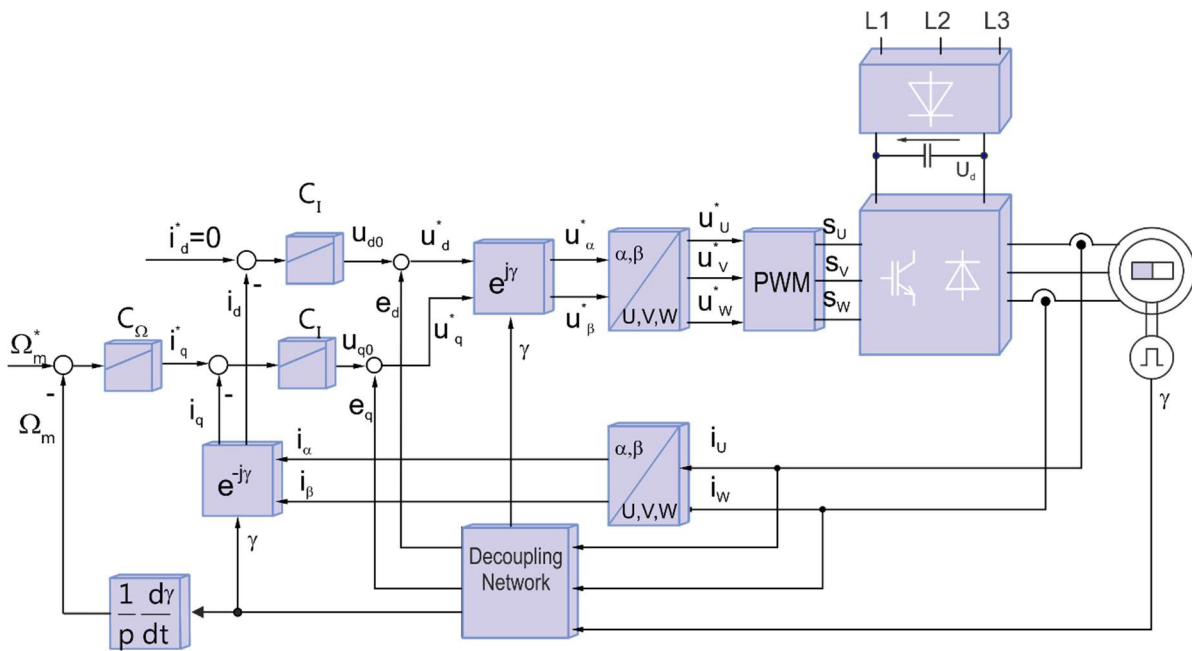

Fig 3.3. Block diagram of the velocity control of the PMSM with an under-layered FOC

3.1.2   Current control loop

As shown in Fig 3.1, the FOC scheme of the PMSM contains the current control loop. Fig 3.4 depicts the simplified current control loop using PI current controllers. The modeling of the PMSM is based on equation (3.1). The transfer functions from the stator

current components on the d- and q-axis to the corresponding voltage components by assuming a perfect decoupling of the equation (3.1) are given by:

$$\frac{i_d(s)}{u_{d0}(s)} = \frac{K_e}{T_{sd} \cdot s + 1} \; ; \quad \frac{i_q(s)}{u_{q0}(s)} = \frac{K_e}{T_{sq} \cdot s + 1} \tag{3.2}$$

where $K_e = 1/R, T_{sd} = L_d/R$, $T_{sq} = L_q/R$; s is the Laplace variable.
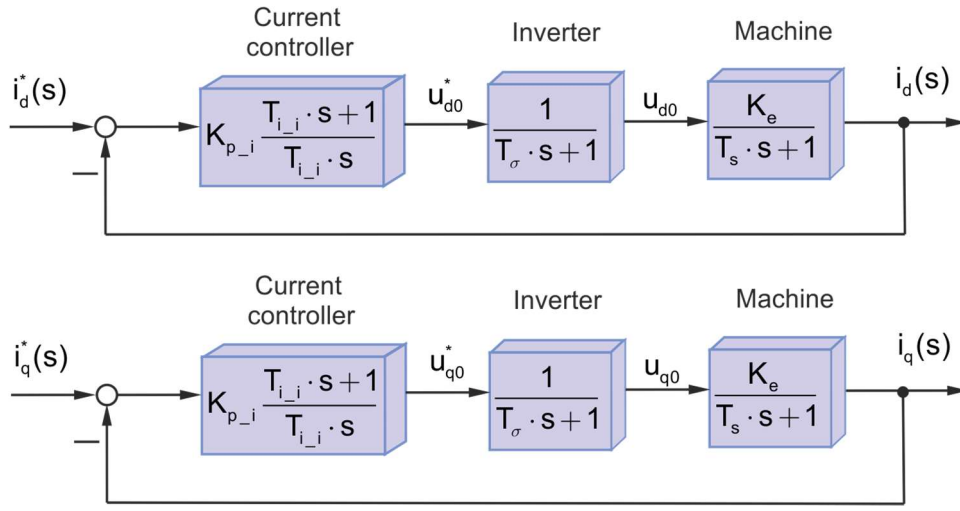

Fig 3.4. Block diagram of the current control loop

As aforementioned, the inductances on the d- and q-axis at fundamental frequency of the surface-mounted PSMS are identical, i.e. $L_d = L_q = L_s$. The transfer functions (3.2) can be rewritten as:

$$\frac{i_d(s)}{u_{d0}(s)} = \frac{i_q(s)}{u_{q0}(s)} = \frac{K_e}{T_s \cdot s + 1} \tag{3.3}$$

where $T_s = L_s/R$ is the dominant time constant of the machine, i.e. the stator time constant determined by the inductance and resistance of the machine.

The inverter is modeled as a first order lag with a time constant $T_\sigma = T_{sampling}$, where $T_{sampling}$ is the sampling time of the control algorithm. The transfer functions from the reference voltages to the actual voltages can be expressed as follows:

$$\frac{u_{d0}(s)}{u_{d0}^*(s)} = \frac{u_{q0}(s)}{u_{q0}^*(s)} = \frac{1}{T_\sigma \cdot s + 1} \tag{3.4}$$

The terms u_{d0}^*, u_{q0}^* are the reference voltages on the d- and q- axis, respectively; u_{d0}, u_{q0} are the generated voltages on the d- and q- axis by the inverter.

The parameters of the PI controllers can be calculated according to the magnitude optimum criterion, by which the PI controllers are designed to keep the closed-loop transfer functions close to one in as large bandwidth as possible. The parameters of the current controller are calculated as [33] :

$$
\begin{aligned}
T_{i\_i} &= T_e \\
K_{p\_i} &= \frac{L_s}{2 \cdot T_\sigma}
\end{aligned}
\tag{3.5}
$$

where K_{p_i} and T_{i_i} are the gain and the time-constant of the PI current controllers.

By designing the current controllers in this way, the transfer function from the reference current to the actual current can be approximated as a first order lag:

$$
G_{c\_id}(s) = G_{c\_iq}(s) = \frac{1}{2 \cdot T_\sigma^2 \cdot s^2 + 2 \cdot T_\sigma \cdot s + 1} \approx \frac{1}{2 \cdot T_\sigma \cdot s + 1}
\tag{3.6}
$$

where $G_{c-i}(s)$ and $G_{c-iq}(s)$ are the transfer functions of the closed current control loop corresponding to i_d and i_q, respectively.

3.1.3 Speed control loop

In the cascade structure, the speed control loop is superposed to the current control loop. By assuming the approximation model of the current loop given in (3.6), the speed control loop can be simplified as illustrated in the block diagram in Fig 3.5.
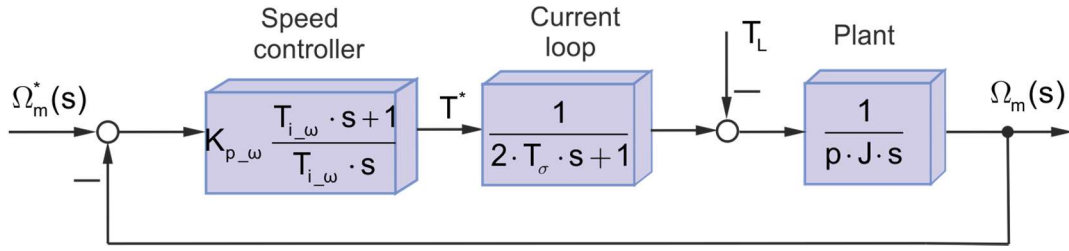
Fig 3.5. Block diagram of the speed control loop

To ensure both the speed reference tracking and the load torque rejection in electric drives, symmetric optimum criterion delivers a commonly used design [34]. It is carried out by finding the maximum damping of the control system, which corresponds to the largest phase margin of the open loop transfer function. Accordingly, the parameters of the PI speed controller are given by [35]:

$$T_{i\_\omega} = 8 \cdot T_\sigma$$
$$K_{p\_\omega} = \frac{J}{4 \cdot T_\sigma}$$

(3.7)

where J is the moment of inertia of the mechanical load referred to the shaft of the machine.

The transfer function of the closed speed control loop is then defined by:

$$G_{c\_\omega}(s) = \frac{\Omega_m}{\Omega_m^*} = \frac{1 + 8 \cdot T_\sigma \cdot s}{1 + 8 \cdot T_\sigma \cdot s + 32 \cdot T_\sigma^2 \cdot s^2 + 64 \cdot T_\sigma^3 \cdot s^3}$$

(3.8)

3.2 Harmonic speed control

The function of the speed control loop is to ensure that the velocity of the drive follows its reference speed and rejects disturbances from the load torque. The conventional PI speed controller designed based on the symmetric optimum criterion can handle normal technical demands, for example, a constant or step-change of the load torque. Yet in cases where the drive is required to accomplish specific shapes of the load torque, the conventional speed controller may provide inadequate reference speed tracking capability [14][36]. In such cases, the structure of the speed controller should be modified in order to ensure the demanded operational quality.

In many industrial installations, the electric drives are desired to be able to work with repetitive mechanical systems, where the load torque changes periodically according to the position of shaft of the driven machine. Because of the variable load torque, the velocity control loop is always working in dynamic modes. The changing load torque yields oscillations in the velocity even for a constant reference value. To cope with this problem, harmonic speed control can be utilized. The idea behind the design of the harmonic speed controller is that each harmonic in the spectrum of the speed error is manipulated by an individual controller. In principle, there are two different approaches for achieving this objective. One is the use of a resonant controller and the other is the utilization of a PI controller. These two solutions will be explained in details in the following section.

Without the loss of generality, the theoretical analysis is conducted under an assumption that the driven machine completes one cycle of the load torque in one revolution.

3.2.1 Proportional-integral resonant speed control

Proportional-integral resonant (PI-R) controllers are widely used for current control loop in grid-connected systems with the aim of harmonic compensation [37][38][39]. In such systems, the current responses contain considerably undesirable harmonics, which are multiples of the grid frequency. These undesirable harmonics have to be canceled. For this purpose, one possible solution is to use a resonant component whose transfer function is given by:

$$F_R(s) = K_R \cdot \frac{s}{s^2 + \omega_R^2} \tag{3.9}$$

where K_R is the gain and ω_R is the characteristic frequency of the resonant component.

As depicted in Fig 3.6 the velocity control loop of the PMSM is modified, where the conventional PI controller is augmented by the resonant part connected in parallel [40]. For simplicity, one resonant component with $\omega_R = 10\pi \ rad/s$ is taken into account. In this case, the transfer function of the PI-R speed controller is:

$$G_{\omega-PIR}(s) = \frac{T^*(s)}{\Delta\Omega_m(s)} = K_{p\_\omega} \frac{T_{i\_\omega} \cdot s + 1}{T_{i\_\omega} \cdot s} + K_R \cdot \frac{s}{s^2 + \omega_R^2} \tag{3.10}$$

As the speed oscillations come from the angle-dependent load torque, the PI-R speed controller is considered in terms of disturbance rejection. The closed-loop transfer function from the load torque T_L to the mechanical speed Ω_m is:

$$G_{1L}(s) = \frac{\Omega_m(s)}{T_L(s)} = \frac{-num_1(s)}{den_1(s)}$$

$$num_1(s) = 2T_{i\_\omega}T_\sigma \cdot s^4 + T_{i\_\omega} \cdot s^3 + 2T_{i\_\omega}T_\sigma \omega_R^2 \cdot s^2 + T_{i\_\omega}\omega_R^2 \cdot s$$

$$den_1(s) = 2pJT_{i\_\omega}T_\sigma \cdot s^5 + pJT_{i\_\omega} \cdot s^4 + \left(2pJT_{i\_\omega}T_\sigma\omega_R^2 + K_{p\_\omega}T_{i\_\omega}\right) \cdot s^3 +$$
$$\left(pJT_{i\_\omega}\omega_R^2 + K_{p\_\omega} + K_R T_{i\_\omega}\right) \cdot s^2 + K_{p\_\omega}T_{i\_\omega}\omega_R^2 \cdot s + K_{p\_\omega}\omega_R^2$$

(3.11)

The closed-loop transfer function from the load torque T_L to the mechanical speed Ω_m corresponding to the conventional PI speed controller is

$$G_{2L}(s) = \frac{\Omega_m(s)}{T_L(s)} = \frac{-num_2(s)}{den_2(s)}$$

$$num_2(s) = 2T_{i\_\omega}T_\sigma \cdot s^2 + T_{i\_\omega} \cdot s$$

$$den_2(s) = 2pJT_{i\_\omega}T_\sigma \cdot s^3 + pJT_{i\_\omega} \cdot s^2 + K_{p\_\omega}T_{i\_\omega} \cdot s + K_{p\_\omega}$$
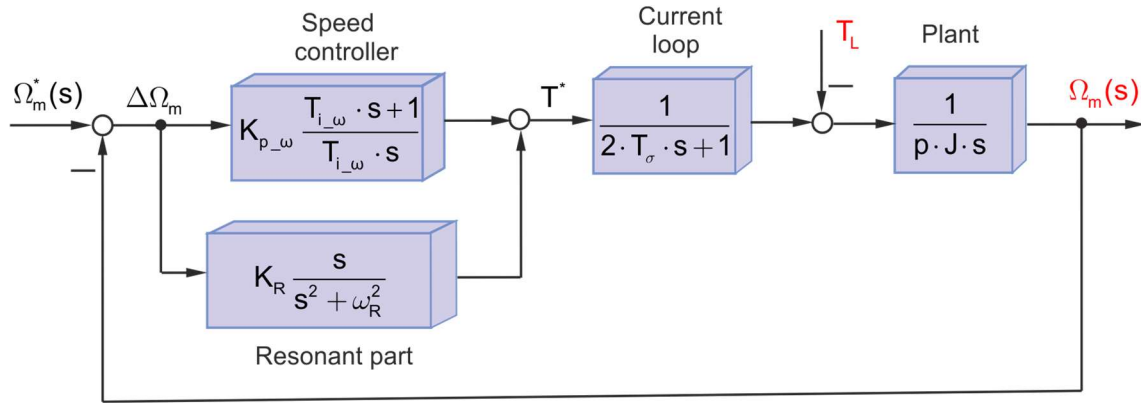
(3.12)

Fig 3.6. Block diagram of the speed control loop with a PI-R controller

The Bode diagrams of $G_{1L}(s)$ and $G_{2L}(s)$ are shown in Fig 3.7 and Fig 3.8, respectively. The frequency response from the load torque to the mechanical speed is used for the purpose of theoretical analysis. The magnitude of the harmonic at frequency ω in the spectrum of the mechanical speed can be defined according to (3.11) .

$$\left|\Omega_m(j\omega)\right| = \left|G_{1L}(j\omega)\right| \cdot \left|T_L(j\omega)\right|$$
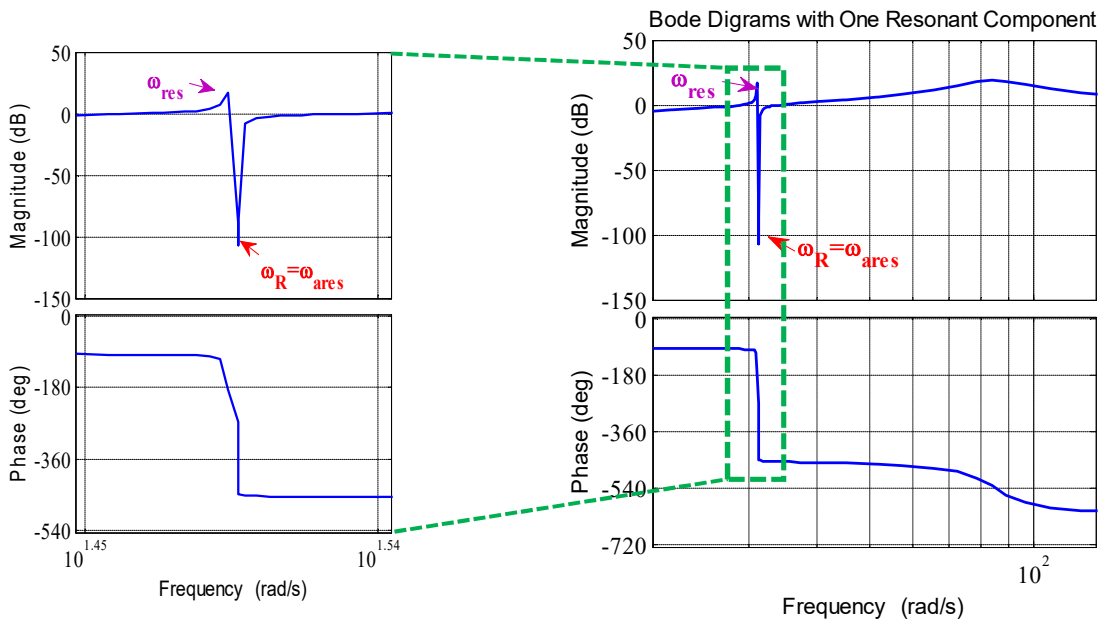
(3.13)

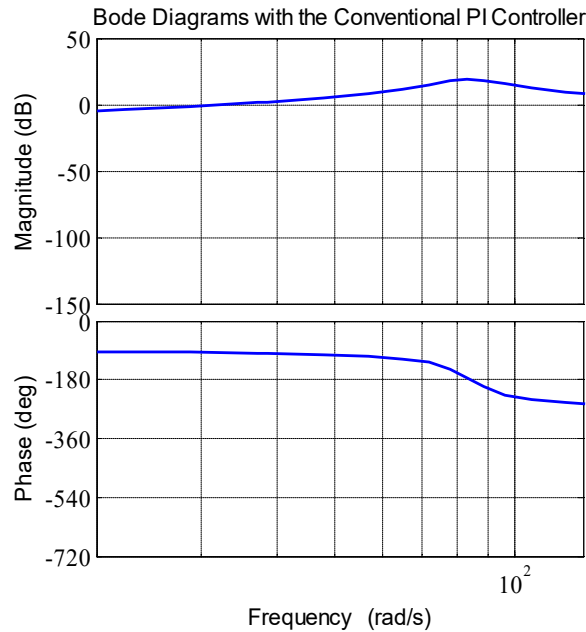Fig 3.7. Bode diagrams of $G_L(s)$ with PI-R speed controller

Fig 3.8. Bode diagrams of $G_L(s)$ with the conventional speed controller

Fig 3.7 shows that the PI-R speed controller results in very low magnitude $|G_{1L}(j\omega)|$ at ω_R. This means that the harmonic corresponding to ω_R in the spectrum of the load torque has low effect on the mechanical speed Ω_m. Frequency ω_R can be regarded as an anti-resonant frequency of the speed control loop ($\omega_{ares} = \omega_R$).

In the Bode diagram, it is observed that the PI-R controller has a side effect as it introduces a new resonant frequency (ω_{res}), at which the magnitude of the closed-loop transfer function increases considerably compared to that of the conventional PI speed controller. However, the effects of the new resonant frequency on the speed control loop can be neglected. The reason is, in spite of the increase of $|G_{1L}(j\omega)|$ at $\omega = \omega_{res}$, the magnitude $|T_L(j\omega)|$ at ω_{res} is small as ω_{res} is not a dominant harmonic of the load torque. Thus, according to (3.13) the magnitude of the mechanical speed Ω_m is not significant at ω_{res}. The phase diagrams corresponding to the two controllers differ from each other only at the anti-resonant frequency ω_R.

The next step concerns the design of the resonant filter, which is characterized by the characteristic frequency ω_R and the gain K_R. While ω_R directly depends on the velocity of the driven machine, K_R should be chosen relatively high but within stable limit to ensure small steady-state speed error. To get an insight into the effect of K_R to the speed control loop, the root-locus of the transfer function $G_{1L}(s)$ from the load torque to the mechanical speed with a PI-R speed controller is plotted and analyzed. The characteristic equation of $G_{1L}(s)$ given by

$$0 = den_1(s) = 2pJT_{i\_\omega}T_\sigma \cdot s^5 + pJT_{i\_\omega} \cdot s^4 + \left(2pJT_{i\_\omega}T_\sigma\omega_R^2 + K_{p\_\omega}T_{i\_\omega}\right) \cdot s^3 + $$
$$\left(pJT_{i\_\omega}\omega_R^2 + K_{p\_\omega} + K_R T_{i\_\omega}\right) \cdot s^2 + K_{p\_\omega}T_{i\_\omega}\omega_R^2 \cdot s + K_{p\_\omega}\omega_R^2$$

(3.14)

can be rearranged in the conventional from (3.15) for the root-loci plot.

$$1 + \frac{K_R \cdot B(s)}{A(s)} = 0$$

(3.15)

where

$$B(s) = s^2$$

$$A(s) = \frac{1}{T_{i\_\omega}}\left[\begin{array}{l}2pJT_{i\_\omega}T_\sigma \cdot s^5 + pJT_{i\_\omega} \cdot s^4 + \left(2pJT_{i\_\omega}T_\sigma\omega_R^2 + K_{p\_\omega}T_{i\_\omega}\right) \cdot s^3 \\ + \left(pJT_{i\_\omega}\omega_R^2 + K_{p\_\omega}\right) \cdot s^2 + K_{p\_\omega}T_{i\_\omega}\omega_R^2 \cdot s + K_{p\_\omega}\omega_R^2\end{array}\right]$$

Fig 3.9 depicts the root-locus of the speed control loop with a PI-R speed controller with respect to the change of K_R. Equation (3.14) shows that the characteristic equation has the order of five, therefore there are five segments of the root loci as shown in Fig 3.9 (a). The dominant poles are on segment 1 and segment 2, which are located near the

imaginary axis. A zoom of segment 1 and segment 2 is shown in Fig 3.9 (b). The gain $K_R = 28.4$ is selected to ensure a desirable damping of the speed control loop.
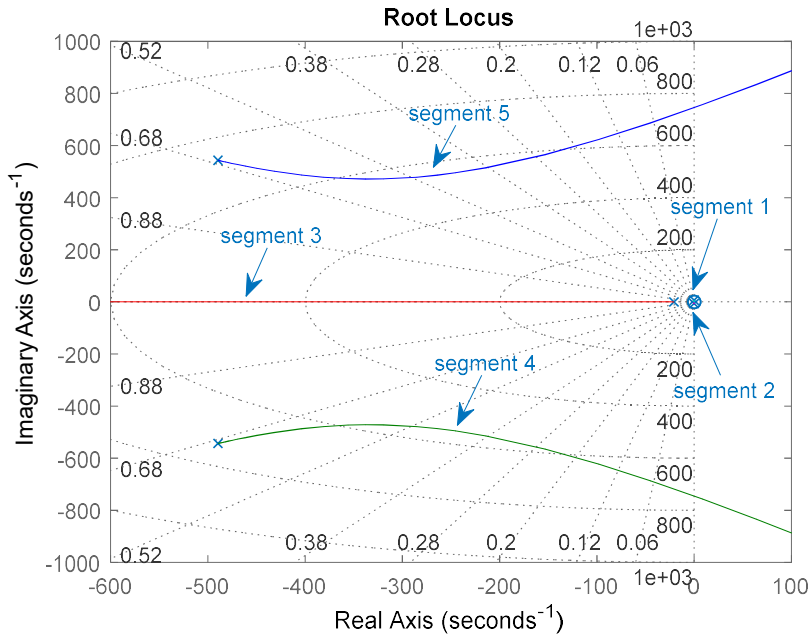
(a)
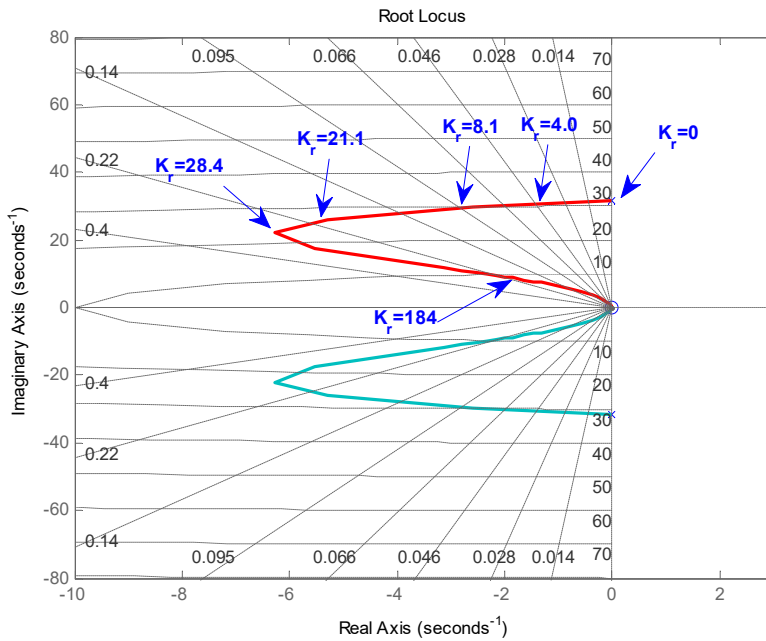
(b)

Fig 3.9. Root-loci of the speed control loop with regard to the gain K_R: a) the whole root-locus; b) the dominant roots lying on segment 1 and segment 2
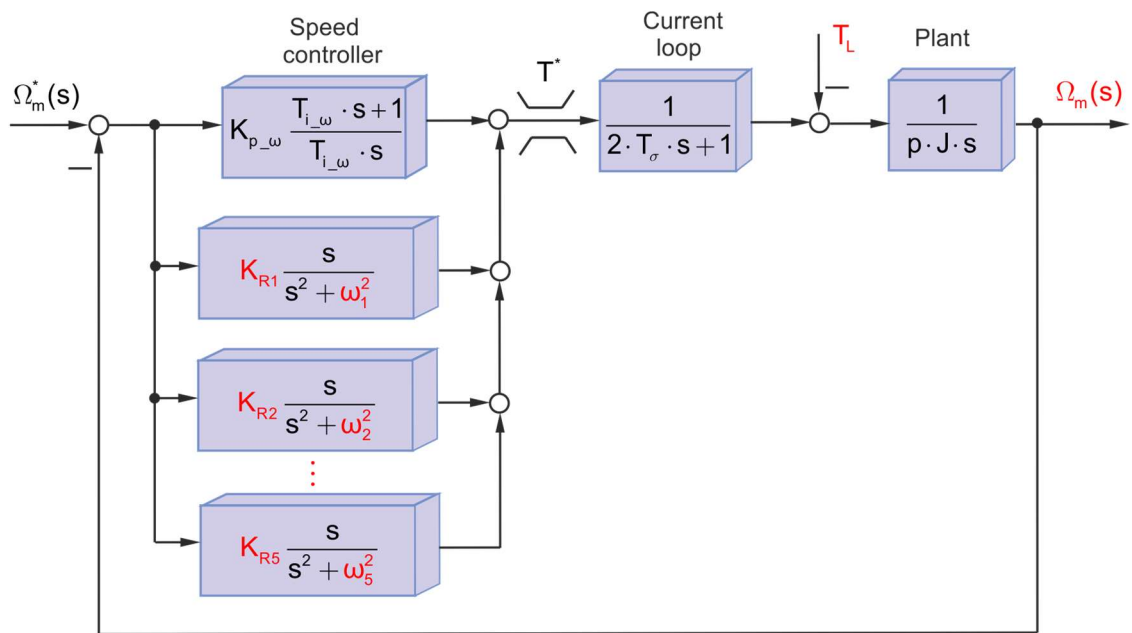
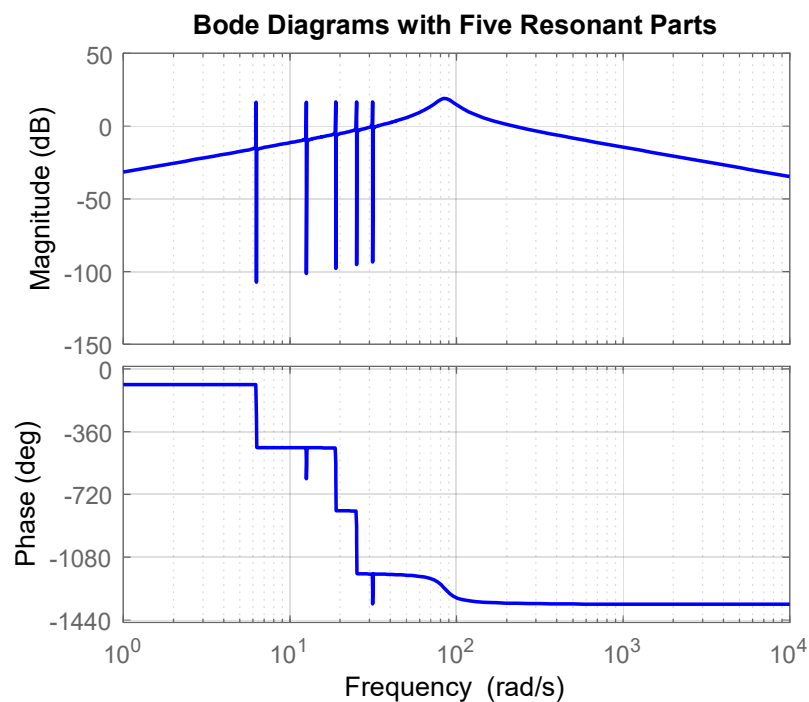Fig 3.10. Block diagram of the peed control loop with five resonant blocks

Fig 3.11. Bode diagram of the speed control loop with five resonant blocks

Usually the periodic disturbances contain more than a single harmonic. Therefore, additional resonant components can be implemented in parallel, where each one is dedicated to a harmonic contained in the spectrum of the disturbance load. Fig 3.10

depicts the speed control loop with a PI-R speed controller, where harmonic up to the 5th of the speed error is considered. The Bode diagram of $G_{1L}(s)$ in this case is shown in Fig 3.11. The design of each resonant filter can be conducted separately by the root-loci analysis as already presented.

It is important to mention again that the characteristic frequency ω_R of each resonant filter depends on the mechanical speed Ω_m. Hence, the PI-R speed controller has to be implemented as an adaptive one that changes characteristic frequency ω_R according to the variable speed.

3.2.2   Harmonic speed control

Another solution to deal with specific harmonics appeared in the controlled variables is the use of a harmonic controller. The harmonic controller was developed for different applications, such as power factor control for a boost rectifier [41] or current control for a transverse flux machine [42]. In the present work, the harmonic controller is applied to the speed control loop [40]. Unlike the PI-R speed controller, where each harmonic is controlled by a resonant filter, in the new approach, each harmonic is manipulated by a PI-controller.

The harmonic controller is based on a single-phase synchronous reference frame control [41]. Since one revolution of the driven machine completes one cycle of the load torque, oscillations in the velocity are related to the mechanical position angle γ_m of the driven machine. Thus, the speed error, which is the difference between the speed response Ω_m and a constant reference speed Ω_m^*, is a periodic function of rotor angle γ_m. The representation of the speed error in terms of infinite Fourier series is given by equation (3.16).

$$e\left(\gamma_m\right) = \Delta\Omega_m = \Omega_m^* - \Omega_m = \sum_{n=0}^{\infty} e_n \sin\left(k \cdot \gamma_m + \varphi_k\right) \tag{3.16}$$

where e is the speed error; e_k and $(k \cdot \gamma_m + \varphi_k)$ are the magnitude and phase of the kth harmonic of the speed error e.

The idea of the harmonic controller is now that the error signal is modulated with the frequencies of the harmonic that have to be rejected by the control. This procedure corresponds to the transformation of each harmonic to a frame of coordinates in which

it becomes constant. Two PI-controllers manipulate each harmonic of the modulated signal and the manipulated variables are demodulated and are added for the calculation of the reference torque. Fig 3.12 shows the structure of the kth controller designed for the kth harmonic of the speed error.
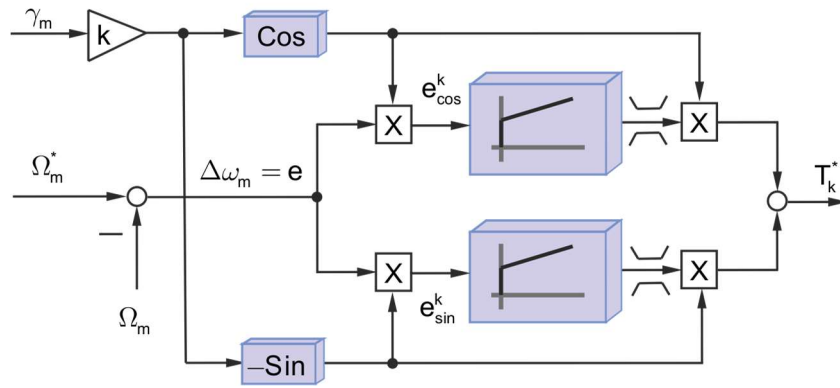

Fig 3.12. Speed controller for the kth harmonic

The transformation results in two signals e_{cos}^{k} and e_{sin}^{k} as follows [42]:

$$e_{cos}^{k} = \cos(k \cdot \gamma_m) \cdot e = \cos(k \cdot \gamma_m) \cdot \sum_{n=0}^{\infty} e_n \cdot \sin(n \cdot \gamma_m + \varphi_n)$$

$$= \frac{1}{2} e_k \cdot \sin(\varphi_k) + \frac{1}{2} \cdot e_k \cdot \sin(2 \cdot k \cdot \gamma_m + \varphi_k) + \tag{3.17}$$

$$+ \frac{1}{2} \sum_{\substack{n=0 \\ n \neq k}}^{\infty} e_n \cdot \left[\sin((n-k) \cdot \gamma_m + \varphi_n) + \sin((n+k) \cdot \gamma_m + \varphi_n) \right]$$

$$e_{sin}^{k} = -\sin(k \cdot \gamma_m) \cdot e = -\sin(k \cdot \gamma_m) \cdot \sum_{n=0}^{\infty} e_n \sin(n \cdot \gamma_m + \varphi_n)$$

$$= -\frac{1}{2} \cdot e_k \cdot \cos(\varphi_k) + \frac{1}{2} \cdot e_k \cdot \cos(2 \cdot k \cdot \gamma_m + \varphi_k) - \tag{3.18}$$

$$- \frac{1}{2} \cdot \sum_{\substack{n=0 \\ n \neq k}}^{\infty} e_n \cdot \left[\sin((n-k) \cdot \gamma_m + \varphi_n) - \sin((n+k) \cdot \gamma_m + \varphi_n) \right]$$

Equations (3.17) and (3.18) show that the transformation makes the kth controller work with constant variables associated with the kth harmonic of $\Delta\Omega_m$. The remaining sine and cosine components have mean values of zero over one period of γ_m. It is well worth noting that the controller for the DC component does not contain a sine part. The output

T_k^* of the kth controller corresponds to the kth harmonic of the reference torque T^*. Furthermore, each PI-controller is equipped with a saturation and an anti-windup algorithm in order avoid the overshoot due to the nonlinear behavior of the limits. The priority of the anti-windup procedures is set based on the magnitude of the corresponding harmonic of the load torque.

The design of the harmonic speed controller is necessary to complement the theoretical analysis. It was proven that the harmonic speed controller is equivalent to a combination of a resonant filter and a proportional controller [39]. Therefore, for a single harmonic the integral gains of the PI controllers can be selected in the same way applied to the PI-R controller. The proportional gains can be combined to form a single proportional part whose value is identical to that of the PI speed controller designed based on the symmetric optimum criteria.
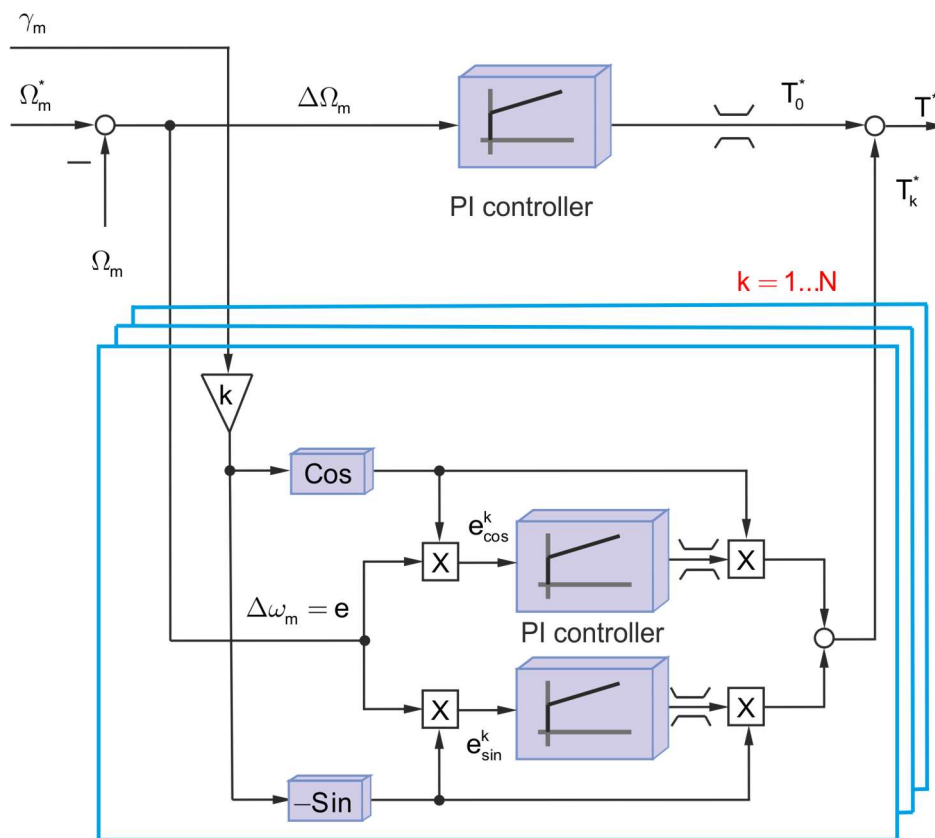

Fig 3.13. A full harmonic speed controller

A full harmonic speed controller is illustrated in Fig 3.13 where harmonics up to the Nth are considered. The increase of N, the more harmonics to be controlled, and the smaller oscillations the speed response. However, the higher the value of N, the more

complex the speed controller and the more calculation to microprocessor or DSP. The selection of N is carried out according to a tradeoff between the algorithm complexity and the desirable quality of the speed response.

3.3   Summary of the chapter

This chapter explained the principle of the FOC for the PMSM, including a general block diagram and criteria for designing current and speed controllers.

The chapter also elaborated on a new method for designing the speed controller. To reduce undesirable harmonics in the speed response originated from an angle-dependent load torque, either a proportional-integral resonant controller or a harmonic speed controller can be used. The former controller relies on resonant parts to compensate for specific predefined harmonics. The latter type refers to an individual PI-controller for each harmonic in the spectrum of the speed response.

4 Sensorless Control of the Permanent Magnet Synchronous Machine

4.1 Introduction

The field-oriented control requires information of the field angle for the coordinate transformations and the mechanical speed for the speed control loop as it is shown in Fig 3.1. The field angle is usually obtained by using an angular transducer installed in the shaft of the machine. However, the sensor is sensitive to the influences of the environment, such as dirt, temperature and etc. The sensor also increases the cost of investment and maintenance, the cables and interface card for installation and commissioning. In the following sections, the sensorless control of the PMSM is presented, where an enhanced voltage model based method is utilized to drive the machine at medium and high-speed speed region while signal injection technique is adopted for the low-speeds including standstill. Finally, a combined field angle observer is introduced to obtain a wide speed-range sensorless control of the machine.

4.2 High-speed sensorless control of the drive

In the sensorless control scheme of a PMSM in medium- and high speed region, i.e. the operating speed is larger than 3% the rated speed, a fundamental field wave model is usually used. The methods utilize either a voltage model [18][27], state observers [19][43] or Kalman filters [44][45] for the estimation of the field angle. In the voltage model based methods, the voltages and the measured currents are used to estimate the position of the rotor from the voltage equations. Parameter variations due to temperature and saturation strongly affect the performance of the estimation algorithm. The state observers and the Kalman filters based methods are less sensitive to parameter variations. However, it is difficult to define covariance matrixes for the Kalman filters or design the state observers. Even though the three approaches differ from each other in the way to estimate the field angle, they share a common characteristic of not being able to work at low and zero stator frequency [17].

A sensorless control can be built in a conventional FOC scheme by substituting the angle measurement by an observer or estimation algorithm. In practical applications, the sensorless scheme should be simple, reliable and easy to be configured. An enhanced

voltage model based method is used in this work because it fulfills the aforementioned requirements [18].

The enhanced voltage model is derived from the mathematical description of the PMSM in the rotor-fixed reference frame given by (2.18). Equation (2.18) is restated hereafter for the purpose of theoretical analysis.

$$u_d = R \cdot i_d + L_d \cdot \frac{di_d}{dt} - \omega \cdot L_q \cdot i_q$$

$$u_q = R \cdot i_q + L_q \cdot \frac{di_d}{dt} + \omega \cdot L_d \cdot i_d + \omega \cdot \psi_p$$

(4.1)

In the sensorless operation mode, the estimated rotor-fixed reference frame is used since the actual reference frame is unknown. Fig 4.1 represents both the estimated and the actual rotor-fixed reference frames, in which the subscript '$_e$' indicates variables associated with the estimated coordinate system.
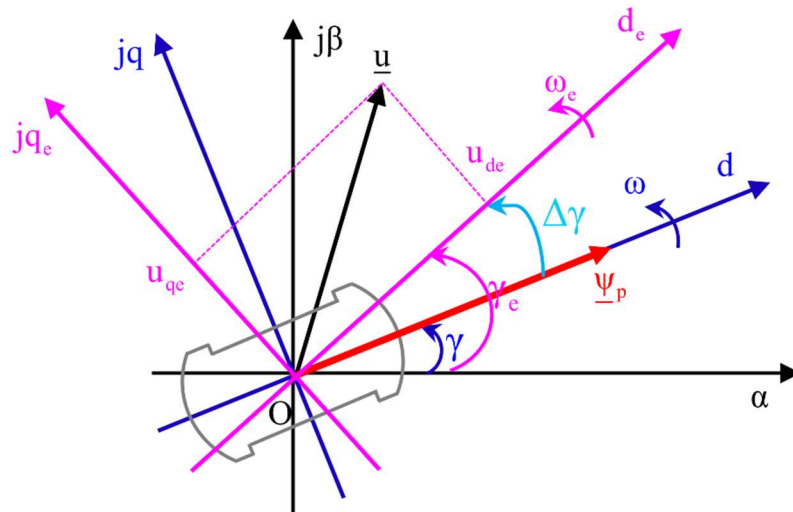

Fig 4.1. Estimated and actual rotor reference frames

The voltage equation (4.1) in regard to the estimated reference frame is given in (4.2) [46]:

$$u_{de} = \left(R + \Delta L \cdot \omega_e \cdot \sin 2\Delta\gamma\right) \cdot i_{de} + \left(L_d - 2 \cdot \Delta L \cdot \sin^2 \Delta\gamma\right)\frac{di_{de}}{dt} -$$

$$-\left(s \cdot \Delta L \cdot \sin 2\Delta\gamma + \left(L_q + 2 \cdot \Delta L \cdot \sin^2 \Delta\gamma\right) \cdot \omega_e\right) \cdot i_{qe} + \psi_p \cdot \omega \cdot \sin \Delta\gamma$$

$$u_{qe} = \left(R - \Delta L \cdot \omega_e \cdot \sin 2\Delta\gamma\right) \cdot i_{qe} + \left(L_q + 2 \cdot \Delta L \cdot \sin^2 \Delta\gamma\right)\frac{di_{qe}}{dt} -$$

$$-\left(s \cdot \Delta L \cdot \sin 2\Delta\gamma - \left(L_d + 2 \cdot \Delta L \cdot \sin^2 \Delta\gamma\right) \cdot \omega_e\right) \cdot i_{de} + \psi_p \cdot \omega \cdot \cos \Delta\gamma$$

(4.2)

The error angle $\Delta\gamma = \gamma_e - \gamma$ is the difference between the estimated field angle γ_e and the true field angle γ. The inductance difference is defined by $\Delta L = \left(L_d - L_q\right)/2$.

At fundamental frequency, the PMSM ensures $\Delta L \ll L_d \approx L_q$. If the error angle $\Delta\gamma$ is sufficiently small, all terms related to the multiplication of two small variables including ΔL, $sin\Delta\gamma$, and $sin(2\Delta\gamma)$ in (4.2) can be ignored. As a result, (4.2) can be rewritten as:

$$u_{de} = R \cdot i_{de} + L_d \cdot \frac{di_{de}}{dt} - L_d \cdot \omega \cdot i_{qe} + \psi_p \cdot \omega \cdot \sin \Delta\gamma$$

$$u_{qe} = R \cdot i_{qe} + L_q \cdot \frac{di_{qe}}{dt} + L_q \cdot \omega \cdot i_{de} + \psi_p \cdot \omega + \psi_p \cdot \omega \cdot \cos \Delta\gamma$$

(4.3)

Because $sin\Delta\gamma \approx \Delta\gamma, cos\Delta\gamma \approx 1$, the two delta voltages defined by (4.4) contain information about the speed error and position error. They can be used for a tracking algorithm to estimate the position and the speed of the rotor.

$$\Delta u_d = u_{de} - R \cdot i_{de} - L_d \cdot \frac{di_{de}}{dt} + L_d \cdot \omega_e \cdot i_{qe} = \psi_p \cdot \omega \cdot \sin \Delta\gamma \approx \psi_p \cdot \omega \cdot \Delta\gamma$$

$$\Delta u_q = u_{qe} - R \cdot i_{qe} - L_q \cdot \frac{di_{qe}}{dt} - L_q \cdot \omega_e \cdot i_{de} - \psi_p = \psi_p \left(\omega \cdot \cos \Delta\gamma - \omega_e\right) \approx -\psi_p \cdot \Delta\omega$$

(4.4)

In (4.4), the electrical speed error $\Delta\omega = \omega_e - \omega$ is the difference between the estimated speed ω_e and the actual speed ω.

Fig 4.2 shows the block diagram of the sensorless control algorithm based on the enhanced voltage model. The motor model was built according to (4.1). The two artificial voltage components given by (4.4) are utilized in a tracking algorithm, which contains two tracking loops. The inner loop and the outer loop provide the estimates of the electrical angular velocity and the field position angle, respectively. The inner loop depends on a parameter $1/T_\omega$, which is the corner frequency of the controller response

in the Bode diagram. The estimated speed should be low-pass filtered before using as a feedback signal for the speed control loop. As the field angle tracking loop already contains an integral, only a proportional part characterized by parameter k_p is required to ensure a zero error angle in the steady state. In many cases, the gain k_p can be chosen in the range $[0,75; 1.25]$.

The enhanced voltage model depicted in Fig 4.2 has a disadvantage associated with the time derivative of the currents expressed by the two expressions $L_d \cdot \frac{di_{de}}{dt}$ and $L_q \cdot \frac{di_{qe}}{dt}$. The time derivative makes the sensorless control algorithm less applicable. To overcome this drawback, instead of adding the time-derivative components to the delta voltages Δu_d and Δu_q, they are moved to the output of the inner tracking loop as shown in Fig 4.3. The mathematical descriptions of the two voltage models are identical, but the model without the time derivative is more reliable [18].

It is necessary to mention that the sensorless control method based on the enhanced voltage model still depends on the accuracy of the machine parameters. If the parameters are well known, the rotor position and the rotor speed can be precisely estimated; otherwise, the tracking algorithm fails to provide sufficiently precise estimates. To ensure a good performance of the sensorless drive, an online parameter adaption is crucial. It is well known that the permanent magnet flux and the stator resistance are temperature-dependent, while the inductance is not influenced by temperature, but by the stator currents. A look-up table that demonstrates the relationship between the inductance and the currents can be used for an inductance tuning rule. To deal with the temperature dependency of the permanent magnet flux and the stator resistance, an online adaptive parameters identification tuning can be utilized [29][47].

In experiments carried out in our laboratory, the enhanced voltage model method was proven to be able to work at the lowest frequency of 3 Hz corresponding to 3% rated frequency under no load. The enhanced voltage model based method is used in this work to drive the PMSM at 100 Hz to emulate faulty bearings according to the ISO 10816 standard. In the normal operation of the electric drive, the machine is operated at low speed range, including zero speed. The signal injection technique is utilized in this case and is presented in the following section.
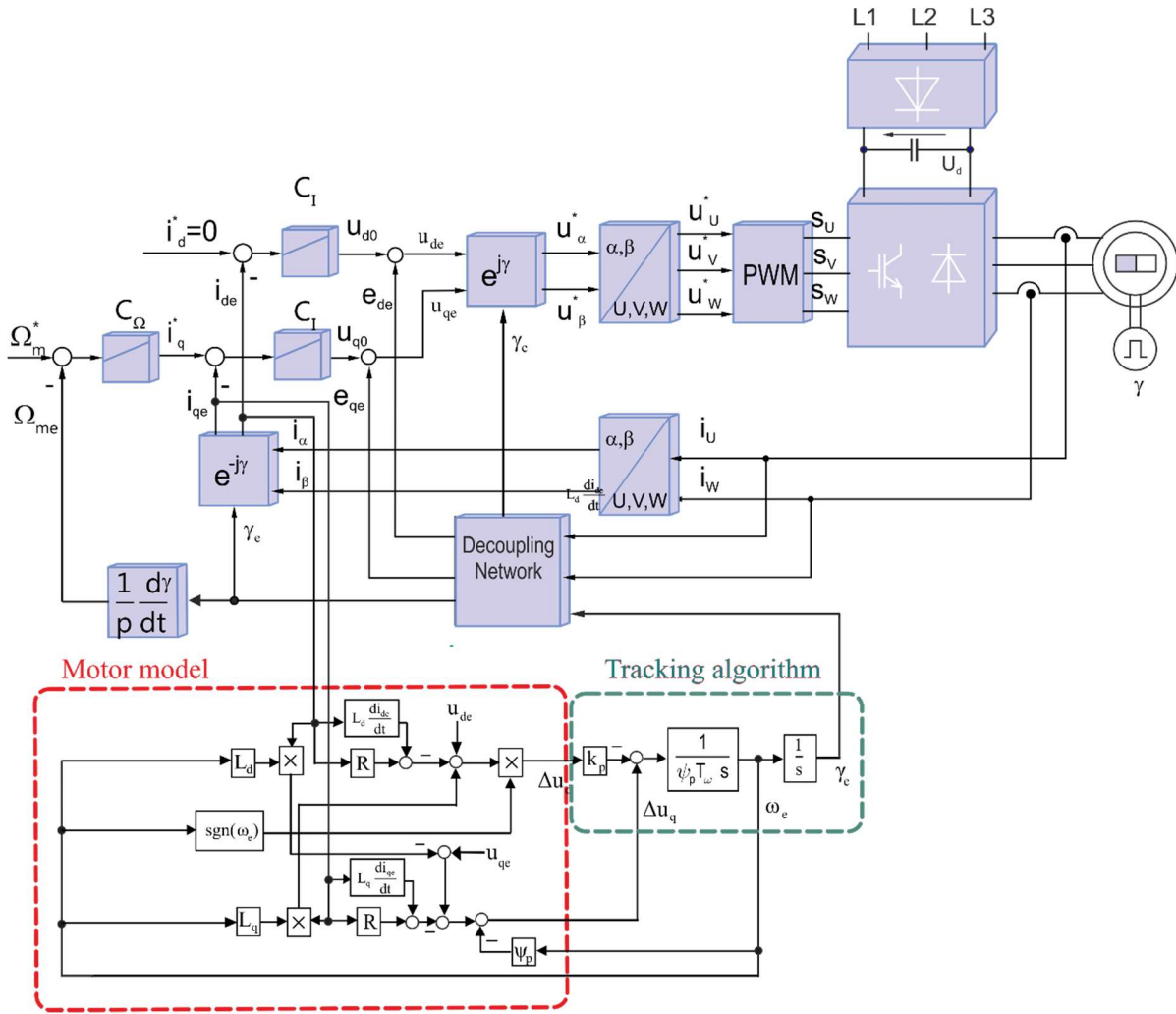
Fig 4.2. Block diagram of the sensorless control of PMSM with an enhanced voltage model
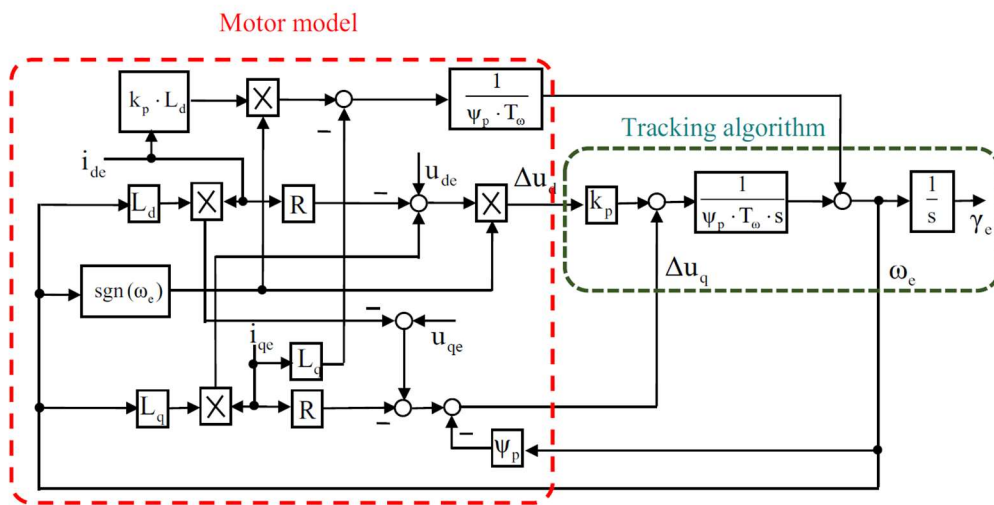

Fig 4.3. Block diagram of the modified enhanced voltage model

4.3 Low-speed sensorless control of the drive

Sensorless control for the PMSM at low-speed region requires signal injection techniques that explore the anisotropic properties of the machine [21][46][48]. In such schemes, extra signals are injected to the motor, then corresponding signals are measured and processed to detect the position of the rotor. The injection techniques differ from each other in the types of the injected signals and in the structure of the field angle tracking procedures.

Generally, a high-frequency voltage vector is used as the excitation signal and a corresponding current is used for the angle tracking algorithm. There are two main types of the injected voltage vector. One is a revolving carrier voltage generated by injecting a high-frequency rotating voltage vector to the input of the pulse-width modulator. The other one is an alternating carrier voltage vector that oscillates in a time-varying spatial direction [21]. Sensorless control methods based on either types of the injected voltage signals were proven successful to be performed in the low-speed region, including zero crossing under loaded conditions. When taking into account the signal-to-noise ratio, the dependencies on parameter variations and the inverter nonlinearities such as dead-time and zero current clamping, the method relied on the alternating carrier signal is preferred [49].

The field angle tracking plays an important role in ensuring a good performance of the sensorless drive. It should be able to track small saliency of PMSMs, especially those with permanent magnets mounted on the surface of the rotor. The tracking procedure can utilize band-pass filters [20][48] or Fourier interpolation [46] to extract the high-frequency current that contain information of the field angle. In this research, the demodulation procedure presented in [48] is adopted because of its simplicity and its sensitivities to small saliency.

For the purpose of convenience, the mathematical description of the PMSM in the actual rotor-fixed reference frame is stated again as follows:

$$
u_d = R \cdot i_d + L_d \cdot \frac{di_d}{dt} - \omega \cdot L_q \cdot i_q
$$
$$
u_q = R \cdot i_q + L_q \cdot \frac{di_q}{dt} + \omega \cdot L_d \cdot i_d + \omega \cdot \psi_p
$$

$$(4.5)$$

If only high-frequency components of the injected voltages and of the response currents are considered under an assumption that the injected frequency is sufficiently higher than the rotor speed, the PMSM can be regarded as a simple R-L circuit. The voltage equations (4.5) can be rewritten as [50]:

$$u_{dh} = R \cdot i_{dh} + L_{dh} \cdot \frac{di_{dh}}{dt}$$
$$u_{qh} = R \cdot i_{qh} + L_{qh} \cdot \frac{di_{qh}}{dt} \tag{4.6}$$

The subscript '$_h$' indicates parameters and variables of the machine corresponding to a high-frequency.

Equation (4.6) can be expressed in the frequency domain as follows:

$$u_{dh} = \left(R + j \cdot \omega_h \cdot L_{dh} \right) \cdot i_{dh} \equiv z_{dh} \cdot i_{dh}$$
$$u_{qh} = \left(R + j \cdot \omega_h \cdot L_{qh} \right) \cdot i_{qh} \equiv z_{qh} \cdot i_{qh} \tag{4.7}$$

The terms $z_{dh} = R + j \cdot \omega_h \cdot L_{dh}$, $z_{qh} = R + j \cdot \omega_h \cdot L_{qh}$ are the d- and q-axis high-frequency impedances; ω_h is the frequency of the injected signal.

With regard to the estimated rotor reference frame, the relationship between the high-frequency voltages and the high-frequency currents is established based on the coordinate transformations presented in section 2.2.

$$\begin{bmatrix} i_{deh} \\ i_{qeh} \end{bmatrix} = \begin{bmatrix} \cos\Delta\gamma & \sin\Delta\gamma \\ -\sin\Delta\gamma & \cos\Delta\gamma \end{bmatrix} \begin{bmatrix} i_{dh} \\ i_{qh} \end{bmatrix} = \begin{bmatrix} \cos\Delta\gamma & \sin\Delta\gamma \\ -\sin\Delta\gamma & \cos\Delta\gamma \end{bmatrix} \begin{bmatrix} 1/z_{dh} & 0 \\ 0 & 1/z_{dh} \end{bmatrix} \begin{bmatrix} u_{dh} \\ u_{qh} \end{bmatrix}$$
$$= \begin{bmatrix} \cos\Delta\gamma & \sin\Delta\gamma \\ -\sin\Delta\gamma & \cos\Delta\gamma \end{bmatrix} \begin{bmatrix} 1/z_{dh} & 0 \\ 0 & 1/z_{dh} \end{bmatrix} \begin{bmatrix} \cos\Delta\gamma & -\sin\Delta\gamma \\ \sin\Delta\gamma & \cos\Delta\gamma \end{bmatrix} \begin{bmatrix} u_{deh} \\ u_{qeh} \end{bmatrix} \tag{4.8}$$

where i_{deh}, i_{qe} are the d- and q-axis high-frequency current components; u_{deh}, u_{qeh} are the d- and q-axis high-frequency voltage components in the estimated reference frame.

If an alternating high-frequency voltage defined by

$$u_{deh} = \hat{u}_h \cos\left(\omega_h t\right); \quad u_{qeh} = 0 \tag{4.9}$$

is superimposed on the d-component of the stator voltage in the estimated rotor reference frame, the corresponding high-frequency current given by (4.8) can be obtained [50]:

$$
\begin{aligned}
i_{deh} &= \frac{\hat{u}_h \cdot \cos(\omega_h \cdot t)}{z_{dh} \cdot z_{qh}} \left(\frac{z_{dh} + z_{qh}}{2} - \frac{z_{dh} - z_{qh}}{2} \cdot \cos 2\Delta\gamma \right) \\
i_{qeh} &= \frac{\hat{u}_h \cdot \cos(\omega_h \cdot t)}{z_{dh} \cdot z_{qh}} \left(\frac{z_{dh} - z_{qh}}{2} \cdot \sin 2\Delta\gamma \right)
\end{aligned}
\tag{4.10}
$$

Equation (4.10) shows that the d- and q-axis high-frequency current components in the estimated rotor reference frame contain information of the field error angle $\Delta\gamma$ if the high-frequency impedance difference between the d- and q-axis exists, i.e. $(z_{dh} - z_{qh}) \neq 0$. The d-axis current component in (4.10) does not become zero in case of a zero error angle. On the contrary, the q-axis current component depends on the field error angle $\Delta\gamma$. If the resistance is small enough in comparison to the high-frequency inductance, it follows with

$$
\begin{aligned}
z_{dh} &\equiv R + j \cdot \omega_h \cdot L_{dh} \approx j \cdot \omega_h \cdot L_{dh}; \\
z_{qh} &\equiv R + j \cdot \omega_h \cdot L_{qh} \approx j \cdot \omega_h \cdot L_{qh}
\end{aligned}
\tag{4.11}
$$

That the q-axis current component can be rewritten as:

$$
i_{qeh} = \frac{\hat{u}_h \cdot \sin(\omega_h \cdot t)}{L_{dh} \cdot L_{qh} \cdot \omega_h} \frac{L_{dh} - L_{qh}}{2} \cdot \sin(2\Delta\gamma)
\tag{4.12}
$$

And if the error angle $\Delta\gamma$ is sufficiently small, which results in $\sin(2\Delta\gamma) \approx 2\Delta\gamma$, then the q-axis current component can be rewritten as:

$$
i_{qeh} = \frac{\hat{u}_h \cdot \sin(\omega_h \cdot t)}{L_{dh} \cdot L_{qh} \cdot \omega_h} \frac{L_{dh} - L_{qh}}{2} \cdot 2\Delta\gamma
\tag{4.13}
$$

Equation (4.13) shows that the q-axis current component is modulated by the field error angle $\Delta\gamma$. A full demodulation procedure for the estimation of the field angle is depicted in Fig 4.4.
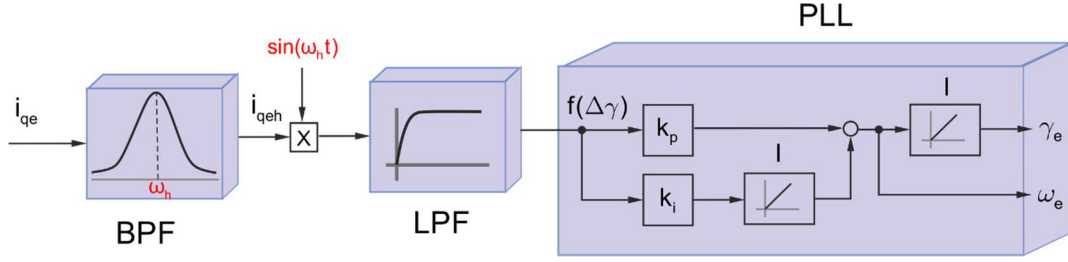
Fig 4.4. Block diagram of the demodulation procedure

The q-axis current component regarding the estimated rotor reference frame i_{qe} is band-pass filtered, resulting in the high-frequency current component i_{qeh} defined by (4.13). This signal is then modulated and low-pass filtered to get an error signal $f(\Delta\gamma)$.

$$f(\Delta\gamma) = \frac{\hat{u}_h}{\omega_h} \cdot \frac{L_{dh} - L_{qh}}{4 \cdot L_{qh} \cdot L_{dh}} \cdot 2 \cdot \Delta\gamma = K_{err} \cdot \Delta\gamma$$

$$K_{err} = \frac{\hat{u}_h}{\omega_h} \cdot \frac{L_{dh} - L_{qh}}{2 \cdot L_{qh} \cdot L_{dh}}$$

(4.14)

It is necessary to mention that the phase of i_{qe} due to the time delay of the inverter should be taken into account. A practical way to identify the phase lag is conducted by comparing the measured waveform of i_{qeh} with that of the reference signal $sin(\omega_h \cdot t)$. The phase lag should be compensated in the demodulation procedure. The error signal $f(\Delta\gamma)$ is further processed by a phase-locked loop (PLL) to obtain the field angle and field speed. The parameters of the PI-controller in the PLL can be tuned according to the characteristic of the low-pass filter (LPF). Assuming that a first-order low pass filter with the transfer function given by (4.15) is utilized.

$$LPF(s) = \frac{\beta_{lp}}{s + \beta_{lp}}$$

(4.15)

where β_{lp} is the bandwidth of the filter.

The block diagram of the PLL can be interpreted in Fig 4.5. The PI controller has the transfer function given by

$$G_{PI}(s) = \frac{k_p \cdot s + k_i}{s}$$

(4.16)

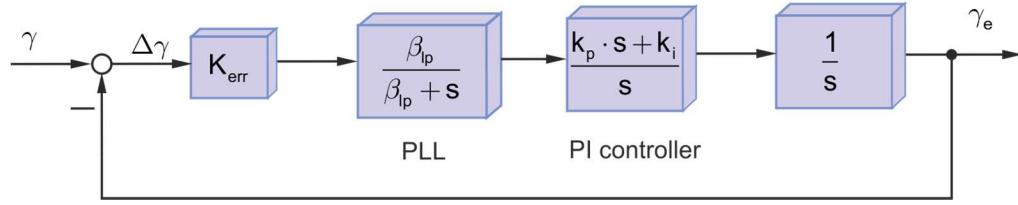where k_p and k_i are the parameters of the PI controller in the PLL.

Fig 4.5. Block diagram of the PLL

The closed-loop transfer function $T(s)$ of the PLL is [51]:

$$T(s) = \frac{\gamma_e}{\gamma} = \frac{K_{err} \cdot k_p \cdot \beta_{lp} \cdot s + K_{err} \cdot k_i \cdot \beta_{lp}}{s^3 + \beta_{lp} \cdot s^2 + K_{err} \cdot k_p \cdot \beta_{lp} \cdot s + K_{err} \cdot k_i \cdot \beta_{lp}} \tag{4.17}$$

A pole-placement method is used to calculate the parameters of the PI controller in the PLL [51]. The closed-loop poles are located at $s = -\beta$, meaning that the denominator of the transfer function $T(s)$ is equivalent to $(s + \beta)^3$. Eventually, the cut-off frequency of the low-pass filter and the parameters of the PI controller of the PLL can be calculated and given by (4.18).

$$\beta_{lp} = 3\beta; \quad k_p = \frac{\beta_{lp}}{3K_{err}}; \quad k_i = \frac{\beta_{lp}^2}{27K_{err}} \tag{4.18}$$

A full low-speed sensorless control scheme for the PMSM based on the injection technique is illustrated in Fig 4.6.
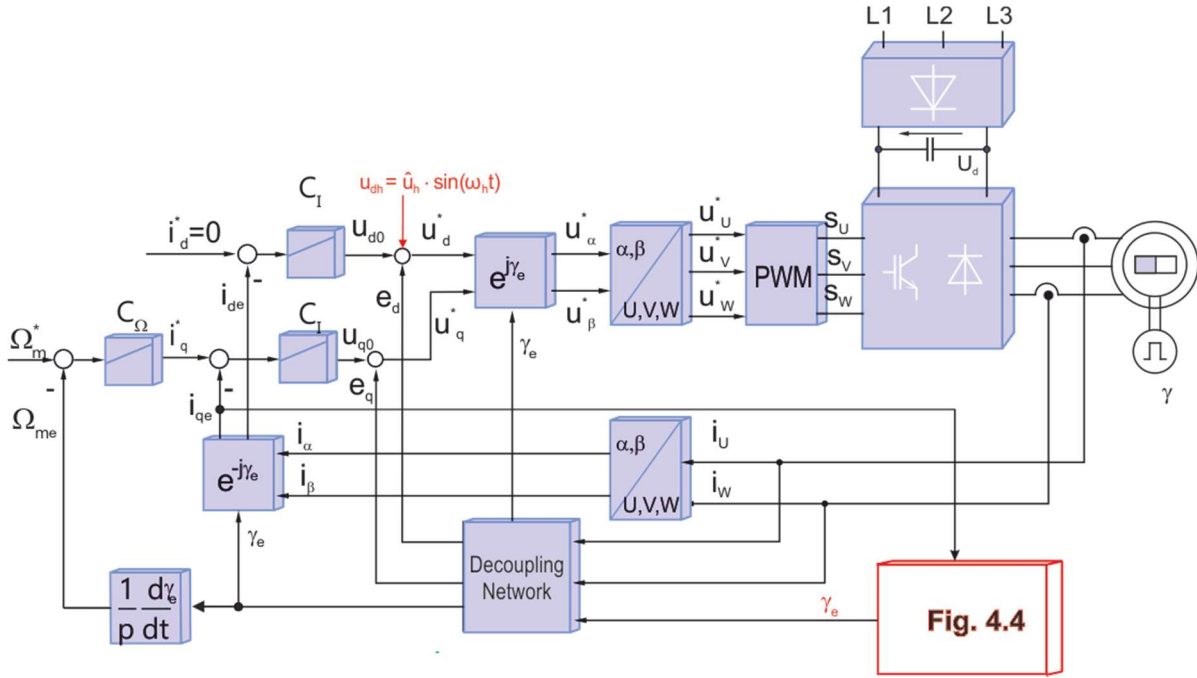
Fig 4.6. Sensorless control scheme of the PMSM at the low-speed

4.4 Wide speed range sensorless control of the drive

The sensorless drive should be able to work in a wide speed range because the machine may be required to work at different speeds. As aforementioned, methods that rely on the fundamental field wave models are applicable to the high-speed region, whereas signal injection based methods are well suited to operation at low-speeds. A combination of the two methods is a promising solution to implement the sensorless drive in a wide speed range.

An approach for combining the two methods was already discussed in [22], in which a modified voltage method is used throughout the whole speed range. The modified voltage model method is augmented with the signal injection technique at low-speeds. Fig 4.7 demonstrates the block diagram of the combined estimator. The estimates of the rotor speed and the rotor position are based on the following equations:

$$\omega_e = \omega_{e\_high} + k_i \cdot \int f(\Delta\gamma)\,dt$$
$$\gamma_e = \int \left[\omega_e + k_p \cdot f(\Delta\gamma)\right]dt$$

(4.19)

where ω_{e_high} is the estimate of the field speed according to the modified voltage method; k_i and k_p are defined by (4.18).
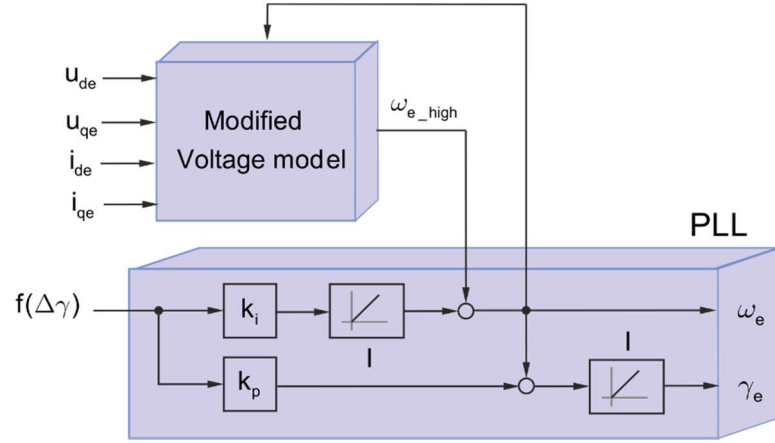
Fig 4.7. Combined angle estimation system [22]

In order to achieve a smooth transition between the low-speed and the high-speed regions, the injection voltage amplitude $\hat{u}_h$ and the bandwidth β_{lp} are linearly decreased with the increasing speed, and the signal injection method is disabled above the transition speed ω_{trans}, i.e.

$$
\hat{u}_h = \begin{cases} \dfrac{\omega_{trans} - |\omega_{me}|}{\omega_{trans}} \hat{u}_{h0}, & if \; |\omega_{me}| \le \omega_{trans} \\ 0, & \text{otherwise} \end{cases}
$$

$$
\beta_{lp} = \begin{cases} \dfrac{\omega_{trans} - |\omega_{me}|}{\omega_{trans}} \beta_{lp0}, & if \; |\omega_{me}| \le \omega_{trans} \\ 0, & \text{otherwise} \end{cases}
$$

$$(4.20)$$

where the parameters $\hat{u}_{h0}$ and β_{lp0} correspond to the zero-speed operation; ω_{me} is the estimated mechanical speed. It can be understood that in the high-speed region, the effect of the injection method vanishes. In the low-speed region, the estimates of the modified voltage model method act as disturbances while those of the injection method are dominant.

In this research work, the high-speed sensorless control is based on the enhanced voltage model as presented in section 4.2. The combined field angle observer is built in a similar way depicted in Fig 4.7, but a weighted coefficient W_0 is augmented to the calculation of the field velocity. The function of W_0 is to reduce the interference of disturbances proposed by the enhanced voltage model method at low-speeds. The determination of W_0 is given by (4.21) and is shown in Fig 4.8 (a).

$$W_0 = \begin{cases} \dfrac{|\omega_{me}|}{\omega_{trans}}, & if \ |\omega_{me}| \leq \omega_{trans} \\ 1, & otherwise \end{cases} \qquad (4.21)$$

The field angle and field velocity are now obtained from the following equations:

$$\omega_e = W_0 \cdot \omega_{e\_high} + k_i \cdot \int f(\Delta\gamma)\,dt$$
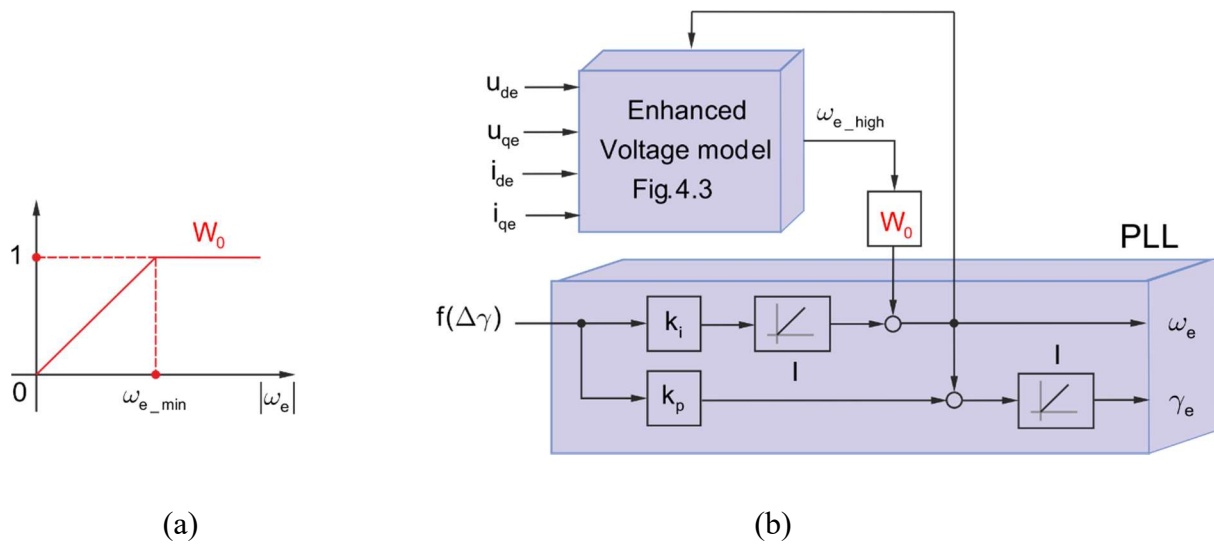$$\gamma_e = \int \left[\omega_e + k_p \cdot f(\Delta\gamma)\right]dt \qquad (4.22)$$

(a)   (b)

Fig 4.8. a) Determination of W_0; (b) block diagram of the proposed estimator

Fig 4.8 (b) shows the structure of the proposed observer. It is obvious that the effects of the signal injection method are inversely proportional to the speed and becomes zero in the speed region above ω_{trans}. The estimates obtained from the enhanced voltage model based method are prevalent in the high-speed region and vanishes at the zero crossing speed.

4.5 Summary of the chapter

The chapter discussed sensorless control for the PMSM. To drive the motor in the high-speed region, an enhanced voltage model based method was introduced. In the low-speed range including standstill, signal injection technique was presented. A combined estimator to drive the machine in both high and low-speed regions was proposed. By conducting the combined estimator, the PMSM can be driven in a wide speed range.

5 Load Torque Estimation in Repetitive Mechanical Systems

5.1 Introduction

As already presented in section 1.3, this work focuses on mechatronics systems characterized by repetitive cycles of production. In the laboratory, a slider-crank mechanism was designed and built as an example of such the system. It should be mentioned that the theoretical analysis and proposed control algorithm applied to the slider-crank mechanism can be extended to any mechatronics systems characterized by repetitive phenomenon. From the viewpoint of control, the mechanical configuration of the mechanism should be well known, where the load torque is a key parameter regarding the design of controllers of the electric drive. Therefore, this chapter introduces the mechanical structure and the equivalent model of the slider-crank mechanism, from which kinetic analysis can be carried out in order to obtain mathematical description of the load torque. The next step is to develop two methods for the estimation of the load torque in the time-domain by using Fourier interpolation. The proposed methods rely on the evaluation of the Fourier coefficients while representing the load torque in Fourier series.

5.2 Horizontal slider-crank mechanism

In technical installations, there are two main types of slider-crank mechanisms, one is the horizontal mechanism and the other is the vertical mechanism. The classification is based on the horizontal or vertical movement of the sliding object. In this work, the former type is utilized.

Fig 5.1(a) illustrates the mechanical structure of a horizontal slider-crank mechanism. As can be seen, the mechanism consists of three main parts: a slider, a connecting rod and a crank. The crank and the driven machine are connected by a coupling shaft. The reduced model depicted in Fig 5.1(b) is used for the kinetic analysis.

In the reduced model, $O, B,$ and C are the three articulated joints between the coupling shaft, the crank, the connecting rod and the slider. G_c and G_{crod} correspond to the centers of gravity of the crank and the connecting rod, respectively. As the mechanism has one

degree of freedom, a two-dimension coordinate system (Oxy) can be used to describe the position of each single body. The angles of the crank and the connecting rod with respect to the horizontal axis are denoted by γ_m and φ, respectively. Since the mechanism and the driven machine are directly coupled, i.e. no gearbox is used, the angle γ_m is also the mechanical angle of the rotor. It can be seen that the driven machine completes one cycle of the mechanism in one revolution of the rotor. In addition, without loss of generality, the surface on which the slider moves can be assumed to be the potential surface. The potential surface is used for the analysis of potential energy associated with each body in the mechanism.
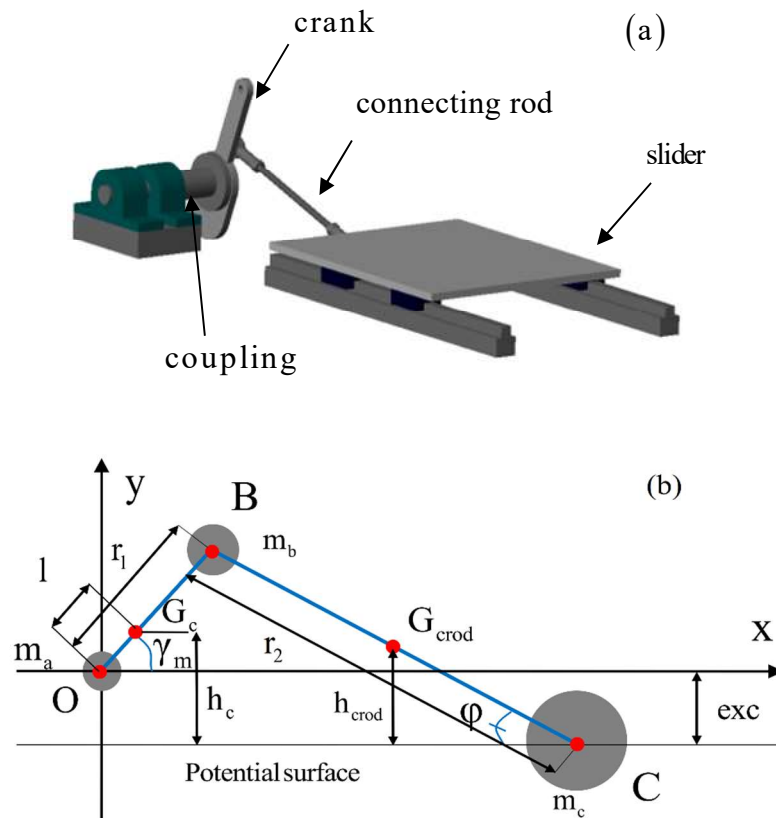
Fig 5.1. Horizontal slider-crank mechanism: a) mechanical structure; b) reduced model

5.3   Load torque calculation in the horizontal slider-crank mechanism

During the operation of the mechanism, there are four main sources of load torque including the changes of the inertia, of the potential energy, of the friction forces and of the crank velocity [52]. If the mechanism is analyzed in the steady state, the load torque

due to the change of the crank velocity can be ignored. The three remaining sources of the load torque will be presented hereafter.

5.3.1 Moment of inertia

According to the kinetic analysis [52], the total moment of inertia of the mechanism referred to the shaft of the drive is given in (5.1). The calculation of the equivalent inertia is explored and presented in appendix 9.2.

$$J_{mechanism}(\gamma_m) = m_b \cdot r_1^2 + m_c \cdot r_1^2 \cdot \left(\sin^2 \gamma_m + \lambda \cdot \sin \gamma_m \cdot \sin 2\gamma_m + 2 \cdot k \cdot \sin \gamma_m \cdot \cos \gamma_m \right) \quad (5.1)$$

with

$$m_b = 0.2 \cdot m_{crank} + 0.5 \cdot m_{crod}; \quad m_c = m_{slider} + 0.5 \cdot m_{crod}; \quad \lambda = r_1 / r_2; \quad k = exc / r_2 \quad (5.2)$$

The total moment of inertia is obtained by adding the moment of inertia of the machine J_{machi} , of the coupling shaft $J_{coupling}$ and of the mechanism $J_{mechanism}$:

$$J_{total}(\gamma_m) = J_{machine} + J_{coupling} + J_{mechanism}(\gamma_m) \quad (5.3)$$

The moment of inertia of the driven machine $J_{machine}$ and of the coupling shaft $J_{coupling}$ are constant while the moment of inertia of the mechanism $J_{mechanism}$ is a function of the crank angle γ_m. As a result, the total moment of inertia is an angle-dependent function.

5.3.2 Potential energy

The potential energy refers to energy possessed by an object by virtue of its position in relation to a reference object. The most common type of potential energy is the gravitational potential energy that depends on the mass of the object and the distance from its center to the reference object [53].

When the slider-crank mechanism operates, the crank and the connecting rod are the two components storing gravitational potential energy because their centers of gravity change regarding the potential surface. The total potential energy is given by (5.4).

$$W_p = W_{p,crank} + W_{p,crod} = m_{crank} \cdot g \cdot h_c + m_{crod} \cdot g \cdot h_{crod}$$

$$= m_{crank} \cdot g \cdot (l \cdot \sin \gamma_m + exc) + m_{crod} \cdot g \cdot \frac{1}{2} \cdot (r_1 \cdot \sin \gamma_m - exc) \tag{5.4}$$

where g is the gravitational acceleration; W_p is the total potential energy; $W_{p,crank}, W_{p,crod}$ are the potential energies of the crank and the connecting rod, respectively.

5.3.3 Modelling of the friction

Friction is a complex nonlinear phenomenon and exists in all mechanisms. In general, friciton is unwanted and is one of the main factors that limit the performance quality of mechanical systems. For this reason, many researches have focused on friction modeling and friction compensation [54][55][56]. Friction models are often used to identify friction forces, which can be compensated by applying equal forces or torque but opposite in sign. A precise friction model is necessary for a precise load torque compensation algorithm.

There have been a number of proposed friction models as listed in [57]. Due to its nonlinearity and dependency on the mechanical configuration, friction is not studied in in general cases but in specific circumstances. In the horizontal slider-crank mechanism, if internal friction of rolling bearings installed in the driven machine and in the articulated joints are neglected, friction mainly comes from the contact surface between the slider and the supporting frame. Friction is composed of four components: Coulomb friction, stiction, viscous damping and Stribek effect as shown in Fig 5.2.

A.   Stiction

Stiction, which is also known as break-away friction, has a non-zero value only when the slider is driven to a standstill. Fig 5.2(a) depicts the shape of the stiction force. Stiction at rest cannot be merely described as a function of velocity, it is often modelled with an external force F_e in the following description:

$$F_{sticiton} = \begin{cases} F_e & \text{if} \quad v_{slider} = 0 \quad \text{and} \quad |F_e| < F_s \\ F_s \cdot \text{sgn}(F_e) & \text{if} \quad v_{slider} = 0 \quad \text{and} \quad |F_e| \geq F_s \end{cases} \tag{5.5}$$
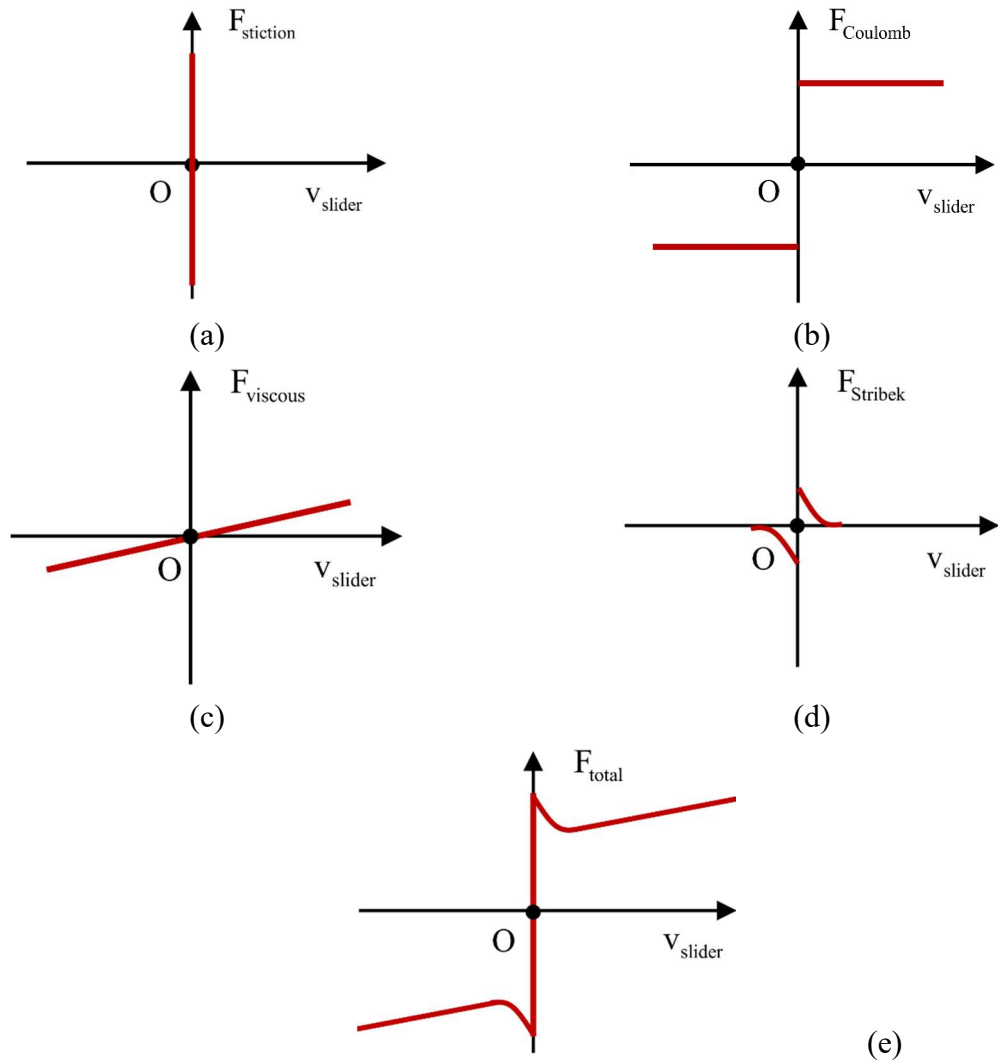
where F_s is a constant.

Fig 5.2. a) Stiction; b) Coulomb friction; c) viscous damping; d) Stribek effect; e) total friction

B. Coulomb friction

Coulomb friction does not depend on the area of the contact. It is proportional to the normal force the slider exerts on the supporting frame. The Coulomb friction is not dependent on the magnitude but on the direction of the slider velocity. Experimental observations have been carried out to prove that the Coulomb friction force is lower than the stiction force [54]. Fig 5.2(b) shows the graphical representation of the Coulomb friction. The mathematical description of the Coulomb friction force is:

$$F_{Coulomb} = K_c \cdot \text{sgn}(v_{slider})$$ (5.6)

where $K_c = \mu|F_N|$; μ is a friction coefficient; F_N is the normal force the slider exerts on the supporting frame.

In the horizontal slider-crank mechanism, the normal force is equal but opposite in sign to the potential force of the slider. Hence, the absolute value of the normal force $|F_N|$ is a constant. The coefficient K_c is known as the Coulomb constant.

The signum function $sgn(v_{slider})$ is defined by:

$$\text{sgn}\left(v_{slider}\right) = \begin{cases} +1 & ; \ v_{slider} > 0 \\ 0 & ; \ v_{slider} = 0 \\ -1 & ; \ v_{slider} < 0 \end{cases} \tag{5.7}$$

C. Viscous friction

Viscous friction as demonstrated in Fig 5.2(c) is due to the viscous behavior of the fluid lubricant on the contact surface between the slider and the supporting frame. The viscous force is proportional to the velocity of the slider. Equation (5.8) describes the calculation of the viscous force.

$$F_{viscous} = K_v \cdot v_{slider} \tag{5.8}$$

where K_v is known as the viscous constant.

D. Stribek effect

Stribek effect is due to the use of lubricant and occurs at the translation boundary from partial to a full fluid lubricant. As shown in Fig 5.2(d), Stribek effect is a highly nonlinear phenomena and arises in low-speed region.

E. Total friction force

The four aforementioned components of friction can be further classified into two groups. The stiction belongs to the first group and is called static friction. The second group known as kinetic friction includes the Coulomb friction, the viscous friction and the Stribek effect. Typically, the static friction between two surfaces is higher than the kinetic friction. If an applied force is strong enough to overcome the static friction, then the reduction of the friction to the kinetic friction can cause the two sticky surfaces to slide over each other [58]. This characteristic is known as stick-slip phenomenon.

The total friction force can be calculated by adding up the four friction components. Fig 5.2(e) shows the graphical representation of the total friction force. For mathematical description, only Coulomb friction and viscous friction are taken into account because the two other components are highly nonlinear and appear only at low-speeds.

$$F_{total} \approx F_{Coulomb} + F_{viscous} = K_c \cdot \text{sgn}(v_{slider}) + K_v \cdot v_{slider} \qquad (5.9)$$

where F_{total} is the total friction force.

5.3.4 Load torque calculation

The load torque demanded by the mechanical system is defined by the Euler-Lagrange equation [52].

$$T_{load} = J_{total} \frac{d^2\gamma_m}{dt^2} + \frac{1}{2} \cdot \frac{dJ_{total}}{d\gamma_m} \cdot \left(\frac{d\gamma_m}{dt}\right)^2 + \frac{dW_p}{d\gamma_m} + F_{total} \cdot \frac{dx_{slider}}{d\gamma_m} \qquad (5.10)$$

where $J_{total}, W_p, F_{total}$ are given by (5.3), (5.4) and (5.9), respectively; x_{slider} is the position of the slider with respect to the x-axis.

Supposing that the crank is driven at a constant angular velocity, i.e. $\Omega_m = d\gamma_m/dt = const$; $d^2\gamma_m/dt^2 = 0$, the first component of the load torque is zero. The derivation of the three remaining load torque components is presented in appendix 9.3. In summary, the load torque consists of four terms including the torque due to the change of inertia T_{inetia}, of the potential energy T_p, of the Coulomb friction $T_{Coulomb}$ and of the viscous friction $T_{viscous}$.

$$T_{load} = T_{inertia} + T_p + T_{Coulomb} + T_{viscous} \qquad (5.11)$$

where

$$T_{inertia} = \frac{1}{2} \cdot m_c \cdot r_1^2 \cdot \Omega_m^2 \left(\sin 2\gamma_m - \frac{1}{2} \cdot \lambda \cdot \sin\gamma_m + \frac{3}{2} \cdot \lambda \cdot \sin 3\gamma_m + 2 \cdot k \cdot \cos 2\gamma_m \right) \qquad (5.12)$$

$$T_p = \left(m_{crank} \cdot l + \frac{1}{2} \cdot m_{crod} \cdot r_1 \right) \cdot g \cdot \cos\gamma_m \qquad (5.13)$$

$$T_{Coulomb} = K_c \cdot r_1 \cdot \left| \sin \gamma_m + \frac{1}{2} \lambda \cdot \sin 2\gamma_m + k \cdot \cos \gamma_m \right| \tag{5.14}$$

$$T_{viscous} = K_v \cdot r_1^2 \cdot \Omega_m^2 \left(\sin \gamma_m + \frac{1}{2} \lambda \cdot \sin 2\gamma_m + k \cdot \cos \gamma_m \right)^2 \tag{5.15}$$

5.4   Load torque estimation methods

The four equations (5.12) - (5.15) show that the load torque depends not only on the system parameters and on the crank velocity, but also on the two unknown constants K_c and K_v. Furthermore, all the four components are periodic functions of the crank angle γ_m. Fig 5.3 shows the figure representation of the total load torque and its components at $\Omega_m = 60 \ min^{-1}$ with predefined values of the two constants K_c, K_v.

As the load torque changes periodically according to the angle γ_m, it can be characterized by using Fourier interpolation [59].

$$T_{load}\left(\gamma_m\right) = \frac{a_0}{2} + \sum_{k=1}^{\infty}\left[a_k \cdot \cos\left(k \cdot \gamma_m\right) + b_k \cdot \sin\left(k \cdot \gamma_m\right)\right] \tag{5.16}$$

The Fourier coefficients a_k and b_k are defined by:

$$a_k = \frac{2}{2\pi} \cdot \int_{\gamma_0}^{\gamma_0+2\pi} T_{load}\left(\gamma_m\right) \cdot \cos\left(k \cdot \gamma_m\right) d\gamma_m$$

$$b_k = \frac{2}{2\pi} \cdot \int_{\gamma_0}^{\gamma_0+2\pi} T_{load}\left(\gamma_m\right) \cdot \sin\left(k \cdot \gamma_m\right) d\gamma_m \tag{5.17}$$

Equation (5.16) shows that the load torque can be identified if the information about the crank angle γ_m and about the Fourier coefficients a_k and b_k is available. The angle can be measured by using an encoder assembled in the driven machine or estimated by using an observer of the rotor position. Therefore, the estimation of the load torque can be conducted via the evaluation of the Fourier coefficients.

The determination of the Fourier coefficients given in (5.17) shows that they depend on the load torque and on the crank angle. By assuming a good dynamic of the speed control loop, the reference torque, which is the output of the speed controller, can be regarded as a good approximation of the load torque. Accordingly, the Fourier

coefficients a_k and b_k can be estimated in one complete cycle of the mechanism, meaning that γ_m changes from γ_0 to $\gamma_0 + 2\pi$ for any starting angle γ_0.
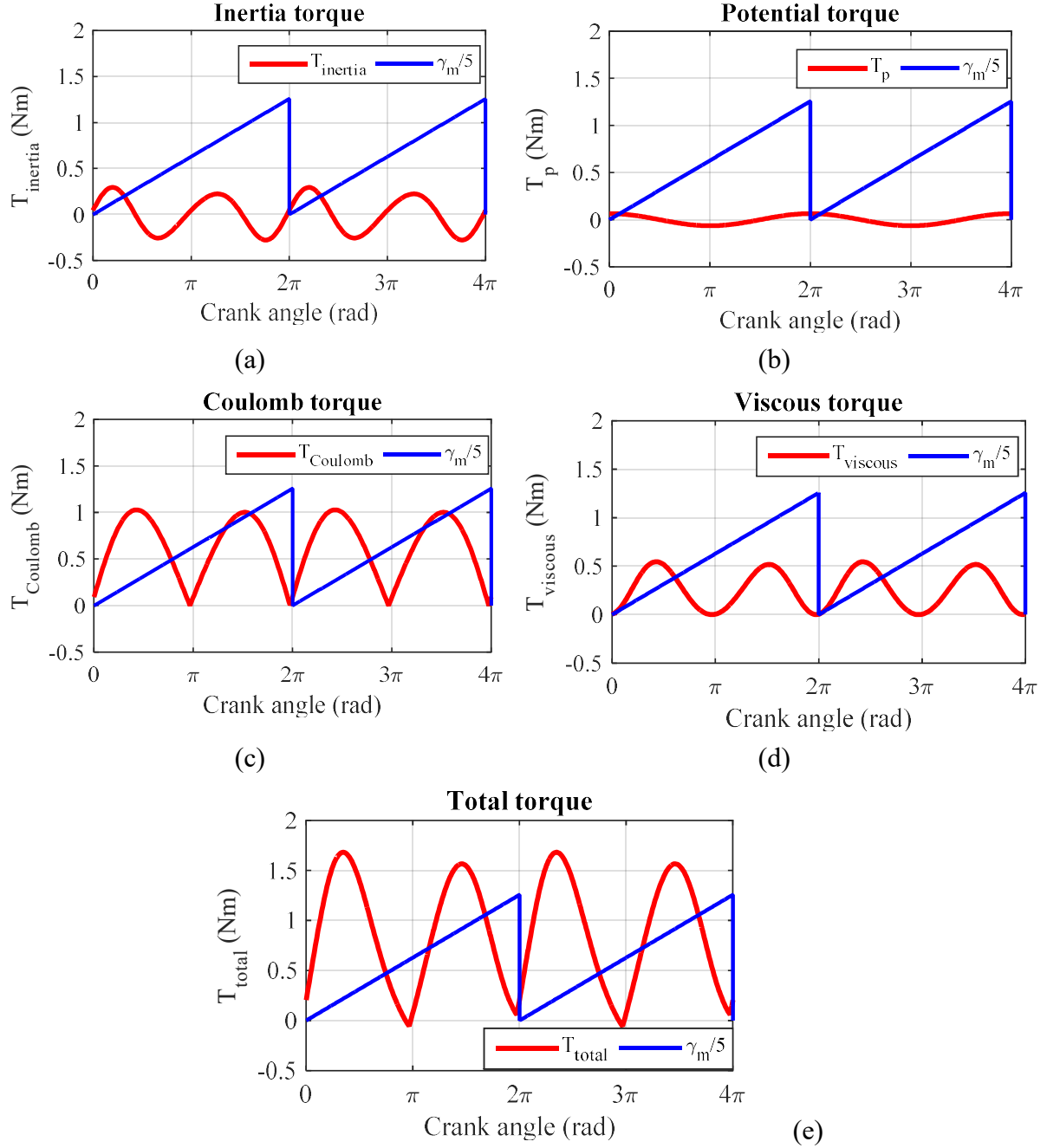

Fig 5.3. Calculation of the load torque components and total load torque with $\Omega_m = 60\ min^{-1}$, $K_c = 20\ N$, $K_v = 32.84\ Ns/m$,: a) inertia torque; b) potential torque; c) Coulomb torque; d) viscous torque; and e) total torque

For the calculation of the Fourier coefficients in (5.16), it is usual to use a DFT (Discrete Fourier Transform). Thus (5.17) is discretized by dividing one period 2π into N equal portions, where each portion is

$$\Delta\gamma_m = \frac{2\pi}{N} \tag{5.18}$$

By taking a period $[\gamma_0, \gamma_0 + 2\pi]$, (5.17) can be rewritten as:

$$a_k = \frac{2}{N \cdot \Delta\gamma_m} \cdot \sum_{i=0}^{N-1} T(i \cdot \Delta\gamma_m) \cos(k \cdot i \cdot \Delta\gamma_m) \cdot \Delta\gamma_m = \frac{2}{N} \sum_{i=0}^{N-1} T(i \cdot \Delta\gamma_m) \cos(k \cdot i \cdot \Delta\gamma_m)$$

$$b_k = \frac{2}{N \cdot \Delta\gamma_m} \cdot \sum_{i=0}^{N-1} T(i \cdot \Delta\gamma_m) \sin(k \cdot i \cdot \Delta\gamma_m) \cdot \Delta\gamma_m = \frac{2}{N} \sum_{i=0}^{N-1} T(i \cdot \Delta\gamma_m) \sin(k \cdot i \cdot \Delta\gamma_m) \tag{5.19}$$

The sums in (5.19) can be numerically evaluated by using a sliding window whose figure representation is shown in Fig 5.4. It can be seen that there are increments of the angle γ_m in time. Each angle increment $\Delta\gamma_m$ triggers a window shift, meanwhile the microprocessor starts a recalculation of (5.19) by adding the value corresponding to the new window portion and subtracting the value of the oldest window portion.
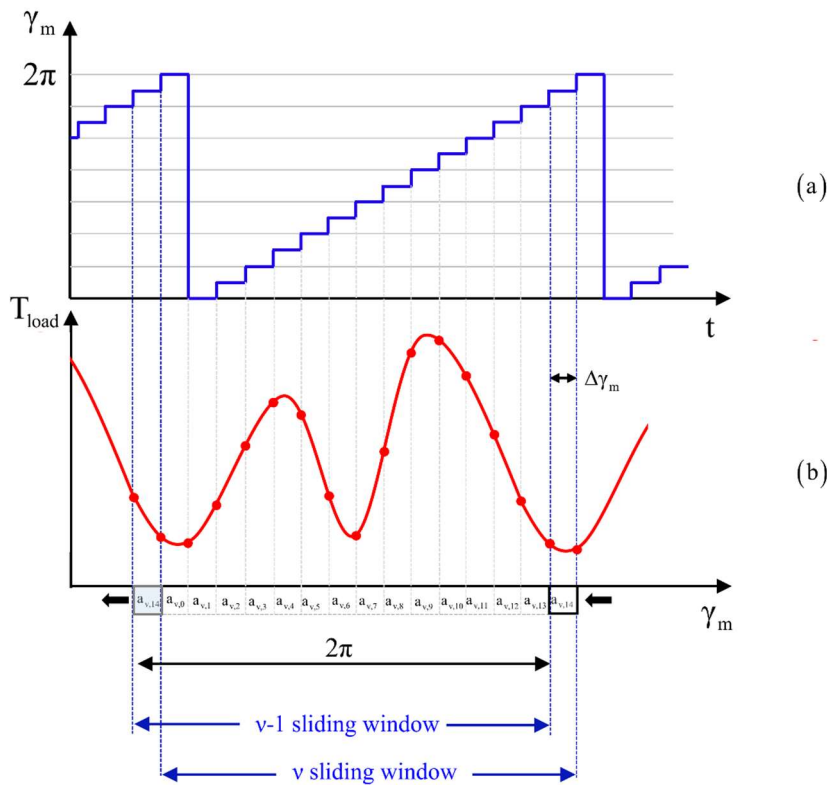
Fig 5.4. Graphical representation of a sliding window method

The sliding window method has some primary characteristics as follows:

- The quantization of a window $\Delta\gamma_m$ is inversely proportional to the number of window portions N, which is also the number of samples in one period. The increase of N yields more precise estimation results. However, the increase of N demands more calculation and memory to microcontrollers because all partial calculation of (5.19) must be stored. The selection of N depends on the sampling time T_s of the estimation algorithm and on the highest frequency f_{max} to be considered [60].

$$N \leq \frac{1}{f_{max} \cdot T_s} \tag{5.20}$$

  N should be properly chosen before carrying out any calculation.

- The shifting speed between the window portions depends on the mechanical velocity of the mechanism and on the window quantization.

- The sliding window method converges after one period. Fig 5.5 depicts simulation results where the estimated torque tracks precisely the reference torque after exactly one cycle of the mechanism.
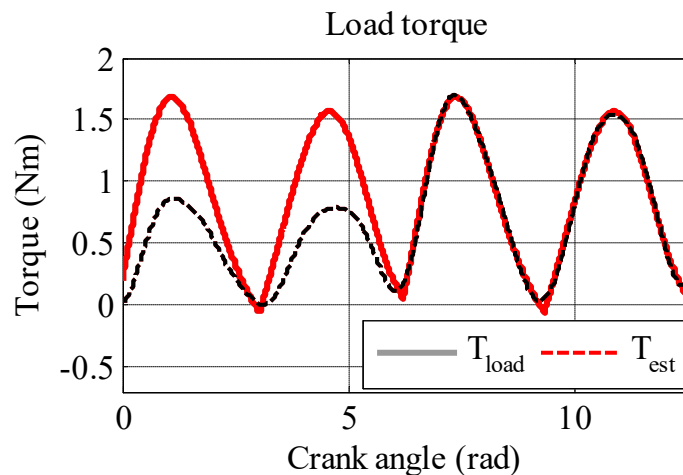
Fig 5.5. Simulation of the load torque and the estimated load torque

An alternative approach that can be used for the evaluation of the Fourier coefficients comes from the structure related to the harmonic speed controller as presented in section 3.2.2. Since the drive is analyzed in the steady state, there is no demanded load torque due to the change of the speed. Therefore, the function of the speed controller is to generate a reference torque to cancel the load torque. The control structure shown in Fig 5.6 is designed for the kth harmonic of the speed error, which is originated from the kth harmonic of the load torque. This means that the kth speed controller aims to cancel the kth harmonic of the load torque. As a result, the outputs of the PI controllers corresponding to e^k_{cos} and e^k_{sin} deliver good estimates of the Fourier coefficients a_k and $-b_k$, respectively [40].
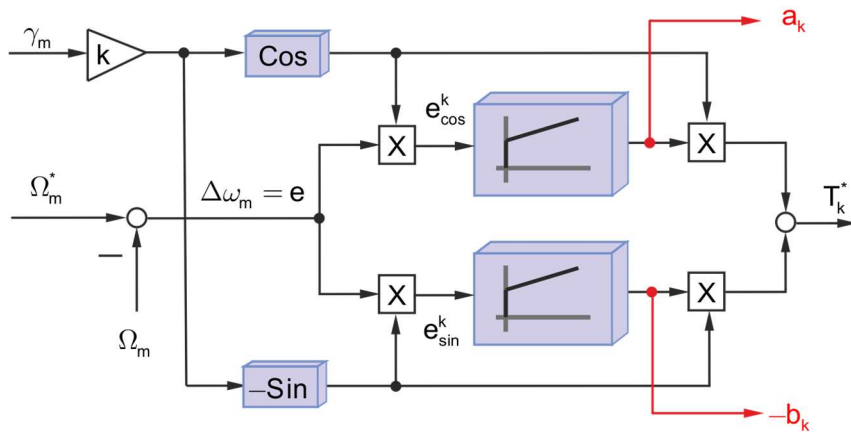
Fig 5.6. Estimation of the Fourier coefficients based on harmonic speed controller
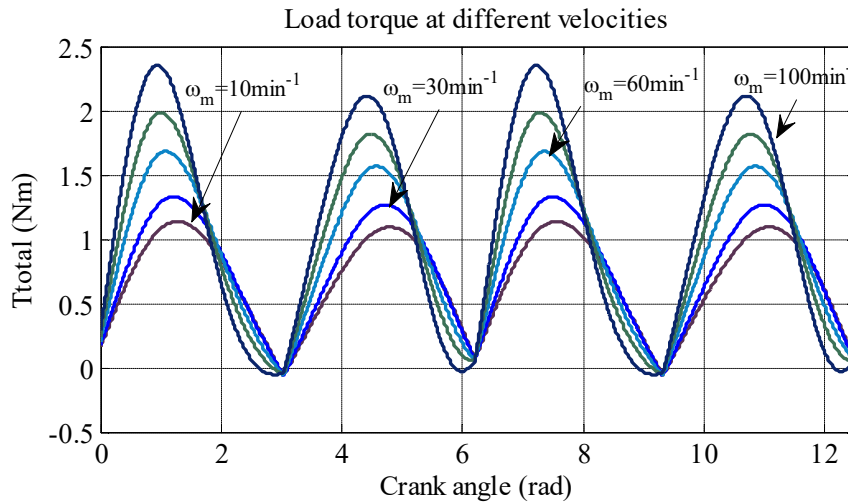

Fig 5.7. Simulation of the load torque at different velocities of the mechanism

In summary, the demanded load torque in the horizontal slider-crank mechanism is a periodic function of the crank angle and can be represented in terms of Fourier series. The estimation of the load torque can be conducted through the evaluation of the Fourier coefficients. At a certain operating velocity, the coefficients can be determined by using either a sliding window method or a harmonic speed controller. The load torque calculation given by equations (5.12) - (5.15) shows that if the two unknown constants K_c and K_v are identified, the load torque only depends on the crank velocity. Fig 5.7 depicts the shape of the load torque at different velocities within the operational speed-range of the mechanism. In order to make the load torque estimation possible at any speed, two approaches including a phenomenological method and a look-up table based method are proposed and presented in the following sections [61].

5.4.1 Phenomenological method

The phenomenological method is based on the physical description of the system and the associated physical phenomenon. In this method, each Fourier coefficient is explicitly described by a function of the crank angle γ_m. To do so, the four components of the load torque given in (5.12)-(5.15) are represented in terms of Fourier series. The two components $T_{inertia}$ in (5.12) and T_p in (5.13) are already trigonometric functions. The two other components can be expanded into Fourier series if the angle-dependent functions

$$f_1(\gamma_m) = \left| \sin \gamma_m + \frac{1}{2}\lambda \cdot \sin 2\gamma_m + k \cdot \cos \gamma_m \right|$$

$$f_2(\gamma_m) = \left(\sin \gamma_m + \frac{1}{2}\lambda \cdot \sin 2\gamma_m + k \cdot \cos \gamma_m \right)^2$$

(5.21)

are in the form of Fourier expansion. When considering the values of the mechanism parameters given in appendix 9.2, $\lambda = r_1/r_2 = 0.147$ and $k = exc/r_2 = 0.0882$ are obtained. Then $f_1(\gamma_m)$ and $f_2(\gamma_m)$ can be calculated by a Matlab-Simulink model in one period of γ_m. The data is stored and processed by the FFT (Fast Fourier Transform) tool to obtain the Fourier coefficients as given in Table 5.1 and Table 4.2.

Table 5.1. Coefficients of $\left| \sin \gamma_m + \frac{1}{2}\lambda \cdot \sin 2\gamma_m + k \cdot \cos \gamma_m \right|$

Harmonic order	DC	1	2	3	4	5
Cos	0.64	0.06	- 0.423	- 0.04	- 0.084	- 0.01
Sin		0	0.074	0	0.031	0.0002

Table 5.2. Coefficients of $\left(\sin \gamma_m + \frac{1}{2}\lambda \cdot \sin 2\gamma_m + k \cdot \cos \gamma_m \right)^2$

Harmonic order	DC	1	2	3	4	5
Cos	0.51	0.0697	- 0.492	- 0.069	0	0
Sin		0.0061	0.0868	0.0061	0	0

Accordingly, the load torque can be described in the following equation:

$$T_{load}\left(\gamma_m\right)=\frac{a_0}{2}+\sum_{k=1}^{5}\left[a_k\cdot\cos\left(k\cdot\gamma_m\right)+b_k\cdot\sin\left(k\cdot\gamma_m\right)\right] \qquad (5.22)$$

where a_k and b_k are given in Table 5.3.

Table 5.3. Fourier coefficients of the load torque

Symbol	Harmonic	Coefficient
$a_0/2$	DC	$0.64\cdot K_c\cdot r_1+0.51\cdot K_v\cdot r_1^2\cdot\Omega_m$
a_1	$\cos\gamma_m$	$0.06\cdot K_c\cdot r_1+0.0697\cdot K_v\cdot r_1^2\cdot\Omega_m+0.104$
a_2	$\cos(2\cdot\gamma_m)$	$m_c\cdot r_1^2\cdot\Omega_m^2\cdot k-0.4235\cdot K_c\cdot r_1-0.4924\cdot K_v\cdot r_1^2\cdot\Omega_m$
a_3	$\cos(3\cdot\gamma_m)$	$-0.04\cdot K_c\cdot r_1-0.0697\cdot K_v\cdot r_1^2\cdot\Omega_m$
a_4	$\cos(4\cdot\gamma_m)$	$-0.0864\cdot K_c\cdot r_1$
a_5	$\cos(5\cdot\gamma_m)$	$-0.01\cdot K_c\cdot r_1$
b_1	$\sin\gamma_m$	$0.25\cdot m_c\cdot r_1^2\cdot\Omega_m^2\cdot\lambda+0.0061\cdot K_v\cdot r_1^2\cdot\Omega_m$
b_2	$\sin(2\cdot\gamma_m)$	$0.5\cdot m_c\cdot r_1^2\cdot\Omega_m^2+0.0754\cdot K_c\cdot r_1+0.0868\cdot K_v\cdot r_1^2\cdot\Omega_m$
b_3	$\sin(3\cdot\gamma_m)$	$0.75\cdot m_c\cdot r_1^2\cdot\Omega_m^2\cdot\lambda+0.0061\cdot K_v\cdot r_1^2\cdot\Omega_m$
b_4	$\sin(4\cdot\gamma_m)$	$0.0308\cdot K_c\cdot r_1$
b_5	$\sin(5\cdot\gamma_m)$	$0.0002\cdot K_c\cdot r_1$

In practical situations, harmonics up to the 5th are taken into account as a compromise between the estimation precision and the algorithm complexity. To complete the phenomenological calculation of the Fourier coefficients, the two constants K_c and K_v must be determined. For doing so, the relationship between the DC component and the two constants is considered. Fig 5.8 depicts experimental measurements of the eleven coefficients given in Table 5.3 by using the sliding window method.
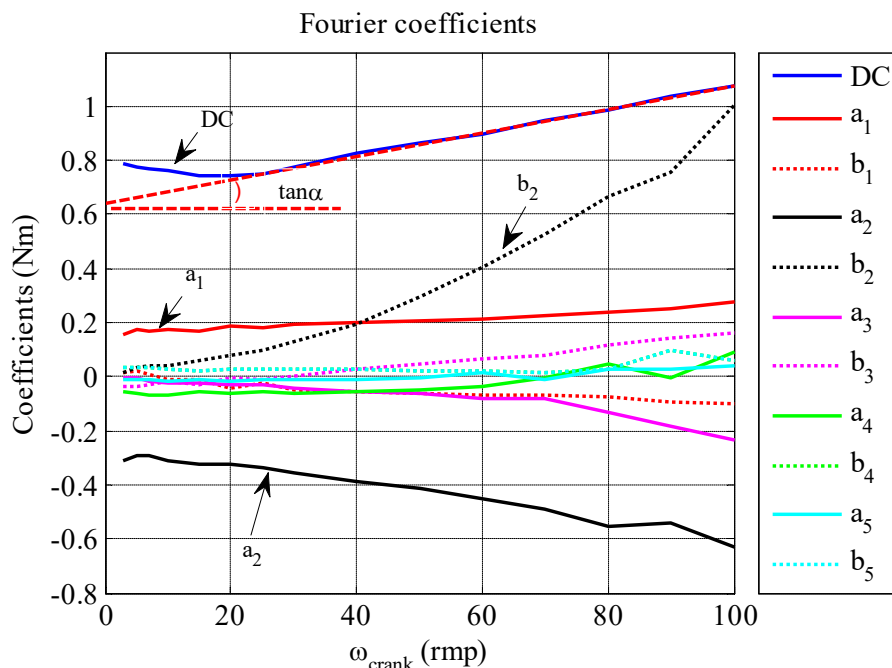
Fig 5.8. Fourier coefficients obtained from experiments by using the sliding window method

The data was obtained by running the mechanism at different constant speeds. The straight dotted red line characterizing the linear behavior of the DC component with respect to the mechanical speed Ω_m is achieved by connecting the two points located on the border of the linear region. The intersection of the straight dotted red line with the vertical axis helps identify the Coulomb constant while its slope can be used to calculate the viscous constant. It is observed that the curve of the DC component shows a nonlinear phenomenon in the low speed region. The reason is that when the slider is moved slowly, the Stribeck effect occurs and considerably contributes to the demanded load torque. However, the Stribek effect is not taken into account in the kinetic analysis of the mechanism.

The procedure for conducting the load torque estimation based on the phenomenological method is shown in Fig 5.9. The mechanical velocity Ω_m is measured or estimated and used for the calculation of the Fourier coefficients according to Table 5.3. The obtained coefficients, together with the crank angle γ_m, are used to calculate the load torque based on (5.22).
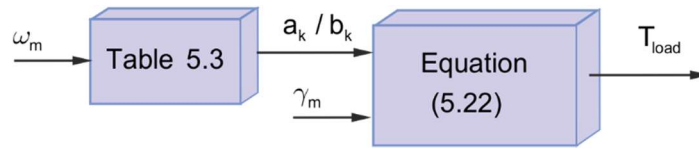
Fig 5.9. Block diagram of the phenomenological method for the load torque estimation

5.4.2 Look-up table based method

It can be realized that the phenomenological method relies on the theoretical analysis of the load torque. The precision of the estimation procedure strongly depends on the precision of the load torque model, which unfortunately is nonlinear. The phenomenological method is less applicable especially at low-speed region at which the stiction and the Stribeck effect are dominant. Thus, an alternative solution called here as look-up table based method is proposed. The idea behind the look-up table method is that the Fourier coefficients are estimated by using look-up tables constructed from measurements on the mechanical system. There are two steps to build such tables:

Step 1: The crank is driven at different angular velocities within its operational range $[0; \Omega_{m,max}]$. In each case, a set of coefficients $[a_k; b_k]$ is obtained.

Step 2: For the calculation of each Fourier coefficient, a two-dimension look-up table is created from the data obtained in Step 1. The input of the table is the crank angular velocity Ω_m. Linear interpolation is used for reducing the size and calculation of the tables.

Fig 5.10 illustrates the concept of the look-up table based method. The crank velocity obtained from a mechanical angular sensor or from an angle observer goes to the look-up tables to evaluate the Fourier coefficients. With the information of the crank angle, equation (5.22) delivers the estimate of the load torque.
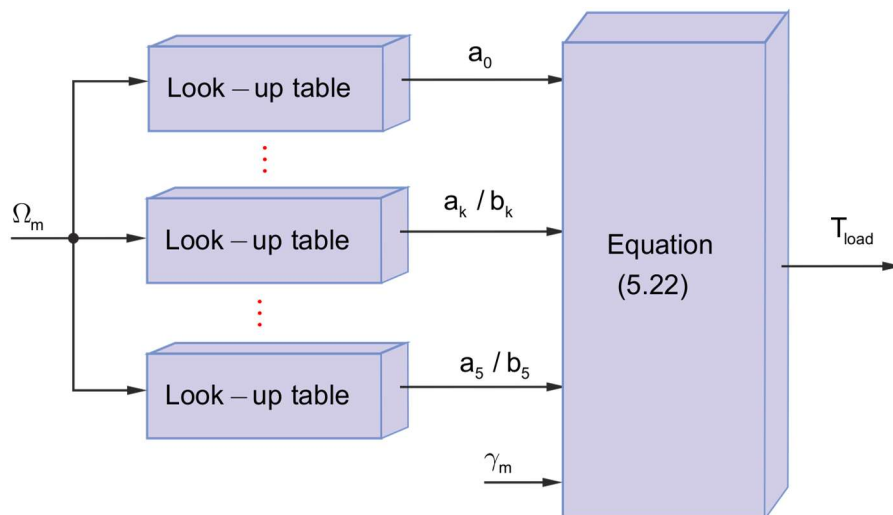
Fig 5.10. Block diagram of the look-up table based method

5.5   Summary of the chapter

This chapter explained the mechanical structure of a horizontal slider-crank mechanism, which is used as an example of repetitive mechanical systems. The model of the load torque was presented theoretically. The mathematical description of the load torque shows that it depends on the system parameters, on K_c and K_v which are known as the Coulomb and viscous constants, on the mechanical position γ_m and on the mechanical speed Ω_m of the crank.

The load torque is a periodic function of the crank angle, so it can be characterized by using Fourier series. The estimation of the load torque can be carried out by the evaluation of the Fourier coefficients. There are two methods for the estimation of the coefficients: one is based on theory while the other is based on look-up tables.

The estimated load torque can be used either in a feed-forward control scheme in order to improve the speed response quality or in a bearing fault detection method which will be presented in the next chapter.

6 Diagnosis of Faults in Rolling Bearing

6.1 Introduction

As presented in Chapter 5, the load torque in a repetitive mechanical system can be estimated by using Fourier interpolation. The estimated load torque can be used as a compensation signal in a feed-forward control scheme to improve the speed response quality as well as for the analysis of mechanical states of bearings installed in the industrial system. When a healthy bearing is in operation, the load torque demanded by the mechanical system does not include the torque coming from the bearing because of negligible internal friction. On the contrary, under faulty working conditions, a defective bearing can cause changes on the demanded load torque. Since the bearing faults and the demanded load torque are correlated, the information of the faults can be obtained by analyzing the load torque.

This chapter describes the mechanical structure of a ball bearing, the causes and effects of the bearing failures and proposes a novel bearing-fault detection method.

6.2 Structure and load distribution of a rolling ball bearing

A rolling bearing is a bearing that carries a load by placing rolling elements like balls or rollers between two bearing rings known as raceways. The relative motion of the raceways causes the rolling elements to roll with very little rolling resistance and very little sliding [62].

According to the types of the rolling elements, rolling bearing can be classified into two groups, including ball bearing and roller bearing shown in Fig 6.1. Ball bearing is subsequently divided according to its raceways configuration, including deep groove and angular contact. Roller bearing, on the other hand, is classified according to the cylindrical, needle, tapered or spherical shape of the rollers.

The rolling bearing can be further classified based on the direction of the applied load. By following this classification scheme, two types of rolling bearing can be found: radial bearing which carries radial loads and thrust bearing which carries axial loads [63].
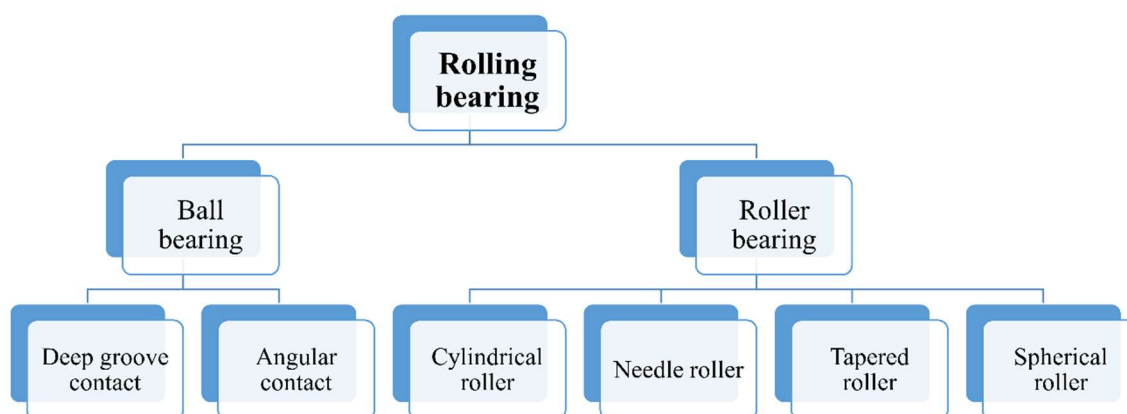
Fig 6.1. Classification of the rolling bearing

Fig 6.2 shows a graphical representation of an angular contact ball bearing. The two bearing rings are an inner raceway and an outer raceway, between which a set of balls can rotate. A cage is installed inside the bearing in order to keep the balls evenly distributed around its whole circumference and also to provide even load distribution and uniform running.

Contact angle α, or load angle, is defined as the angle between the centerline of the bearing and the direction of the force that the rolling elements exert on the outer raceway as shown in Fig 6.2 [5]. Angular contact ball bearings are designed to accommodate both radial and axial loads. The contact angle often ranges from 10 to 45 degrees. For bearings that are only subjected to radial load, the contact angle is zero, i.e. ($\alpha = 0$).

The research about the load distribution on the elements of a ball bearing to build friction models was carried out and presented in [64]. It was proven that when radial load is applied to a bearing, the rolling elements are not equally loaded. In addition, the load zone for a radically loaded bearing with internal clearance, i.e. the total distance through which one ring can be moved relative to the other ring, would be less than 180^0.

Fig 6.3 shows the load zone and the load distribution of a bearing subjected to only radial load with zero internal clearance. The number of balls in the bearing is $z = 10$. In the bearing, five balls carry the load including ball number one and two more pairs. The parameter n referred to the number of ball pairs carrying the load in addition to ball number one is defined by (6.1) [65].
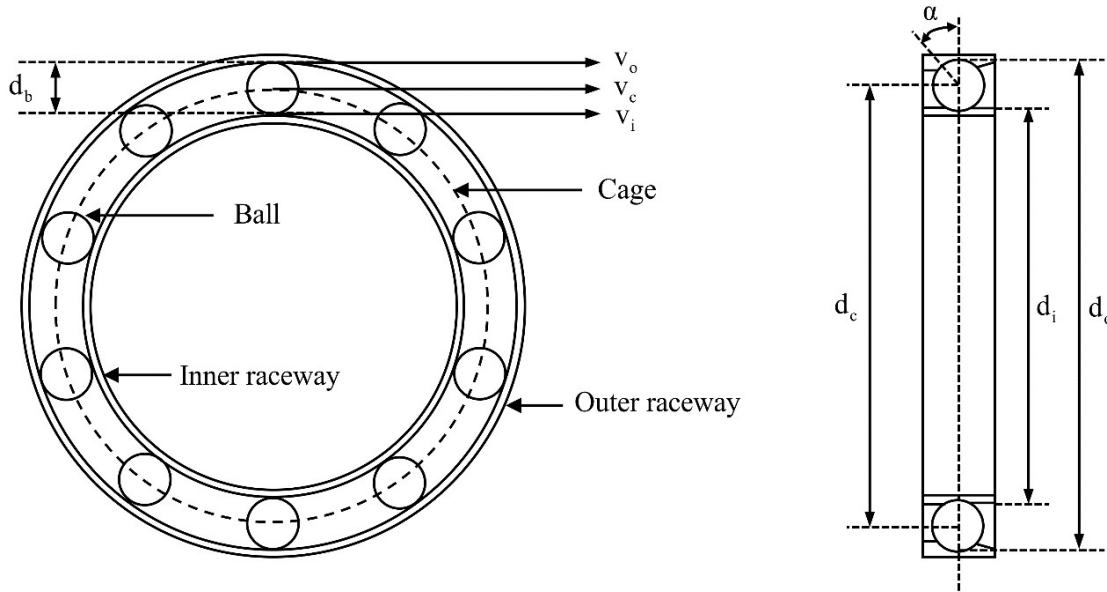
Fig 6.2. Mechanical and kinetic representation of a ball bearing

- v_0: tangential velocity of the outer raceway
- v_c: tangential velocity of the cage
- v_i: tangential velocity of the inner raceway
- d_b: diameter of the ball
- d_c: diameter of the cage
- d_i: diameter of the inner raceway
- d_0: diameter of the outer raceway
- α : load angle

$$n = INT\left(\frac{z-1}{4}\right) \tag{6.1}$$

where z is the number of balls; INT is the integer function meaning that any fractional part of (6.1) is truncated.

Angle β between the two adjacent rolling elements is given by:

$$\beta = \frac{2\pi}{z} \tag{6.2}$$

In the static equilibrium of the bearing, the load on the rolling elements is given by:

$$P_r = P_1 + 2 \cdot P_2 \cdot \cos\beta + \ldots + 2 \cdot P_{n+1} \cdot \cos n\beta \tag{6.3}$$

where P_r is the applied radial load on the bearing and P_i for $i = 2 \ldots n$ is the load on a rolling element.
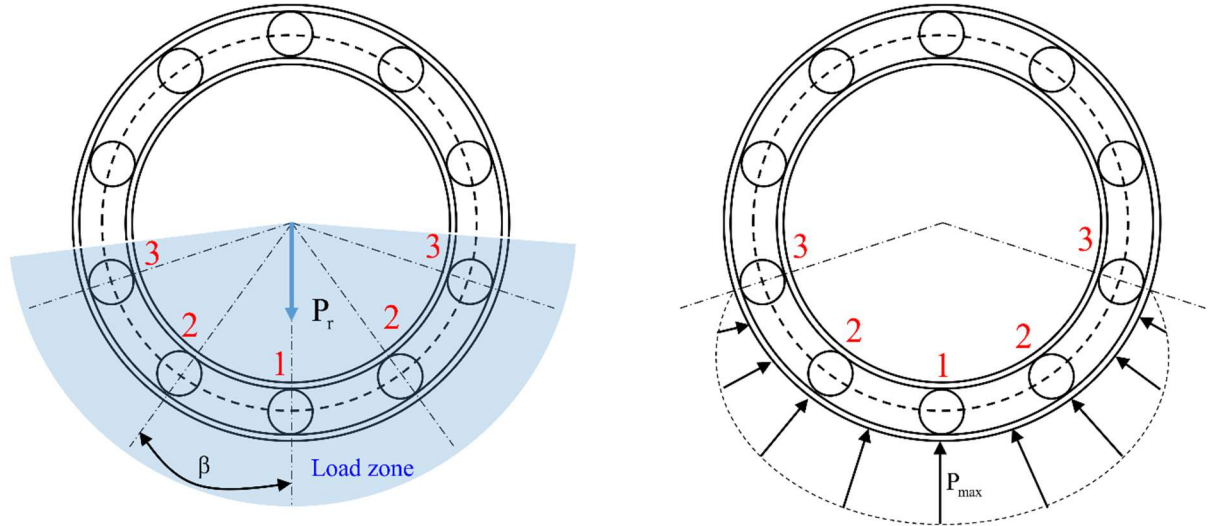
Fig 6.3. Ball bearing: a) load zone and b) load distribution

The relationship between the load on each individual ball and the load exerted on ball number one as shown in Fig 6.3 is:

$$P_i = P_1 \cdot \cos\left((i-1)\beta\right)^{3/2}, \ i = \overline{2, n+1} \tag{6.4}$$

By combining (6.3) and (6.4), the radial load on the bearing can be found and given by the following equation.

$$P_r = P_1 \cdot \left[1 + 2 \cdot \left(\cos\beta\right)^{5/2} + \ldots + 2 \cdot \left(\cos n\beta\right)^{5/2}\right] \tag{6.5}$$

As P_1 is the maximum ball load and is denoted by P_{max}, and if the function in the bracket in (6.5) is denoted as Q, or:

$$Q = 1 + 2 \cdot \left(\cos\beta\right)^{5/2} + \ldots + 2 \cdot \left(\cos n\beta\right)^{5/2} \tag{6.6}$$

Equation (6.5) can be rewritten as:

$$P_r = P_{max} \cdot Q = P_{max} \cdot \frac{z}{S_t} \tag{6.7}$$

where $S_t = z/Q$ is a constant.

The load torque exerted on ball number one can be calculated from (6.7):

$$P_1 = P_{max} = P_r \cdot \frac{S_t}{z} \tag{6.8}$$

Thus, the exerted on the ball number i is:

$$P_i = P_{max} \cdot \cos\left((i-1)\beta\right)^{3/2} \tag{6.9}$$

Equation (6.9) shows that the load distribution is sinusoidal and is illustrated in Fig 6.3 (b).

6.3   Bearing faults causes

Rolling bearings are designed to have a long lifetime. To maximize the lifetime of a bearing, it must be properly installed, lubricated and maintained. Poor operating conditions, such as moist environments, contaminated areas and improper handling can lead to a reduction of the lifetime of the bearing. When a bearing fault is found, it is important to determine the exact cause of the fault in order to make appropriate adjustments to avoid a similar failure in the future [66].

Under normal operating conditions, including a balanced load and a good alignment, a fatigue bearing fault starts with a fissure located below the raceways or rolling elements. With time, the fissure propagates up to the surface and eventually causes a localized fatigue phenomenon known as spalling or flaking. The affected area rapidly expands over the entire circumference of the raceways or the rolling elements, and pollutes the lubricant. As a result, a failure occurs with a rough running of the bearing [4]. Even though this is the most commonly found cause of rolling bearing faults, there are many external sources that speed up the failure process, including contamination, corrosion, improper lubrication, defective installation and overheating.

Due to harsh environment conditions present in almost all industrial installations, contamination and corrosion are the leading external sources of bearing faults. Contamination includes airborne dust, dirt and any abrasive substances, whose hardness ranges in between relatively soft and diamond-like. Once contamination finds its ways to the bearing, it contaminates the bearing lubricant and triggers an incipient bearing

fault. Corrosion comes from the exposition of the bearing to corrosive fluids like water, acid, deteriorated lubricant, etc. [4]. The usual effect of corrosion is the increase of vibration followed by wear. In extreme cases, corrosion can initiate an early fatigue bearing failure.

The operation of the bearing balls depends on the continuous presence of a very thin film of lubricant between the balls and the raceways or between the cage and the balls. Improper lubrication includes both under- and over-lubrication, and in either cases, the balls cannot rotate on the desired oil film that increases the level of heating. Excessive temperature degrades the properties of the lubricant and accelerates the bearing failure process.

Installation failures are associated with an improper installation of the bearing to the shaft or in the housing. An improper installation produces either physical damage known as brinelling or misalignment. Brinelling relates to the formation of indentation in the raceways which increases the vibration of the bearing. Any static overload or strong impact, such as dropping assembled equipment or using hammers to remove or install the bearing, can cause brinelling. Severe brinell-marks can result in a premature fatigue failure. Misalignment is also a common result of the defective bearing installation. If misalignment appears and exceeds $1\mu m/mm$, the temperature of the bearing balls or of the housing can reach an abnormal value, which eventually reduces the lifetime of the bearing [66].

Overheating is another external source causing bearing failure. The temperature in excess of 120^0 C can anneal the ring and the ball materials. The resulting loss in hardness reduces the loaded capability of the bearing. In severe cases, the balls and the raceways can be deformed. Some common causes of overheating include heavy electrical heat loads, inadequate heat paths, and insufficient cooling [66].

6.4 Classification and signatures of bearing faults

The classification of bearing faults is not performed based on the causes of the faults but on the consequence of the damage. A well-known approach to categorize bearing faults was presented in [5] where they are divided into two main types: single-point defect and generalized roughness as shown in Fig 6.4. This research work uses the same classification.
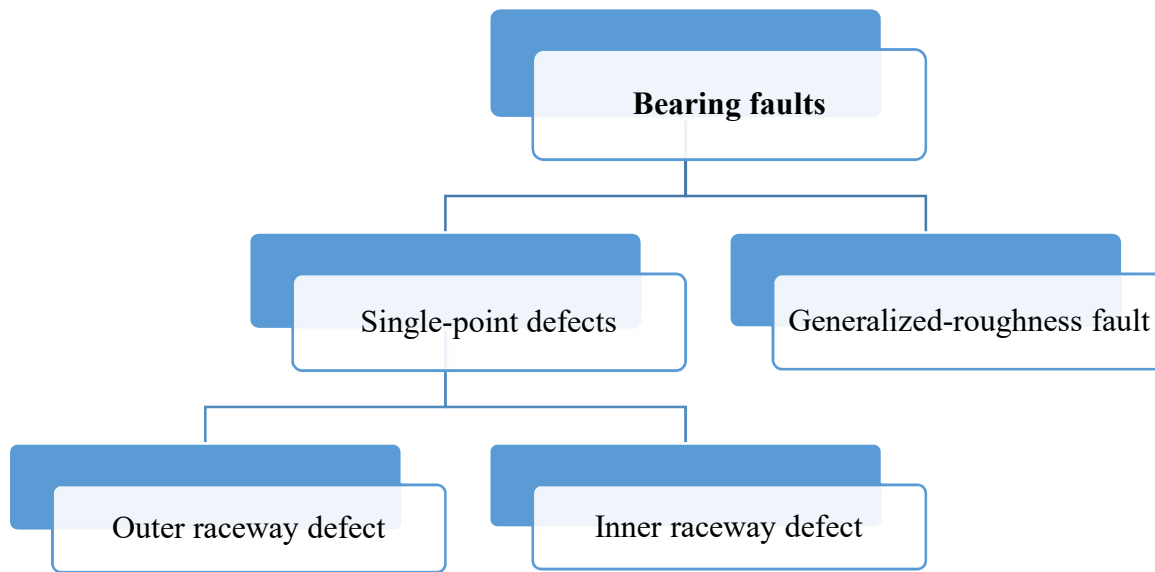
Fig 6.4. Classification of bearing faults

A single-point defect is defined as a single, localized defect on the surface of one of the four bearing elements: the inner raceway, the outer raceway, the cage and the balls. A single-point defect produces a characteristic fault frequency which depends on the surface that contains the fault. A predictable frequency component usually appears in the machine vibration and is reflected in the stator currents. Therefore, most condition monitoring techniques are designed to detect the characteristic fault frequencies, from which the corresponding failures can be detected.

Generalized roughness occurs when the bearing surface has degraded considerably over a large area and, thus, becoming rough, irregular and deformed [5]. This type of failure is found in many industrial installations. The damage on a generalized roughness bearing may not be visible to naked eyes. As there is no single-point defect on the bearing elements, the characteristic fault frequencies are not found in the spectrum of the machine vibration or of the stator currents. Instead, the generalized roughness causes unpredictable broadband effects [6][67]. This signature is often used for the detection of the generalized roughness. Furthermore, the roughness increases friction inside the faulty bearing, which results in an increase of the demanded load torque to the driven machine. This phenomenon can also be used to indicate the presence of the fault.

In a study presented in [68], the inner raceway and outer raceway faults are responsible for up to 90% of all bearing failures. Hence, this work will mainly focus on these two

types of single-point defects. The analysis of the inner and outer raceway defects starts with the derivation of the corresponding characteristic fault frequencies. By taking into account the mechanical structure of a ball bearing, including the load angle α, the number of balls z, and the dimensions of the ball elements, the mechanical angular speed of the cage Ω_c is defined by:

$$\Omega_c = \frac{v_c}{r_c} = \frac{v_i + v_o}{2 \cdot r_c} = \frac{v_i + v_o}{d_c} \tag{6.10}$$

where v_i and v_0 are the angular velocities of the inner and the outer raceways, which are given in (6.11) and (6.12).

$$v_i = \Omega_i \cdot r_i = \Omega_i \cdot \left(r_c - \frac{d_b \cdot \cos \alpha}{2} \right) \tag{6.11}$$

$$v_o = \Omega_o \cdot r_o = \Omega_o \cdot \left(r_c + \frac{d_b \cdot \cos \alpha}{2} \right) \tag{6.12}$$

where r_i, r_0 and r_c are the radius of the inner raceway, outer raceway and cage, respectively; Ω_i and Ω_o are the angular speed of the inner and the outer raceways.

By putting (6.11) and (6.12) in (6.10), the angular velocity of the cage can be found.

$$\Omega_c = \frac{1}{d_c} \left[\Omega_i \cdot \left(r_c - \frac{d_b \cdot \cos \alpha}{2} \right) + \Omega_o \cdot \left(r_c + \frac{d_b \cdot \cos \alpha}{2} \right) \right] \tag{6.13}$$

Ideally the cage and the balls have the same angular velocity. The inner and the outer characteristic fault frequencies are defined based on the relative motion between the balls and the corresponding raceways. Fig 6.5 shows an example of an outer raceway faulty bearing. The damaged area is supposed to be located at the 6 o'clock position and is marked by a blue triangle. Whenever a ball goes over the damaged area, a load torque pulse is created. The frequency of the pulse is the outer raceway characteristic fault frequency.
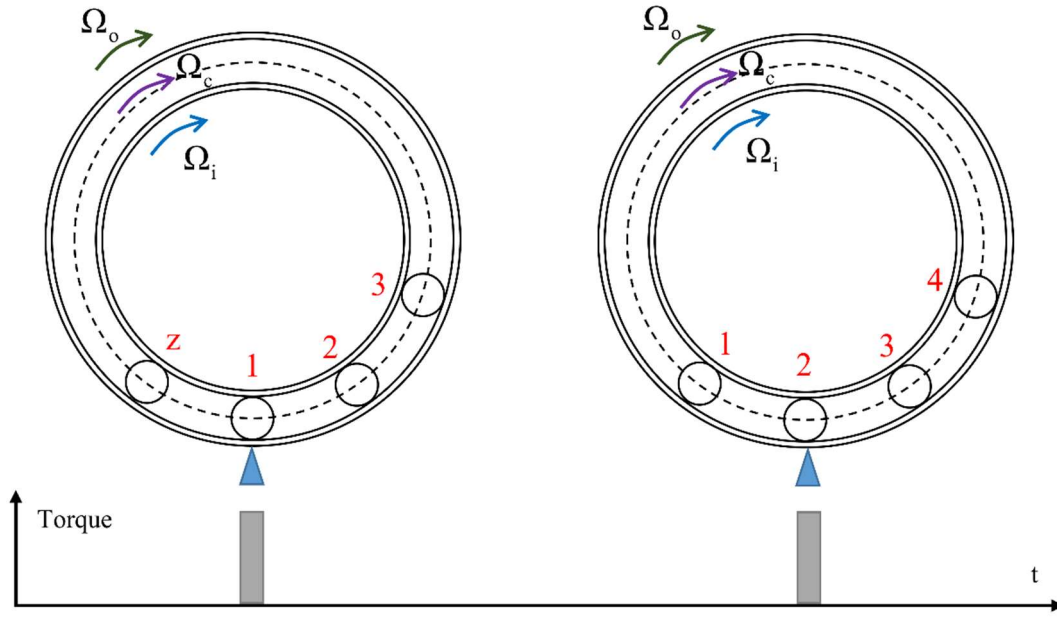
Fig 6.5. Load pulses corresponding to an outer raceway fault

Therefore, the characteristic fault frequency of the outer raceway fault can be calculated by (6.14) [69].

$$
\begin{aligned}
f_{ORF} &= \frac{1}{2\pi} \cdot z \cdot \left| \Omega_c - \Omega_0 \right| \\
&= \frac{1}{2\pi} \cdot z \cdot \left| \frac{1}{d_c} \left[\Omega_i \cdot \left(r_c - \frac{d_b \cdot \cos\alpha}{2} \right) + \Omega_o \cdot \left(r_c + \frac{d_b \cdot \cos\alpha}{2} \right) \right] - \Omega_0 \right| \\
&= \frac{1}{2\pi} \cdot \frac{z}{2} \cdot \left| (\Omega_i - \Omega_o) \left(1 - \frac{d_b}{d_c} \cdot \cos\alpha \right) \right|
\end{aligned}
\tag{6.14}
$$

Similarly, the characteristic fault frequency of the inner raceway fault can be determined by (6.15).

$$
\begin{aligned}
f_{IRF} &= \frac{1}{2\pi} \cdot z \cdot \left| \Omega_c - \Omega_i \right| \\
&= \frac{1}{2\pi} \cdot z \cdot \left| \frac{1}{d_c} \left[\Omega_i \cdot \left(r_c - \frac{d_b \cdot \cos\alpha}{2} \right) + \Omega_o \cdot \left(r_c + \frac{d_b \cdot \cos\alpha}{2} \right) \right] - \Omega_i \right| \\
&= \frac{1}{2\pi} \cdot \frac{z}{2} \cdot \left| (\Omega_i - \Omega_o) \left(1 + \frac{d_b}{d_c} \cdot \cos\alpha \right) \right|
\end{aligned}
\tag{6.15}
$$

Under the assumption that the outer raceway is fixed inside the bearing housing, i.e. $\Omega_0 = 0$, and that the inner raceway rotates at an angular velocity $\Omega_i = \Omega_n$, or at frequency $f_n = \Omega_n/2\pi$, the characteristic fault frequencies given by (6.14) and (6.15) can be rewritten as (6.16) and (6.17), respectively.

$$f_{ORF} = \frac{z}{2} \cdot \frac{\Omega_n}{2\pi} \cdot \left(1 - \frac{d_b}{d_c}\right) \cdot \cos\alpha = \frac{z}{2} \cdot f_n \cdot \left(1 - \frac{d_b}{d_c} \cdot \cos\alpha\right) \tag{6.16}$$

$$f_{IRF} = \frac{z}{2} \cdot \frac{\Omega_n}{2\pi} \cdot \left(1 + \frac{d_b}{d_c}\right) \cdot \cos\alpha = \frac{z}{2} \cdot f_n \cdot \left(1 + \frac{d_b}{d_c} \cdot \cos\alpha\right) \tag{6.17}$$

It can be seen that the inner and the outer characteristic fault frequencies depend on the rotational frequency f_n of the inner raceway, on the mechanical dimension of the bearing, and on the contact angle α. If the necessary information is available, the characteristic fault frequencies can be easily calculated. On the contrary, for a bearing with six to twelve balls, the following approximation formulas can be used [70].

$$f_{ORF} = 0.4 \cdot z \cdot f_n \tag{6.18}$$

$$f_{IRF} = 0.6 \cdot z \cdot f_n \tag{6.19}$$

The outer and inner raceway faults can also be observed at multiples of the characteristic fault frequencies defined by (6.20) and (6.21) in the spectrum of the machine vibration [5] or of the stator currents [4].

$$f_{ORF}^k = k \cdot f_{ORF} \tag{6.20}$$

$$f_{IRF}^k = k \cdot f_{IRF}, \quad k = 1,2,3... \tag{6.21}$$

As can be seen in Fig 6.3, the load zone covers a part of the circumference of the bearing. Evidently, the location of the defect has a great influence on the magnitude of the fault frequency. When the defect rotates through the load zone, an impulse is generated every time a ball passes over the damaged area. The intensity of the shock will be at its greatest magnitude if the defect is located at the point of maximum radial force. Therefore, the most intense impulse is generated on every turn of the machine, assuming that the inner raceway synchronously rotates with the shaft of the driven machine with a frequency f_n. This aspect leads to a phenomenon that the intensity of the defect, which is periodically

generated at f_{IRF}, will be modulated by the mechanical rotation frequency f_n. As the modulated signal produces spectral components at the sum- and difference- frequencies, sidebands around f_{IRF} appear at any frequencies given by (6.22).

$$f_{IRF}^{k,v} = k \cdot f_{IRF} + v \cdot f_n, \ k = 1, 2, 3..., \ v = \pm 1, \pm 2, \pm 3... \tag{6.22}$$

The width of the sideband is defined by:

$$\Delta f^{SB} = f_n \tag{6.23}$$

The intensity of the defect determines the number of detectable sidebands. In addition to the characteristic fault frequency, sidebands can also be used as a signature for the detection of an inner raceway defect.

6.5 Detection of the bearing faults

As mentioned in section 1.2, there are two main methods dedicated to the detection of the bearing faults. The method with the use of the acceleration sensor is more costly than that which does not require an additional sensor. The current work aims to develop a new procedure to detect the bearing faults in repetitive mechanical systems. As the movement of a bearing ball over the damaged areas creates load torque pulses, the spectrum of the load torque contains information related to the bearing defects. Therefore, the spectrum of the load torque can serve as an indicator of the presence of a bearing fault. Also, the proposed method does not require additional sensors [71].

Fig 6.6 illustrates the idea behind the proposed diagnostic procedure. It is necessary to mention again that in case the electric drive is properly designed, the reference torque T_{ref}, which is the output of the speed controller, is considered as a good approximation of the actual load torque T_{load}. The estimated load torque T_{est}, which is obtained by conducting the procedure shown in Fig 5.10, is compared to the approximation of the actual load torque T_{ref}. The difference between the estimated torque and the reference torque designated here as delta torque ΔT is represented in terms of Fourier series by using the FFT algorithm. As the diagnostic procedure is conducted in the steady state, where the reference torque and the estimated torque are periodic functions, the delta torque is also a periodic function. As result, there are dominant harmonics related to the cyclical load torque in the spectrum of the delta torque. To make the diagnostic procedure more reliable, the dominant harmonics that are not related to the characteristic

fault frequencies are filtered in the same way presented in [16]. The remaining spectrum corresponding to a healthy bearing serves as the baseline and is compared to faulty lines. If the two lines have significant differences at f_{ORF} and its multiples, the faulty bearing is diagnosed to have an outer raceway fault. If the differences are visible at f_{IRF} and its multiples and at sideband frequencies $f_{IRF}^{k,v}$, the faulty bearing is diagnosed to have an inner raceway defect. In case the two lines differ from each other in a broad band and the average value of the reference load torque increases significantly, the faulty bearing is diagnosed to have a generalized roughness.
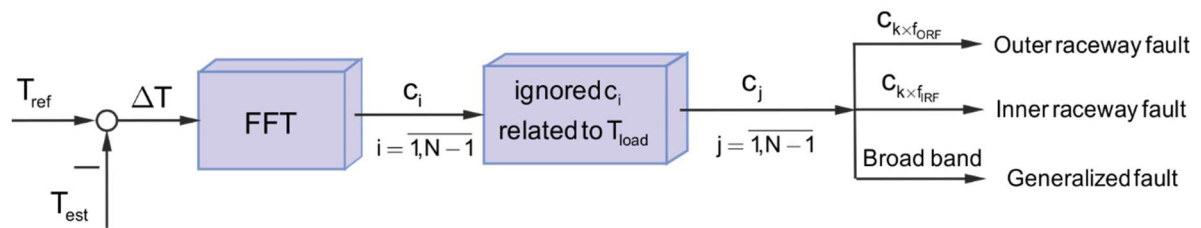
Fig 6.6. Procedure for the detection of bearing faults

6.6 Summary of the chapter

This chapter described the diagnosis of rolling bearing faults. The mechanical structure of a ball bearing was presented, followed by different causes of bearing failures.

The classification of the bearing faults was introduced. From this process, there are two main types of bearing faults including single-point defects and generalized roughness. The characteristic fault frequencies are used for the detection of the faults.

A new diagnostic method based on the load torque estimation was proposed. This method analyzes the spectrum of the delta torque. The spectrum provides necessary information for the diagnosis of the single-point defects as well as the generalized roughness. This approach does not require additional sensors.

7 Experimental Results

7.1 Introduction

In this chapter, experimental results are presented and analyzed to verify the operation of the proposed methods on the estimation of the load torque, the harmonic speed control, the detection of rolling bearing faults and the sensorless control of the drive. First, the structure of the test-bench is introduced, then the two methods dedicated to the load torque estimation as presented in section 5.4 are conducted. The better estimation method is chosen to provide the estimated load torque for the feed-forward control algorithm. The next section will show experiments concerning the harmonic speed controller and is followed by the results on the sensorless control of the drive. The final section focuses on the detection of the rolling bearing faults. Both single-point defect and generalized roughness are investigated by using either the conventional FOC with an encoder for the measurement of the rotor position or the sensorless control scheme.

7.2 Experimental Set-up

The proposed methods were verified through experiments conducted on a laboratory setup as shown in Fig 7.1.

For the digital control implementation, a commercial high performance dSPACE 1104 board is used. The board has the following main characteristics [60]:

- High level programming using Matlab-Simulink and a C complier
- A power PC 603e processor with a slave TMS320C2000 DSP controller
- Eight ADC converters: one ADC converter is multiplexed to four channels with 16-bit resolution, other four parallel channels with 12-bit resolution
- Eight parallel DAC converters with 16-bit resolution
- Two incremental encoder channels working with both TTL and sine/cosine signals
- Twenty digital I/O
- One three-phase PWM unit and four single-phase PWM units
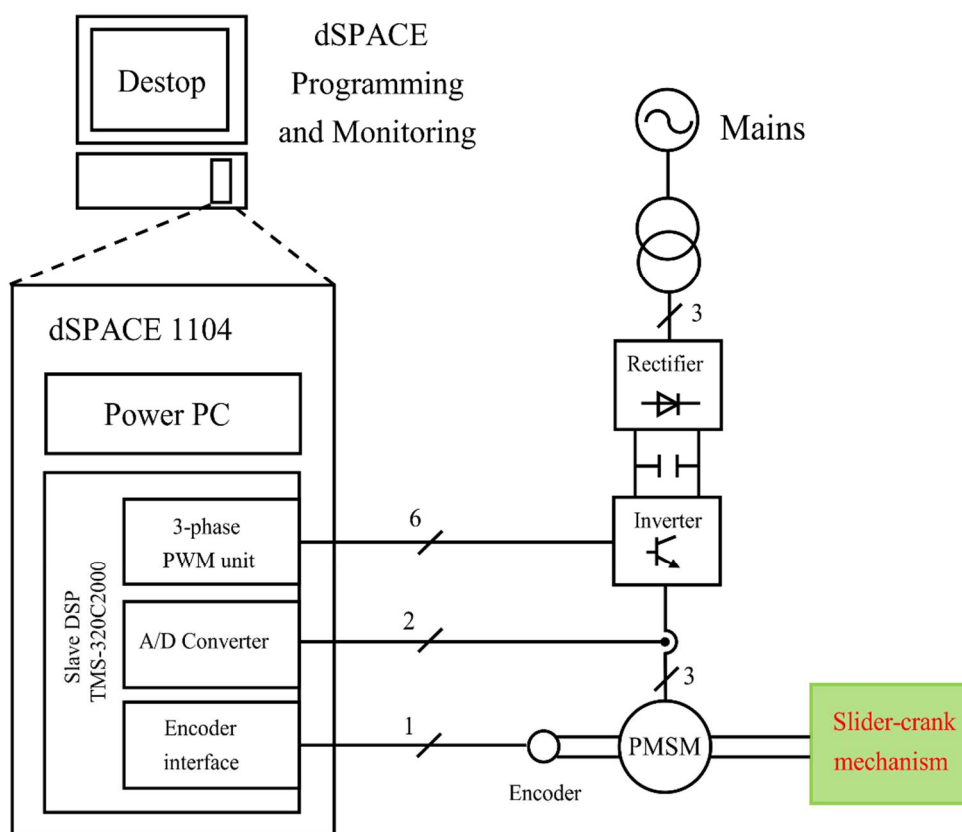
Fig 7.1. Simplified configuration of the experimental set-up

The controller board generates firing pulses for controlling the IGBTs inside a two-level voltage source inverter including a suitable dead-time to avoid DC-link short circuit. A standard space phasor modulation with a switching frequency of 5 kHz is considered in the present work. The dSPACE 1104 board communicates with the PC via the Control desk software for the purposes of monitoring.

An incremental sine/cosine encoder with 2048 increments per revolution assembled in the driven machine is used for the measurement of the rotor position of the driven machine. The currents of two phases are measured by two Hall-effect current transducers. The DC-link voltage used for the space phasor modulation is measured by using resistors and amplifiers.

As depicted in Fig 7.2, a surface-mounted PSMS is used to move the horizontal slider-crank mechanism. The parameters of the machine and of the mechanism are given in appendix 9.1 and 9.2, respectively. There are two bearings installed in between the machine and the mechanism: one is on the motor side while the other is on the load side.

The mechanical configuration of the mechanism can be changed by adding a mass to the slider or changing the position of the articulated joint between the connecting rod and the crank.
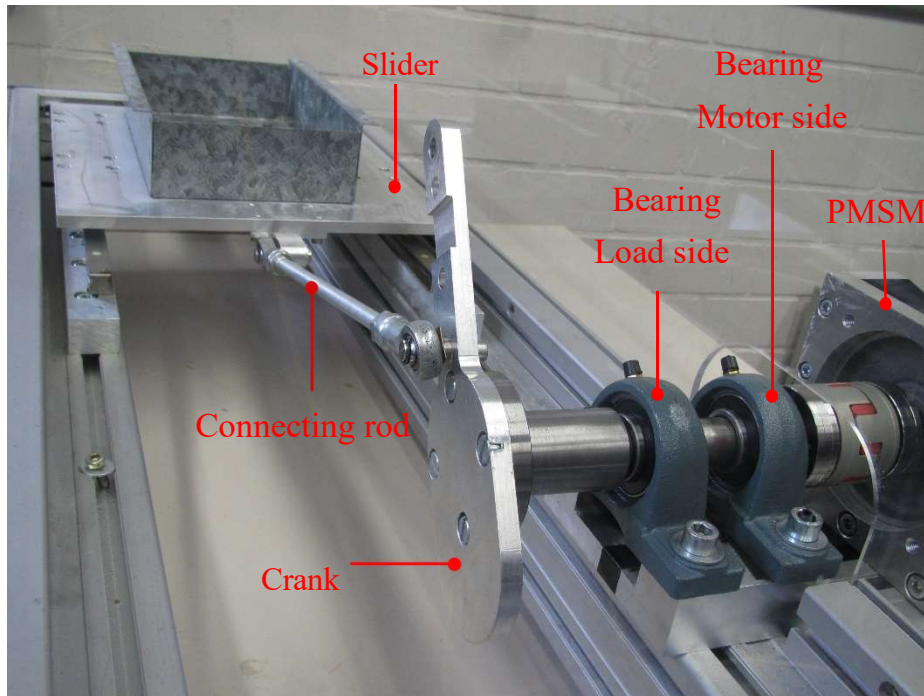
Fig 7.2. Horizontal slider-crank mechanism driven by a PMSM

7.3 Load torque estimation and feed-forward control

The first experiment for the load torque estimation is conducted by applying either the phenomenological or the look-up table method. Fig 7.3 depicts a block diagram of the test bench including the control scheme. The installed encoder in the PMSM is used for the measurement of the rotor angle. The Fourier coefficients are identified based on a sliding window method with $N = 500$ samples per period as given in equation (5.18) in section 5.4. Harmonics up to the 5th in the spectrum of the load torque are considered as they ensure the desirable estimation precision of the load torque and the algorithm simplicity.

The mechanism was driven in the velocity control mode with different values of the reference speeds within its operational range: 3 min^{-1}, 5 min^{-1}, 7 min^{-1}, 10 min^{-1}, 15 min^{-1}, 20 min^{-1}, 25 min^{-1}, 30 min^{-1}, 40 min^{-1}, 50 min^{-1}, 60 min^{-1}, 70 min^{-1}, 80 min^{-1}, 90 min^{-1}, 100 min^{-1}. The *estimation* switch in Fig 7.3 was closed to enable the *sliding window* block to work with two inputs including the reference current in the q-axis for the

calculation of the reference load torque $T^* = k \cdot i_q^*$, where k is a constant of the machine, and the crank angle γ_m. It is necessary to mention that the precision of the crank angle strongly affects the precision of the estimation algorithm. Therefore, the initial value of the angle have to be determined during the commissioning of the system. The Fourier coefficients obtained from the estimation process are depicted in Fig 7.4.

Fig 7.3. Block diagram of the experimental set-up for the load torque estimation according to section 5.3
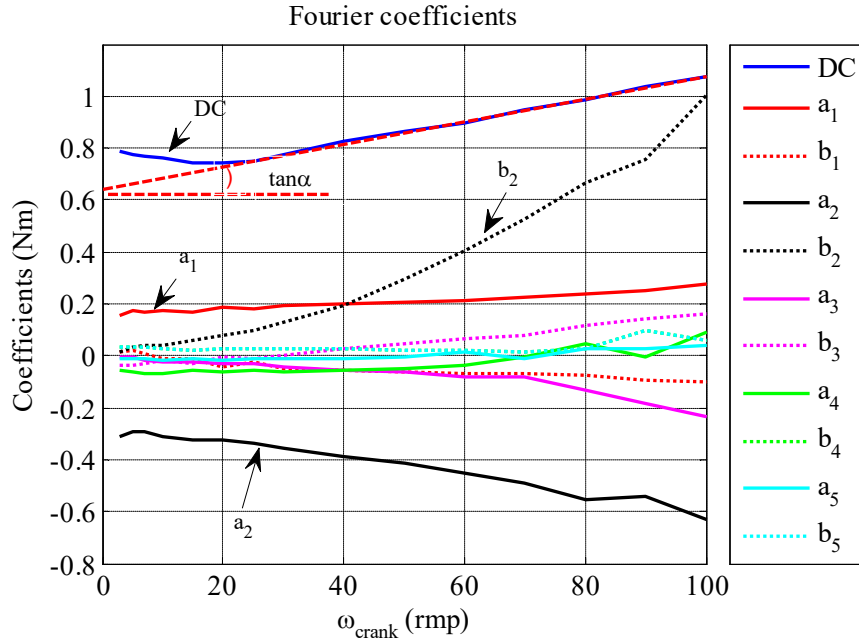
Fig 7.4. Fourier coefficients of the load torque at different velocities

Fig 7.4 shows that the dependency of b_2 on the crank angular velocity Ω_m resembles a parabola. This behavior agrees with the calculation of b_2 in Table 5.3. Furthermore, it can be seen that the shape of the DC component a_0 is similar to that of the total friction force in Fig 5.2(e). The linear region ranges from 25 min^{-1} to 100 min^{-1}. As already mentioned in section 0, the straight dotted red line connecting the two points on the border of the linear region characterizes the linear behavior of the friction model of the mechanism. The Coulomb and the viscous constants are identified based on the slope of the straight dotted red line and its intersection with the vertical axis, respectively, and result to be:

$$K_v = 33.64\,Ns\,/\,m; \quad K_c = 20N \tag{7.1}$$

The phenomenological method for the load torque estimation can be carried out after the identification of K_v and K_c. In addition, the two steps of the look-up table based method illustrated in Fig 5.10 can also be performed by using the coefficients depicted in Fig 7.4. For the operation of the system with a feed-forward control, the switch in Fig 7.3 is closed and the system works with a compensation of the load torque. The estimated load torque acts as a compensation signal in the speed control loop. It is assumed that the load torque is compensated at $t = 2s$.

Fig 7.5 shows the reference torque and the estimated torque before and after the load torque compensation. Fig 7.6 depicts the compensation load torque while Fig 7.7 shows the speed responses with and without the load torque compensation. It can be seen in Fig 7.7 that both methods improve the speed response quality in the steady state by considerably reducing the tracking error. However, the look-up table based method ensures smaller speed oscillation as it yields a more precise load torque estimation as shown in Fig 7.5. One of the reasons for this behavior is, unlike the phenomenological method, the look-up table method takes into account the effects of the nonlinear friction.
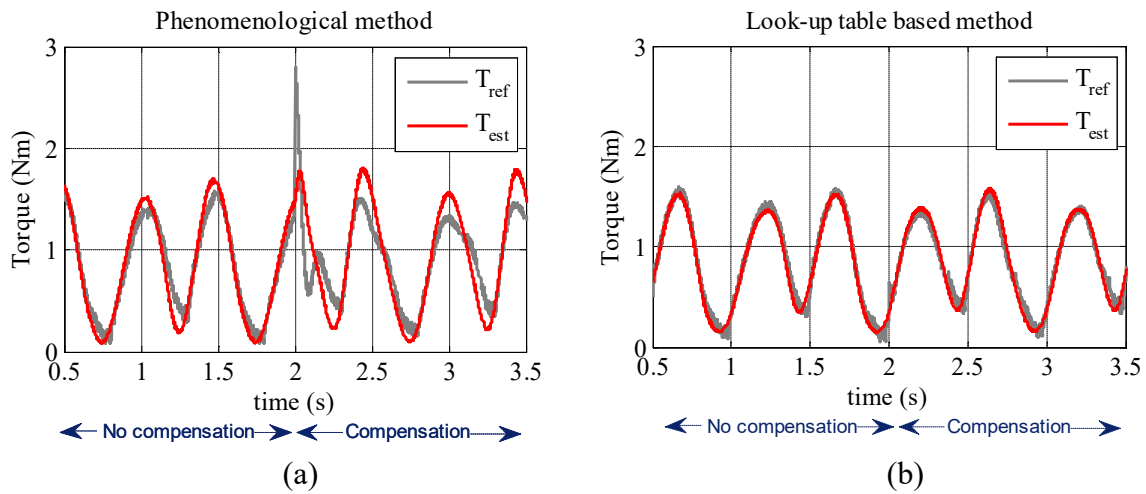
Fig 7.5. Reference torque and estimated torque: a) theory based method; b) look-up table based method
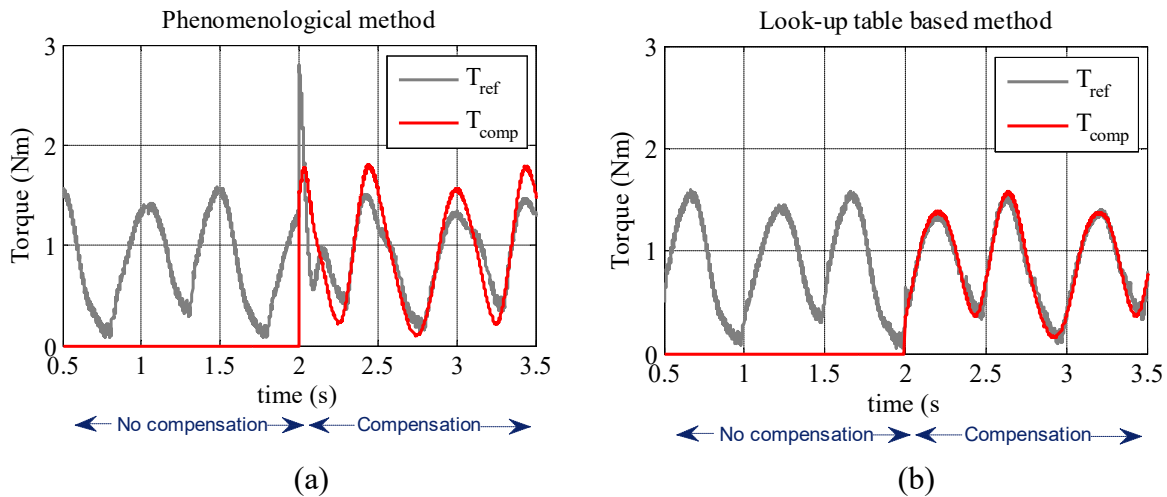
Fig 7.6. Reference torque and compensation torque: a) phenomenological method; b) look-up table based method
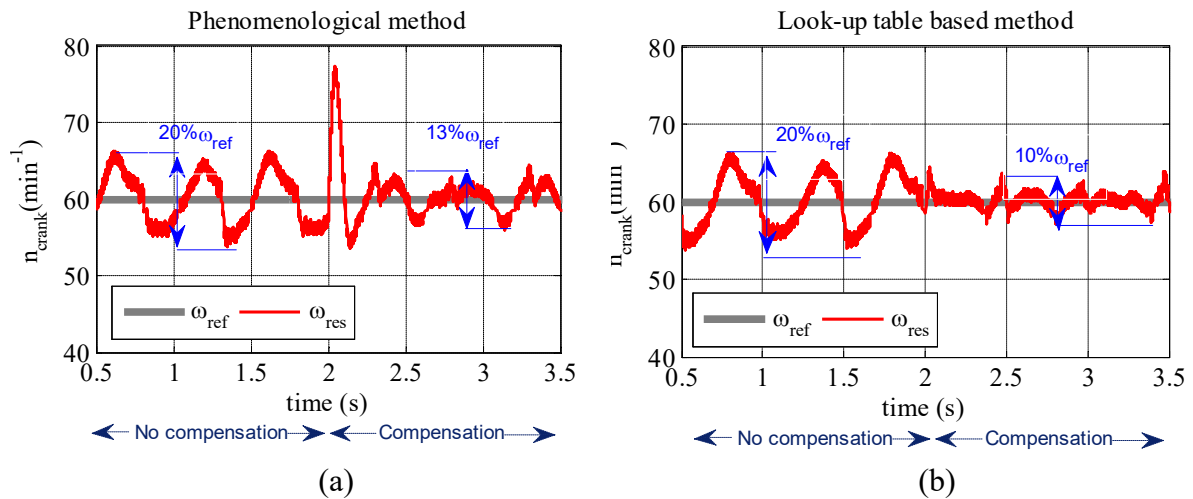
Fig 7.7. Reference speed and response speed: a) phenomenological method; b) look-up table based method

The effectiveness of the look-up table method was verified by two other experiments associated with the changes of the mechanical configuration. For the calculation of the look-up table, the reference speed was set to 55 min^{-1}. First, r_1 as shown in Fig 5.1 was changed from 55 mm to 85 mm, the corresponding results are depicted in Fig 7.8. The increase of r_1 leads to the increase of the load torque as it is defined by equations (5.11) -(5.15) in section 5.3.

As seen in Fig 7.8 (a), the look-up table method still provides a good estimation result. Fig 7.8 (c) demonstrates that the speed oscillation is significantly reduced by the feed-forward control algorithm. For the second configuration, a mass of 1.7 kg was added to the slider. The corresponding results depicted in Fig 7.9 show that the look-up table method still works well in this case.

(a)

(a)

(b)

(b)

(c)

(c)
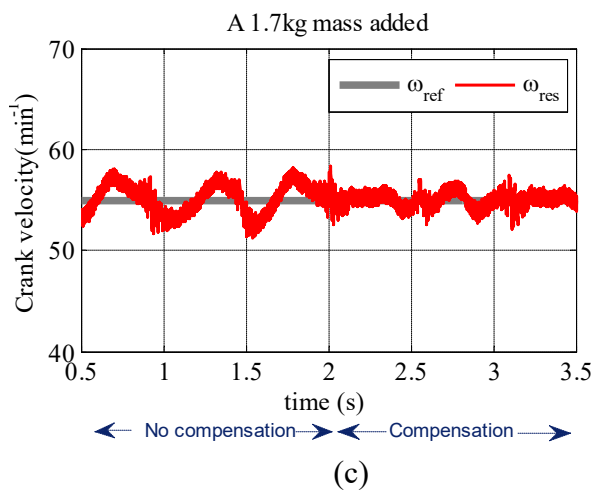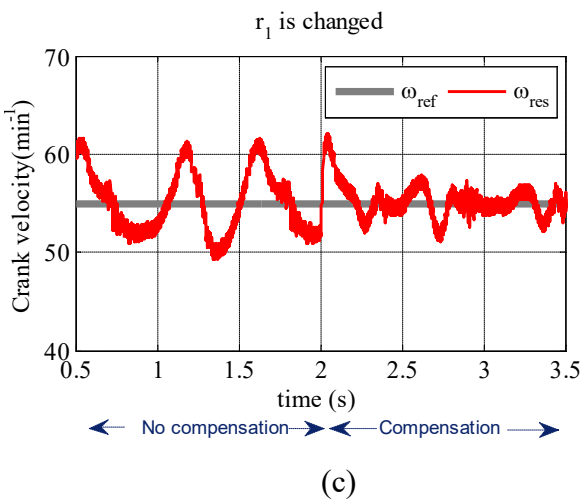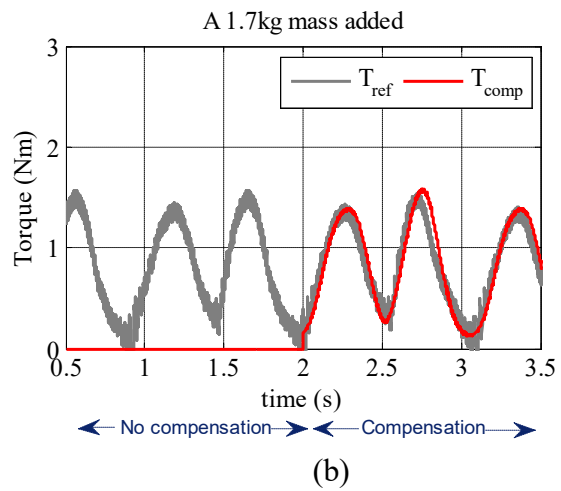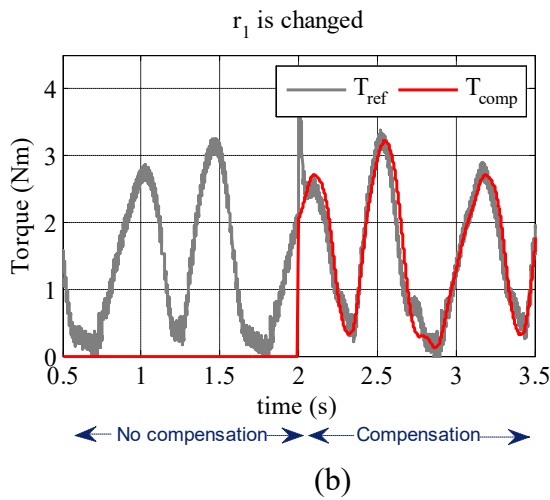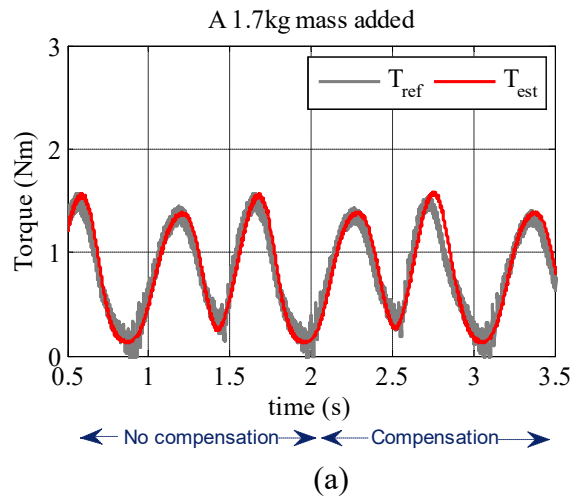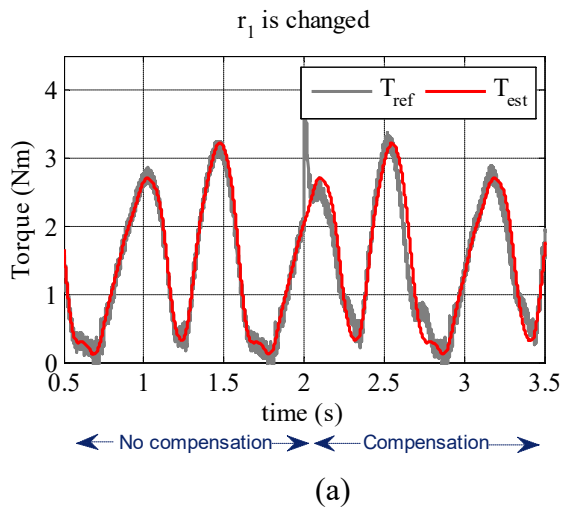
Fig 7.8. r_1 is changed from 55 mm to 85mm: a) reference and estimated load torque; b) reference and compensation load torque; c) reference and response speed

Fig 7.9. A 1.7-kg mass is added to the slider: a) reference and estimated load torque; b) reference and compensation load torque; c) reference and response speed

The next experiment refers to the operation of the feed-forward control algorithm in dynamic mode. To do so, three compensators were tested:

i-   No load torque compensation

ii- The compensation load torque is obtained by using the look-up table based method

iii- The compensator ii) augmented with the acceleration component $J_{total} \cdot \frac{d\omega_m}{dt}$

The compensator iii) being as the compensator ii) is based on the look-up table method, in which the Fourier coefficients were achieved in the steady state, meaning that the effect of the acceleration load torque component was ignored.

To evaluate the operation of the three compensators, a reference speed with a 60 min^{-1}/s- slope was used. The final reference speed was set to 60 min^{-1}. Fig 7.10 shows that the speed responses were improved by applying the load torque compensation in both dynamic and steady states. Furthermore, the compensator iii) works more effectively than the compensator ii) only in the low-speed region since the augmented term can be compared to other terms when the crank is driven at low-speeds.
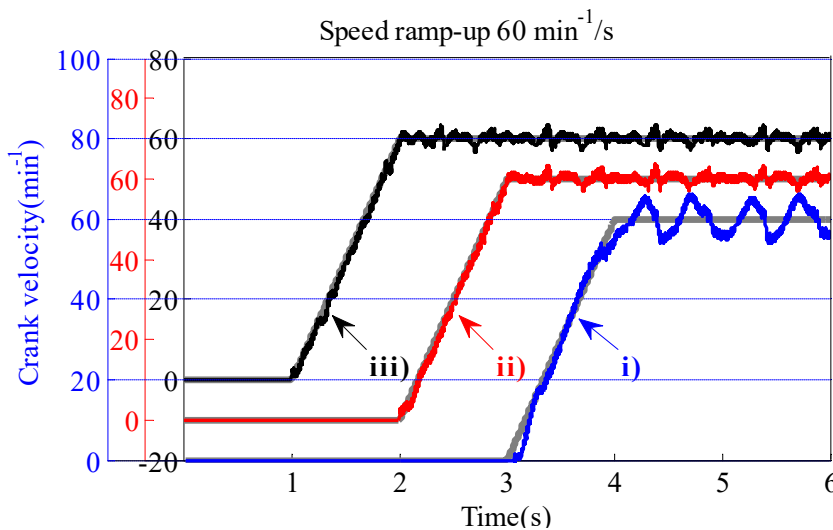
Fig 7.10. Speed responses corresponding to the three compensators

7.4 Harmonic speed control

Experiments related to the harmonic speed control are conducted with two objectives. One is to improve the speed response quality and the other is to estimate the load torque. Both the objectives will be presented hereafter.

7.4.1 Velocity control

 For the first purpose, a ramp-up reference speed with a slope of 60 min^{-1}/s and a final value of 80 min^{-1} was utilized. The conventional PI-speed controller and a harmonic speed controller were implemented and compared, in which harmonic up to the 5th were taken into account.

Fig 7.11 and Fig 7.12 show the speed responses and the spectrum of the speed oscillations corresponding to the conventional and the harmonic speed controller. It can be seen in Fig 7.11 that the harmonic speed controller works more effectively than the conventional one in both dynamic and steady states. The speed error in the steady corresponding to the harmonic controller is around 4 min^{-1}, or 5% ω_{ref} while that of the conventional controller is 16 min^{-1} or 20% ω_{ref}. In the ramp-up time, the harmonic controller provides better reference speed tracking. Spectrum analysis of the speed error in the steady state shown in Fig 7.12 proves that harmonics up to the 5th were considerably diminished by the harmonic speed controller, because, as already mentioned, harmonics up to the 5th were considered.
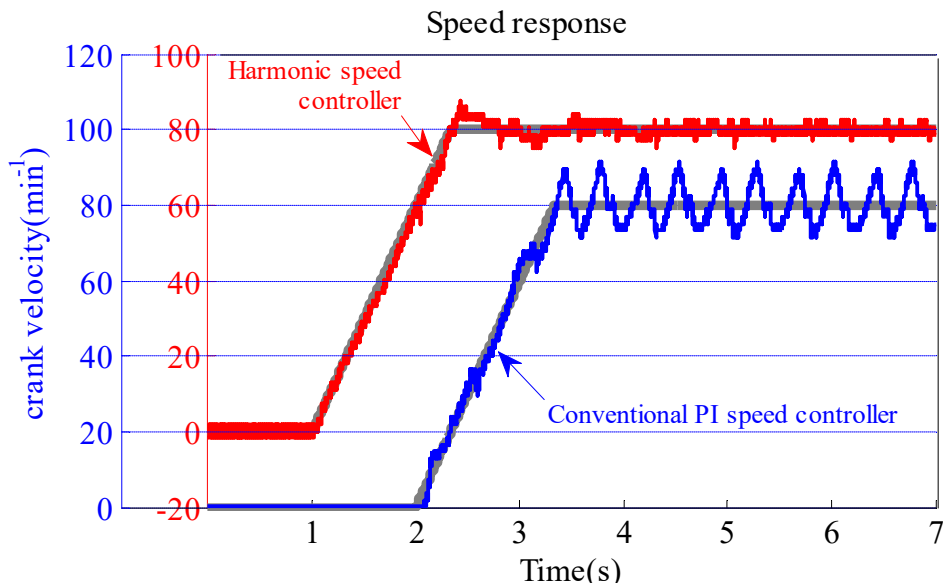
Fig 7.11. Speed responses corresponding to the harmonic speed controller and the conventional PI speed controller
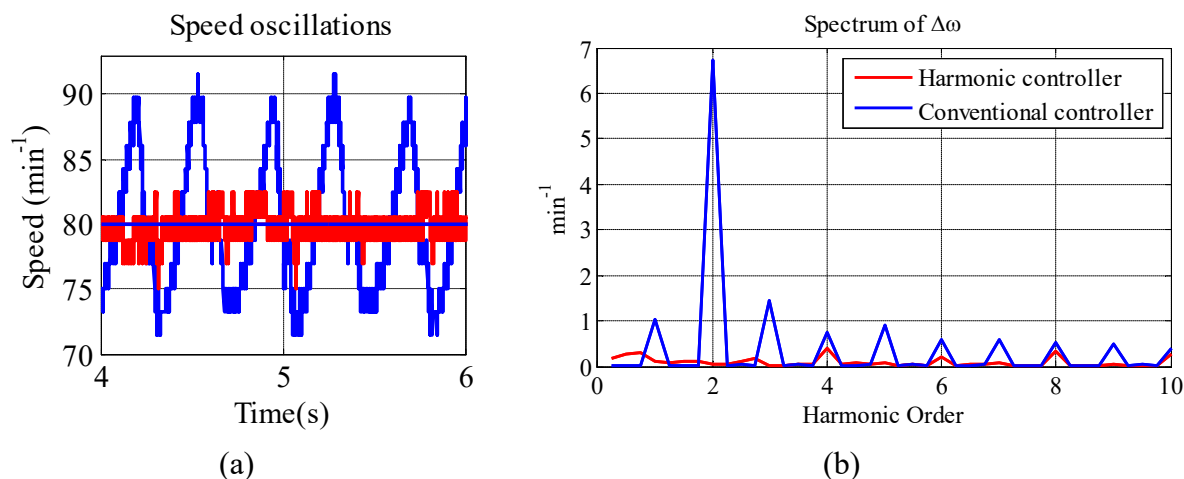
Fig 7.12. a) Speed oscillations; b) spectrum of the speed oscillations

The next comparison is made among the harmonic controller, the PI-R controller, and the feed-forward controller. The feed-forward algorithm is based on the compensator ii) as it was introduced in section 7.3. A ramp-up reference speed with a 180 min^{-1}/s-slope was utilized. The slope was set higher than those in the former experiments in order to make the speed control loop work with higher dynamics.

Fig 7.13 depicts the reference speed tracking corresponding to the three configurations of the speed controller. It can be seen that the harmonic and the resonant speed controllers provide better speed responses than the feed-forward speed controller as they ensure smaller speed oscillations. It is necessary to note that the resonant parts were allowed to take effect when the absolute angular speed of the crank Ω_m is higher than 5 min^{-1}, because the resonant and the anti-resonant frequencies proposed by the resonant parts are identical in zero speed and may lead to unpredictable behaviors of the speed control loop.
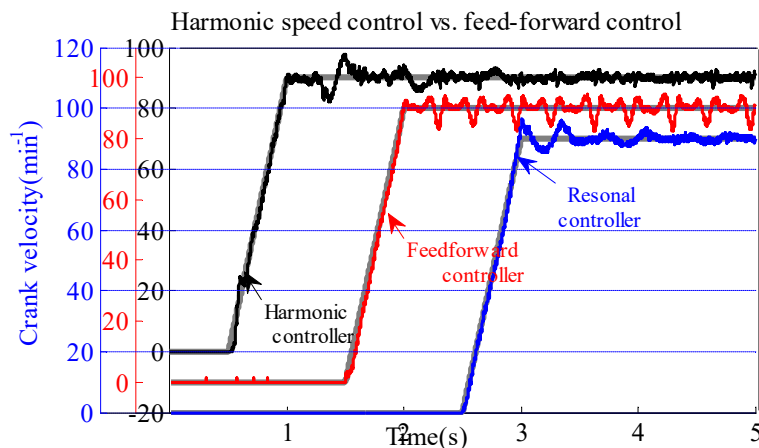
Fig 7.13. Reference speed tracking of the three configurations of the speed controller

7.4.2 Estimation of the load torque

The second purpose related to the load torque estimation starts with the evaluation of the Fourier coefficients. Instead of using the sliding-window method, the coefficients can be obtained directly from the output of the corresponding harmonic controllers as shown in Fig 5.6.
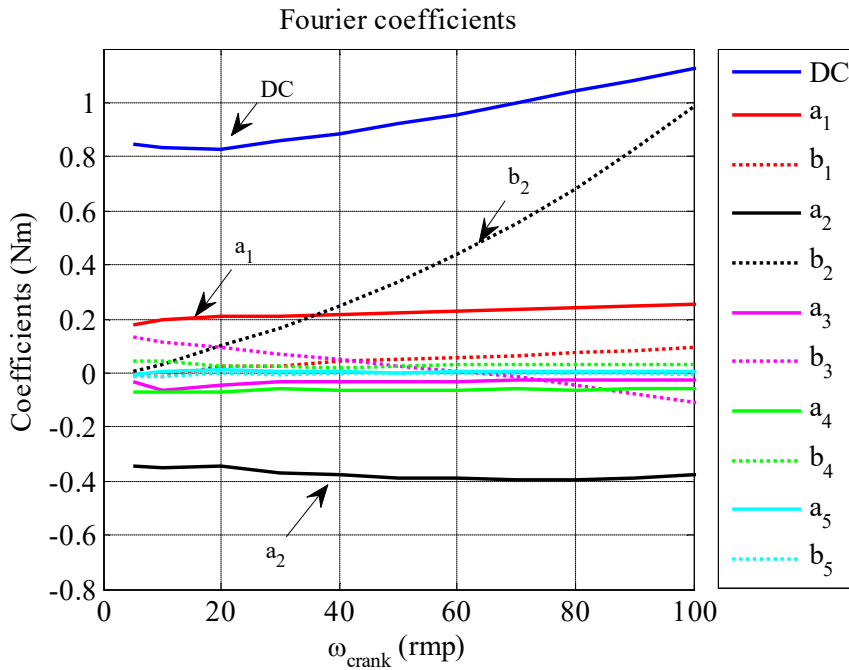
(a)
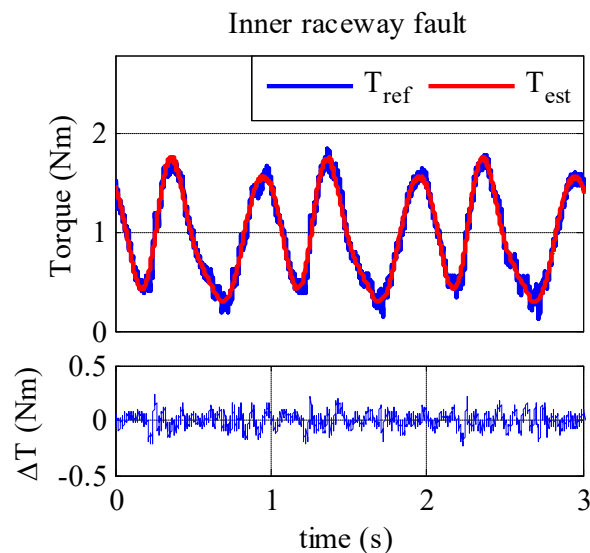
(b)

Fig 7.14. Estimations based harmonic speed controller: a) Fourier coefficients; b) load torque

Fig 7.14(a) shows the results of the estimation of the Fourier coefficients based on the structure of the harmonic speed controller. Fig 7.4 and Fig 7.14 show that the sliding-

window method and the harmonic speed controller provide similar estimation values of the coefficients. After obtaining the coefficients, the load torque can be estimated by using the look-up table method, from which the load torque can be estimated as it is depicted in Fig 7.14(b). It is observed that the estimated load torque precisely tracks the reference load torque. This promising result will be used in another experiments related to the detection of the bearing faults.

7.5 Sensorless control of the drive

Until now, experiments on the load torque estimation and on the harmonic speed control are based on an encoder for the measurement of the rotor angle and rotor speed. The experiments shown in the following sections will focus on the sensorless control of the drive, where the rotor position and rotor speed are obtained from a field observer as mentioned in section 4. The installed encoder in the driven machine is used only for the purpose of comparison between estimated and measured values. As the slider-crank mechanism is operated from 0 min^{-1} to 100 min^{-1} corresponding to 0-3.3% rated speed of the driven machine, the high-frequency injection technique is adopted for the sensorless operation.

7.5.1 Low-speed sensorless control of the drive

The first step to implement the high-frequency injection technique is related to the selection of the alternating high-frequency injected voltage. Equation (4.14) demonstrates that the sensitivity of the injection method depends on coefficient K_{err}, which can be rewritten as follows:

$$K_{err} = \frac{\hat{u}_h}{\omega_h} \cdot \frac{L_{dh} - L_{qh}}{2 \cdot L_{qh} \cdot L_{dh}} \approx \frac{\hat{u}_h}{2 \cdot |z_{dh}|} \cdot \frac{L_{dh} - L_{qh}}{L_{qh}} \tag{7.2}$$

If the magnitude of the high-frequency current on the d-axis is kept unchanged, or in other words the first term of the product on the right hand side of (7.2) is a constant, then K_{err} only depends on the difference between the $d-$ and $q-$axis high-frequency inductances. Hence, the measurement of the high-frequency inductances is crucial in order to choose a suitable injected frequency. For doing so, a pure sinusoidal voltage generated by a high-power generator with a frequency range $400 \div 3000(Hz)$ and an amplitude $\hat{u}_h(V)$ was applied to the windings phase U and phase V of the machine. Phase W was opened.

$$u_{UV}(t) = \hat{u}_h \cdot \sin\left(2 \cdot \pi \cdot f_h \cdot t\right) \ , V; \ \hat{u}_h = 20V; \ f_h = 400 \div 3000 Hz \tag{7.3}$$

The rotor of the machine was slowly rotated to detect the maximum RMS value I_{max} and the minimum RMS value I_{min} of the current flowing in the windings. The high-frequency inductances corresponding to the d- and q-axis can be determined by the following equations:

$$
\begin{aligned}
L_q(f_h) &= \frac{\hat{u}_h}{2 \cdot \sqrt{2} \cdot I_{min} \cdot 2\pi \cdot f_h} \\
L_d(f_h) &= \frac{\hat{u}_h}{2 \cdot \sqrt{2} \cdot I_{max} \cdot 2\pi \cdot f_h}
\end{aligned}
\tag{7.4}
$$

Fig 7.15 (a) shows the measured high-frequency inductances while Fig 7.15 (b) depicts the inductance difference, i.e. the last term of the product on the right hand side of equation (7.2).

(a) (b)
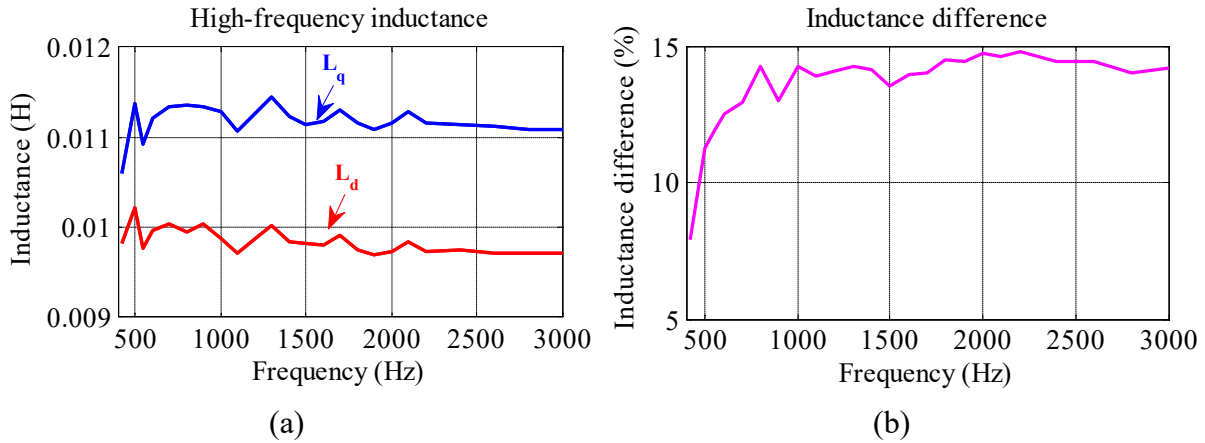
Fig 7.15. a) High-frequency inductances; b) difference inductance of the d- and q- axis

The selection of the injected frequency is carried out by taking into account the capability of the microprocessor or DSP and the sensitivity of the injection method [48]. Generally, the higher the injected frequency, the higher the dynamic of the field angle observer, and as a result the faster the speed response. However, the increase of the injected frequency demands a higher magnitude of the carrier voltage to make sure that the magnitude of the high-frequency current is large enough to be compatible with the resolution of the ADC converters built in the microprocessor. Furthermore, coefficient K_{err} should be as high as possible because its value determines how sensitive the method reacts to the field error angle. By considering all these factors, an alternating carrier voltage signal with frequency of $f_h = 625 \ Hz$ and having amplitude of $\hat{u}_h =$

$20\ V$ is chosen. The sampling frequency and switching frequency of the whole control system are synchronized and set at 5 kHz. The DC-link voltage is set to $U_{dc} = 300\ V$ for reducing the adverse effects of a dead-time $T_{dead} = 3\ \mu s$ originated from the inverter equipped in the electric drive. At the injected frequency, the d- and q-axis inductances are:

$$L_{dh} = 10\ mH; \ L_{qh} = 11.2\ mH \tag{7.5}$$

The low-pass filter in the demodulation procedure shown in Fig 4.4 is designed with $\beta_{lp} = 500\ Hz$. The parameters of the PI controller in the phase-locked loop can be determined according to (4.18):

$$k_p = 6109\ rad\ /\ As; \ k_i = 339369\ rad\ /\ As^2 \tag{7.6}$$

The dynamics of the field angle tracking algorithm was tested with a step response of the field angle by forcing the estimated angle at an initial value of zero. Fig 7.16 shows that the rise-time of the estimation response is $20\ ms$ for a reference angle of $1.05\ rad$, while the steady state error angle stays in the limits to $0.1\ rad$ or 5.7^0 electrical degrees. The next experiment is related to the measurement of the error signal $f(\Delta\gamma)$ as a function of the error angle $\Delta\gamma$. From (4.12) and the demodulation procedure depicted in Fig 4.4, the error signal $f(\Delta\gamma)$ can be defined as follows:

$$f\left(\Delta\gamma\right) = \frac{\hat{u}_h}{\omega_h} \cdot \frac{L_{dh} - L_{qh}}{4 \cdot L_{qh} \cdot L_{dh}} \cdot \sin(2\Delta\gamma) \tag{7.7}$$

For small value of the error angle $\Delta\gamma$, (7.7) becomes (4.14). To conduct the experiment, the alternating carrier high-frequency voltage is injected into the $\alpha -$axis of the α, β-coordinate system while running the PMSM with an encoder for position feedback. While the rotor rotates, the error angle $\Delta\gamma$ changes. The error signal $f(\Delta\gamma)$ and the error angle $\Delta\gamma$ were recorded and are shown in Fig 7.17. It can be seen that the shape of $f(\Delta\gamma)$ resembles a sinusoidal signal whose period is equal to half of that of the error angle $\Delta\gamma$. This phenomenon agrees with the theoretical determination of the $f(\Delta\gamma)$ given in (7.7) . It is necessary to mention that the demodulation procedure provides the estimation angle γ_e which either indicates the correct direction of the magnetic flux, or it is in error by a displacement of $\pi\ rad$. Therefore, the magnet polarity of the rotor has to be determined in order to obtain the correct direction of the pole flux [21].
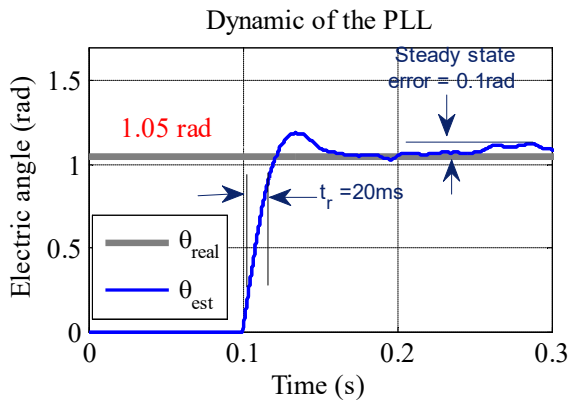
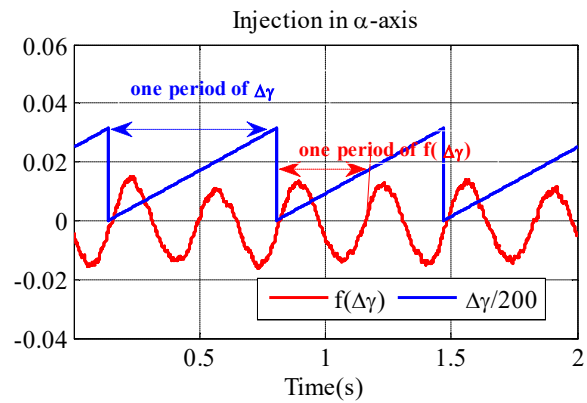Fig 7.16. Step response of the field angle tracking algorithm

Fig 7.17. Error signal corresponding to one period of the error angle

The sensorless control algorithm based injection technique was utilized for the operation of the drive. To evaluate its operation, a reference speed with a 60 min^{-1}/s-slope was used. Fig 7.18 and Fig 7.19 show the results by using a conventional PI speed controller and a harmonic speed controller without the use of mechanical encoder. The harmonic speed controller was also designed up the 5th harmonic.

Fig 7.18(a) and Fig 7.19(a) show that the sensorless control system can handle very low-speeds including standstill. However, the harmonic speed controller provides better speed reference tracking by canceling cyclic speed oscillations originated from the periodic load torque. The results are similar to those obtained by using an encoder for the angle measurement as presented in section 7.4. The remaining speed error comes from the resolution of the ADC and the noise buried in the current measurement. Fig 7.18 (b)-(c) and Fig 7.19 (b)-(c) show that the angle tracking algorithm works well by limiting the error angle to approximately six electrical degrees.

In order to get a deeper insight into the reasons for the ripples in the estimate of the speed, the impact of the ADC quantization was carried out. The 12-bit ADC converters of the DSP built in the dSPACE 1104 board are capable of working with analog voltage inputs ranging from -10V to +10V. This means that the resolution of the ADC converter is $20V/2^{12} = 4.883\ mV$. The current measurement circuit was designed with a ratio from the measured current to the output voltage of $K_{iu} = 0.98\ A/V$. Hence, the resolution of the current measurement is $K_{iu} \cdot 4.883mV = 4.785\ mA$. Fig 7.20 shows the magnitude of the ripples that can be observed at some points in the demodulation procedure at the injected frequency $f_h = 625\ Hz$ and the amplitude of the injected high-frequency voltage is $20\ V$.
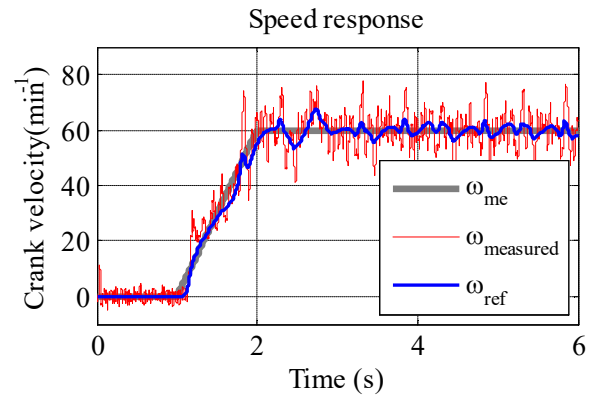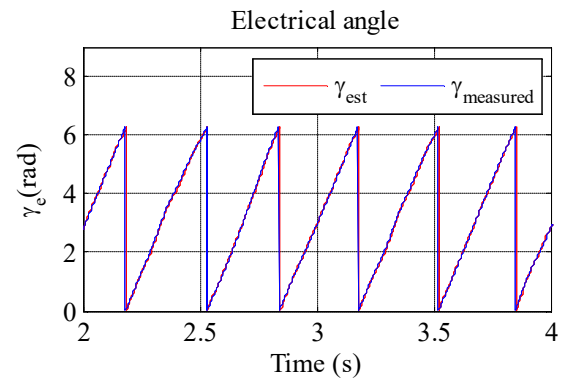
Speed response

Electrical angle

Electrical error angle
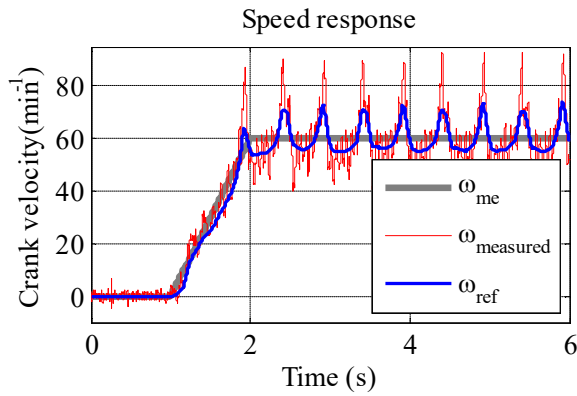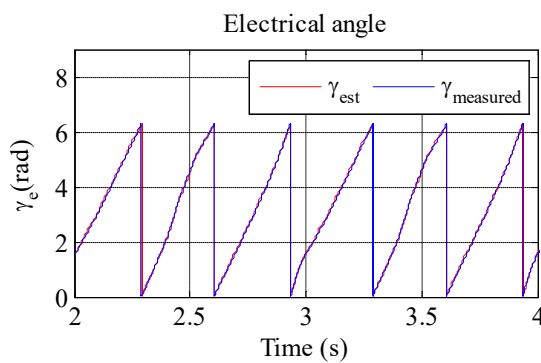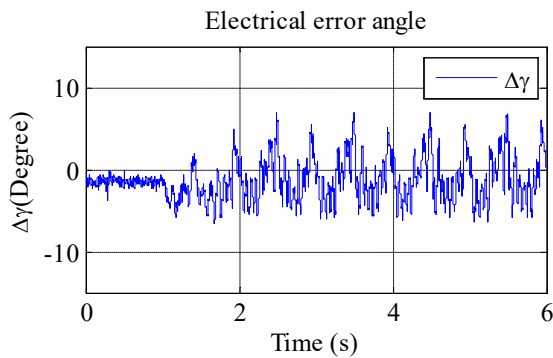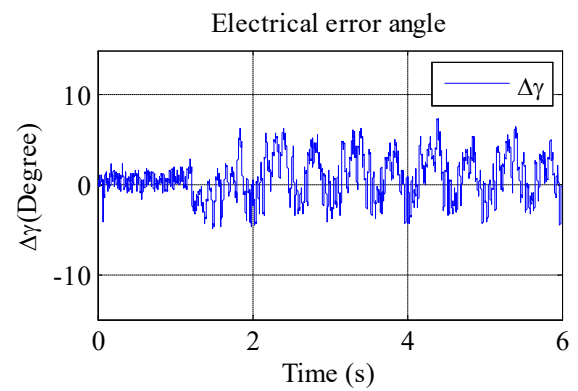
Fig 7.18. Conventional PI speed controller:
a) speed response; b) measured and
estimated field angle; c) error angle

Fig 7.19. Harmonic speed controller: a)
speed response; b) measured and estimated
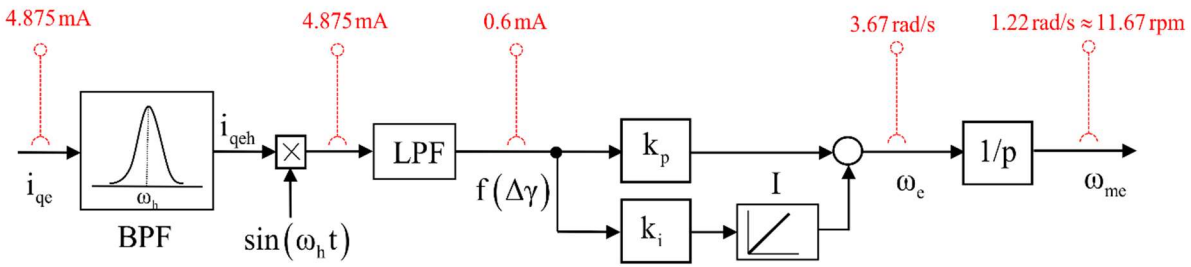field angle; c) error angle

Fig 7.20. Ripples of 625Hz-signals in the demodulation procedure coming from the resolution of the A/D converters

Fig 7.20 shows that the estimated crank velocity has a ripple of $11.67\ min^{-1}$ originated from the resolution of the ADC converters. The speed ripples can be observed in Fig 7.18(a) and Fig 7.19(a). One solution to reduce the ripples is reducing the current measurement coefficient K_{iu}. However, the decrease of K_{iu} results in a smaller current the ADC converter can handle. A tradeoff between the estimated speed quality and the range of the current measurement has to be made.

7.5.2   Wide speed sensorless control of the drive

In this section, a combined field angle observer is implemented to drive the PMSM in a wide speed range. The transition speed was set to $\omega_{trans} = 200\ min^{-1}$. The alternating high-frequency carrier voltage was selected in the same manner presented in section 7.5.1. It is necessary to mention that the parameters of the low-pass filter and the PI controller in the PLL depend on the estimated rotor speed. The PLL has to be programmed in such a way that it can adapt to the variable speed.

Fig 7.21 to Fig 7.24 show the results corresponding to the combined angle estimator. As depicted in Fig 7.21, the speed was smoothly changed in the range $[-700; 700]\ min^{-1}$ corresponding to $[-0.23; 0.23]$ p.u. The signal injection method takes effects when the speed is in the range between $[-200; 200]\ min^{-1}$ according to the predefined transition speed ω_{trans}. This phenomenon is clearly observed in the figure representation of the error signal $f(\Delta\gamma)$ in Fig 7.23. The estimated and the measured field angles are depicted in Fig 7.22, while the error angle is shown in Fig 7.24. It can be seen that the combined estimator limits the error angle to approximately ten electrical degrees in the steady state and eighteen electrical degrees in the transition region.
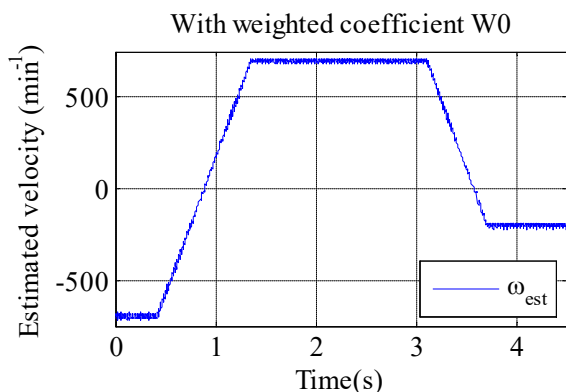
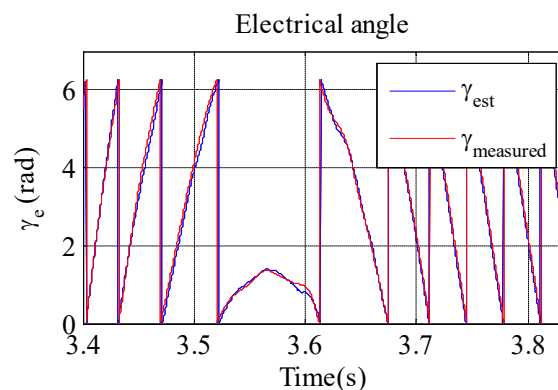Fig 7.21. Speed response with a combined estimator

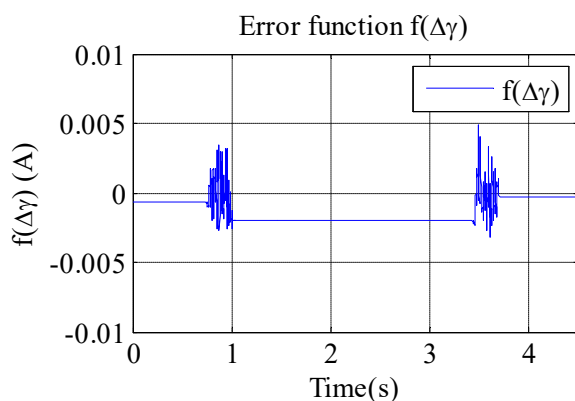Fig 7.22. Estimated and measured field angles
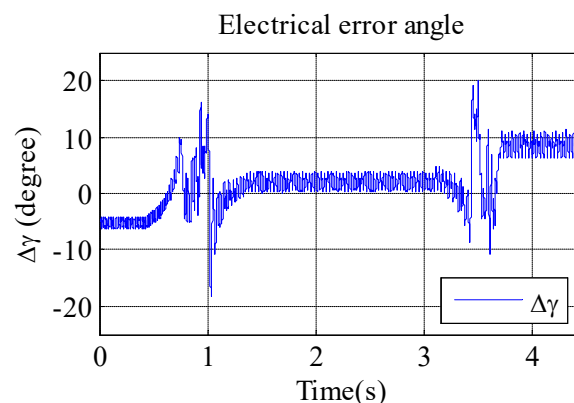

Fig 7.23. Error signal in the PLL

Fig 7.24. Error angle

The next experiment was conducted for the comparison between the combined estimators with and without the use of the weighted coefficient W_0. Fig 7.25 (a) shows that the speed was smoothly changed in the low-speed region including zero crossing with the combined estimator augmented by the weighted coefficient. On the contrary, the speed response according to the estimator without the weighted coefficient is noisy in the low speed region as it is shown in Fig 7.26 (a). In addition, combined angle estimator augmented by coefficient W_0 ensures smaller error angle as shown in Fig 7.25 (b) and Fig 7.26 (b). It can be concluded that the weighted coefficient W_0 improves the performance of the combined angle estimator.
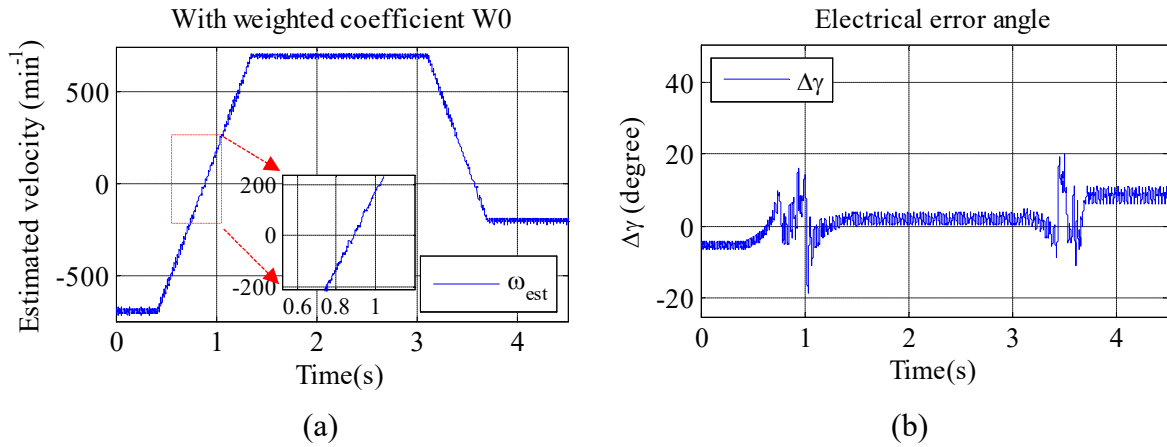
(a)

(b)

Fig 7.25. Combined angle estimator with weighted coefficient W_0: a) speed response; b) electrical error angle
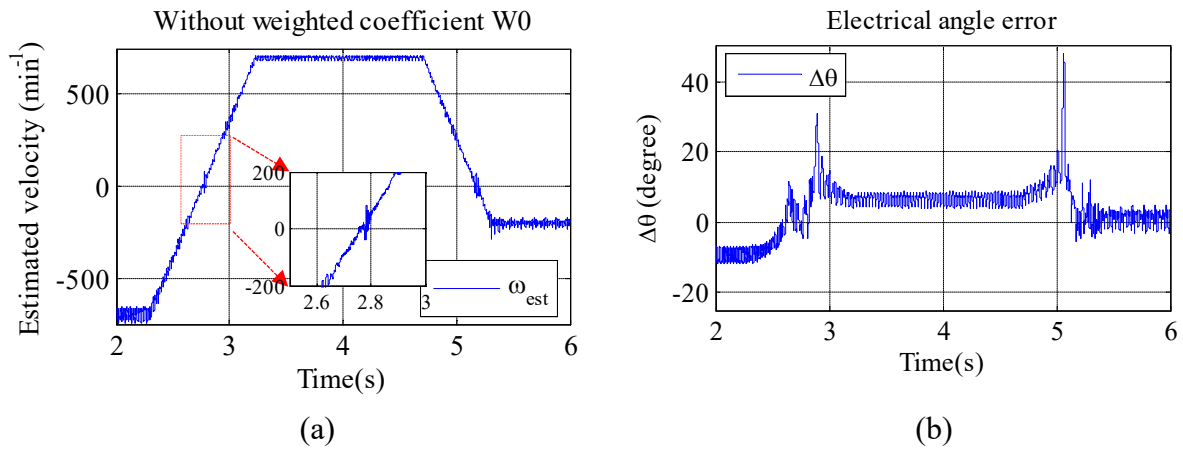

(a)

(b)

Fig 7.26. Combined angle estimator without weighted coefficient W_0: a) speed response; b) electrical error angle

7.6 Diagnosis of the bearing faults

Experiments on the detection of the bearing faults are conducted with two configurations of the electric drive: with and without the use of the mechanical encoder. Experiments with an encoder follow the diagnostic procedure presented in section 6.5, in which the load torque is estimated by applying either a sliding window method or a harmonic speed controller. In the sensorless drive, the rotor angle and rotor speed are provided by the field angle observer. Both single-point defects and generalized roughness of a ball bearing installed on the load side are taken into account. The horizontal slider-crank mechanism was driven at 60 min⁻¹. For practical purpose, the delta torque ΔT was represented in Fourier series with $f_n = 10\,Hz$ by taking a sample with a ten seconds length. The testing bearings are UBC-P205 bearings with the number of balls $z = 9$.

7.6.1 Diagnosis of the bearing faults with the conventional FOC and mechanical encoder

A. Outer raceway fault

The first step for any experiments on the detection of the bearing faults is the preparation of desirable faulty bearings. Fig 7.27 shows a bearing with an artificial defect on the outer raceway. A screw was inserted into a hole located on top of the bearing housing. It can go up or down to change the contact pressure with the bearing balls for getting a desirable faulty level. An acceleration sensor was mounted on the bearing housing to measure vibration velocity, which is used to classify the working condition of the bearing. The crank was detached from the coupling shaft. The location of the screw was set so that the RMS value of the vibration velocity is categorized in level C according to the ISO 10816 standard while the machine was operating at 1000 min^{-1} or 16.67 Hz. Fig 7.28 illustrates the RMS value of the vibration velocity corresponding to the emulated outer raceway fault.

Fig 7.29 shows the load torque, the estimated torque and the delta torque as time-dependent functions in case of healthy and outer faulty bearings. Fig 7.30 depicts the spectral representation of the delta torque ΔT after the FFT. The red line corresponds to the Fourier terms associated with the healthy bearing and acts as the reference line. The blue line refers to the faulty bearing.
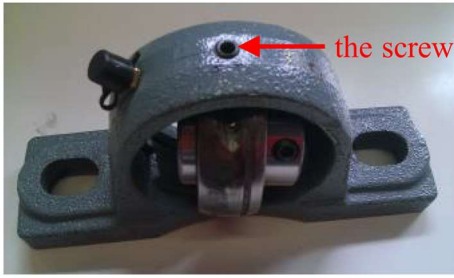
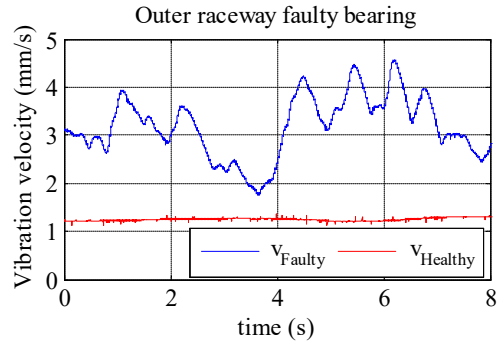Fig 7.27. Bearing with an outer raceway defect

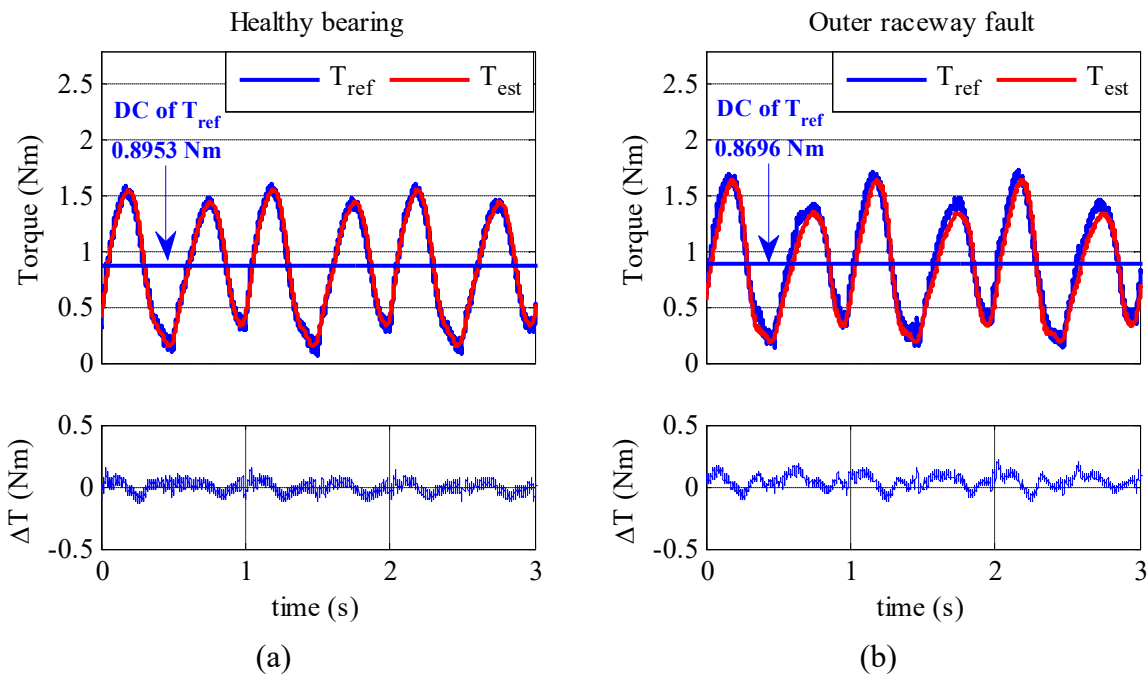Fig 7.28. Vibration velocity measurement

Fig 7.29. Load torque as time-dependent functions: a) healthy bearing: b) outer raceway faulty bearing

According to (6.18), the resulting fault frequency is:

$$f_{ORF} = 0.4 \cdot z \cdot f_n = 0.4 \cdot 9 \cdot 10\,Hz = 36Hz \tag{7.8}$$

At this frequency, Fig 7.30 shows a small but clear difference between the spectra. Furthermore, the deviations at the multiples of f_{ORF} ($72\,Hz, 108\,Hz, \dots$) are also indications of the fault. Generally, the signatures to detect the outer raceway fault can be observed at frequencies defined by $f_{ORF}^k = k \cdot f_{ORF}, k \in N^*$.

It can be concluded that the outer raceway fault was successfully detected by using the proposed method.
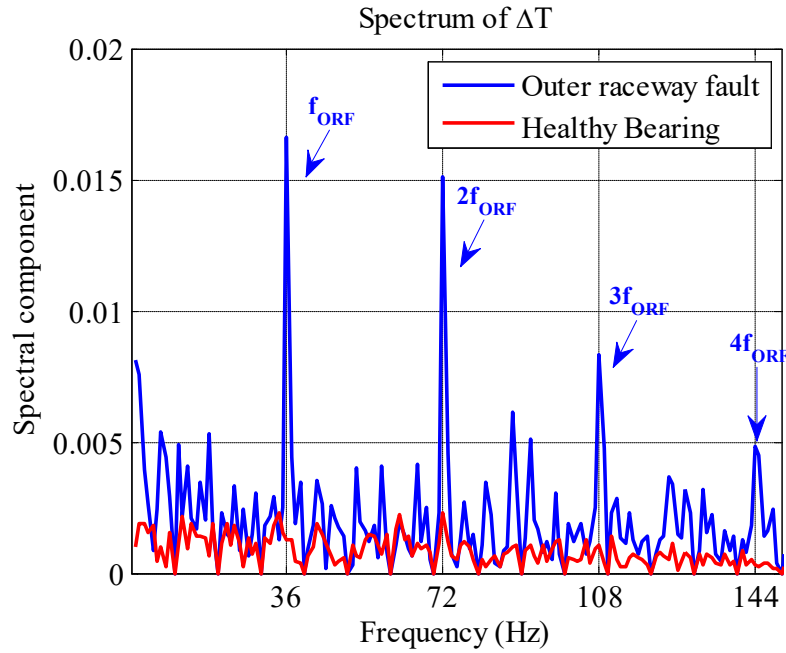
Fig 7.30. Spectrum of ΔT corresponding to the healthy and the faulty bearings

B. Inner raceway fault

In further experiments, the case of an inner raceway defect was researched. Fig 7.31 depicts the system designed for emulating defective bearing. The screw can move inside a hole in the coupling shaft to achieve an inner raceway defect. A gap of $6.5\ mm$ on the circumference of the inner raceway was removed to make sure that the screw can contact the bearing balls. The location of the screw was changed until the RMS value of the vibration velocity was in level C according to the ISO 10816 standard as it is shown in Fig 7.32.

The diagnostic procedure was conducted similarly to the diagnosis of the outer raceway defect. According to (6.19), the characteristic fault frequency is $f_{IRF} = 54\ Hz$. Fig 7.33 shows the load torque, the estimated torque, and the delta torque as time-dependent functions for the case of the defect on the inner raceway. It also shows the angular position of the crank, from which the position associated with the highest value of the load torque can be determined. In Fig 7.34, the Fourier spectrum of the delta torque corresponding to the faulty bearing is depicted in blue in comparison with the red reference spectrum. It can be observed that in addition to the characteristic fault frequency and its multiples $f_{IRF}^{k} = (54\ Hz, 108\ Hz\ ...)$, there are sidebands around these frequencies with the sideband width $\Delta f_{SB} = f_n = 10\ Hz$. The sideband frequencies are defined by (7.9).

$$f_{IRF}^{k,i} = \left| k \cdot f_{IRF} + i \cdot \Delta f_{SB} \right| = \left| k \cdot 54 + i \cdot 10 \right| Hz; \ k \in N^*, i \in Z^* \tag{7.9}$$
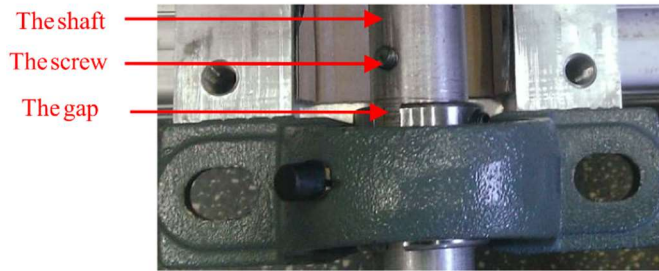

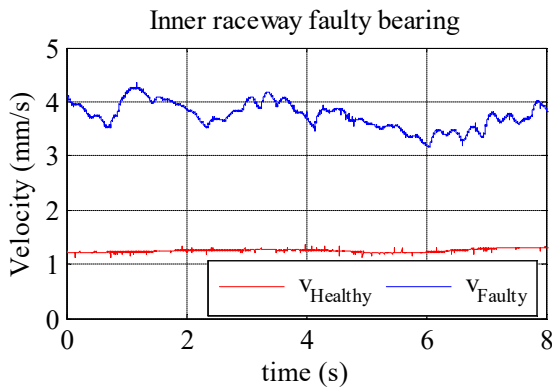Fig 7.31. bearing with an inner raceway defect
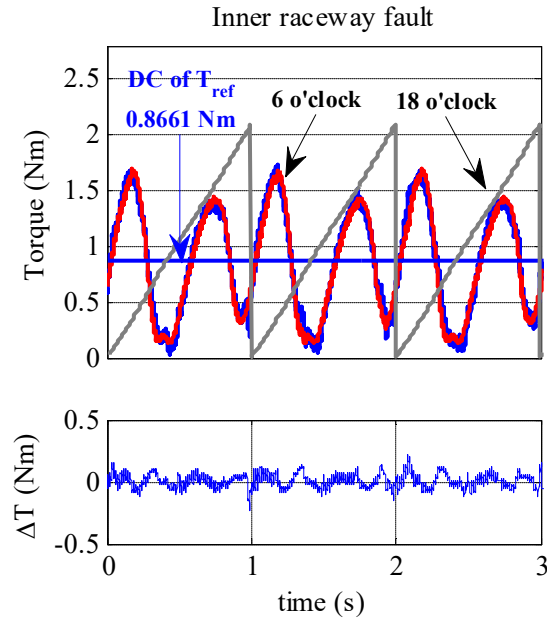

Fig 7.32. Vibration velocity measurement

Fig 7.33. Load torque as time-dependent functions and angular position of the crank in case of an inner raceway fault

As it was explained in section 6.4, the sidebands are caused by the load zone effect. In the horizontal slider-crank mechanism, the load applied to the bearing reaches the highest value when the crank stands at the position 6 o'clock and the second highest value at the position 18 o'clock as shown in Fig 7.33. The defect on the inner raceway rotates through the load zone once per revolution. As the fault intensity reaches the highest values twice per revolution (at the two aforementioned positions), the values of the coefficients corresponding to $i = 2$ (or more generally at any even values of i) are higher than those corresponding to other sideband frequencies.

From the clear signatures observed at the characteristic fault frequency and its multiples as well as the sideband effect, the inner raceway fault was successfully detected.
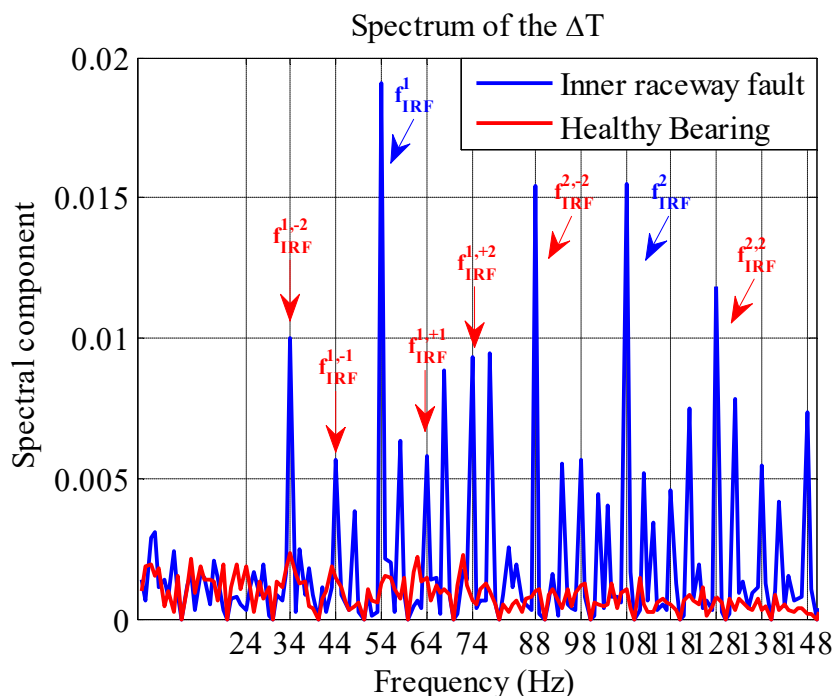

Fig 7.34. Spectrum of the delta torque

C.   Generalized roughness fault

To create a generalized roughness fault, some corundum was used to contaminate the bearing. This very hard material destroys the surface of the raceways and the bearing balls. As shown in Fig 7.35, a hole on the outer raceway and a hold on the bearing housing were created to make a path through which the corundum can enter the bearing. The results achieved by conducting the diagnostic method including the vibration velocity, the load torque, and the delta torque are shown in Fig 7.36 and Fig 7.37, respectively.

Fig 7.29(a) shows that the DC component of the load torque corresponding to the healthy bearing is 0.8696 Nm. Fig 7.37 illustrates that the DC component belonging to the generalized roughness bearing is 0.9655 Nm that exhibits an increase of 11% when compared to the healthy case. The DC component related to the outer and the inner raceway defects are 0.8953 Nm (difference of 2.9%) and 0.8661 Nm (difference of 0.4%) as they are shown in Fig 7.29(b), Fig 7.33, respectively. As expected, the increase of the DC component in the case of generalized roughness fault is much more significant than those in the case of single-point defects.

To make sure that the system was not affected by the corundum, the angular velocity was measured for the healthy and the faulty bearing. Fig 7.38 shows the crank angular velocity in both cases. It can be seen that there are no considerable differences between the speed responses, so the mechanism with the faulty bearing still works properly.

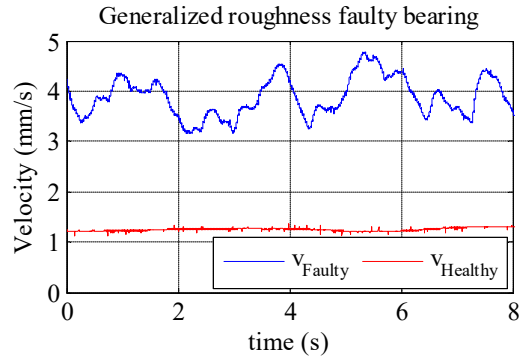Fig 7.35. Generalized roughness fault bearing

Fig 7.36. Vibration velocity measurement
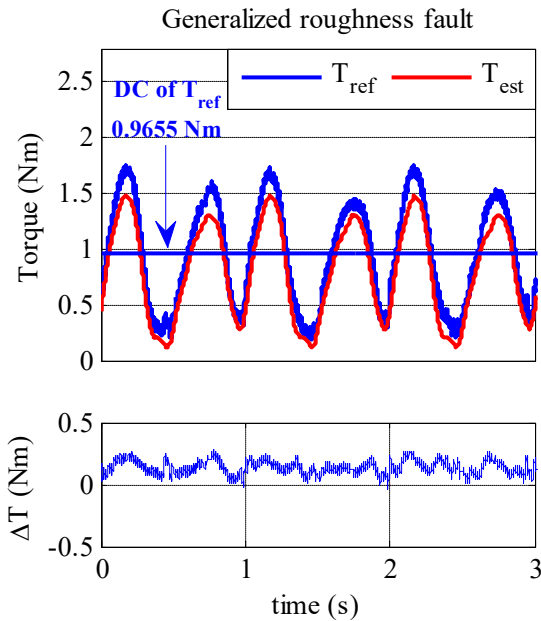
Fig 7.37. Load torque as time-dependent function in case of generalized roughness fault
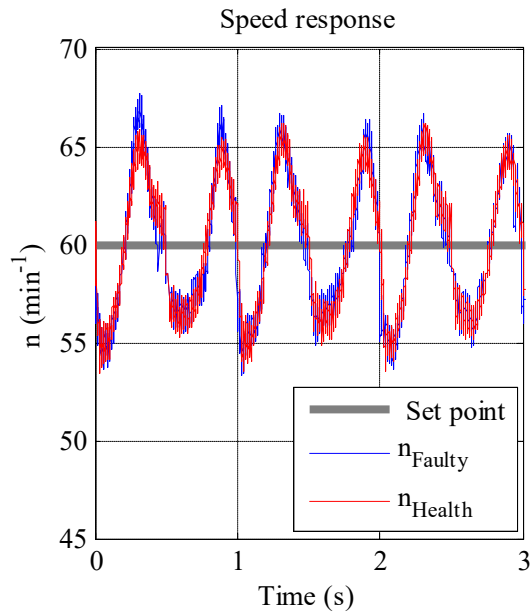
Fig 7.38. Speed responses with a healthy and a generalized roughness bearings

The broadband change caused by the generalized roughness fault is visible in Fig 7.39. The spectral line corresponding to the frequency $f = 36\ Hz$ is higher than others because of the effect of the hole on the outer raceway. This hole can be considered as a mild outer raceway fault. However, the faulty signature at the multiples of $f = 36\ Hz$ are not observed, so it cannot be classified as an outer raceway fault.

It can be concluded that the proposed diagnostic procedure can detect the generalized roughness fault in the ball bearing.
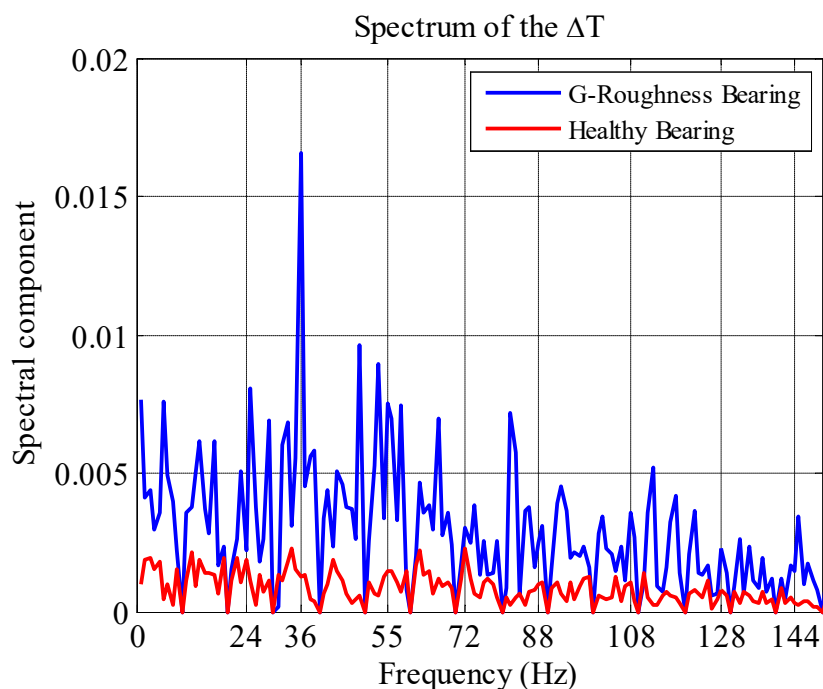
Fig 7.39. Spectrum of the delta torque

D. Spectrum analysis by using FFT with windowing

The three former experiments on the detection of the bearing faults were based on the FFT analysis, in which 10-second sampled signals corresponding to ten periods of the load torque were analyzed. Another way to get the spectrum of the delta torque is the use of a windowing method installed in a commercial oscilloscope [72]. The main advantage of the windowing method is the ability to work with any periods of the sampled signals.

The Fourier spectra corresponding to a healthy, an inner and an outer raceways faulty bearings are depicted in Fig 7.40(a),(b),(c), respectively. The conditions of the bearings are similar to those presented in section 7.6.1(A) and 7.6.1(B).
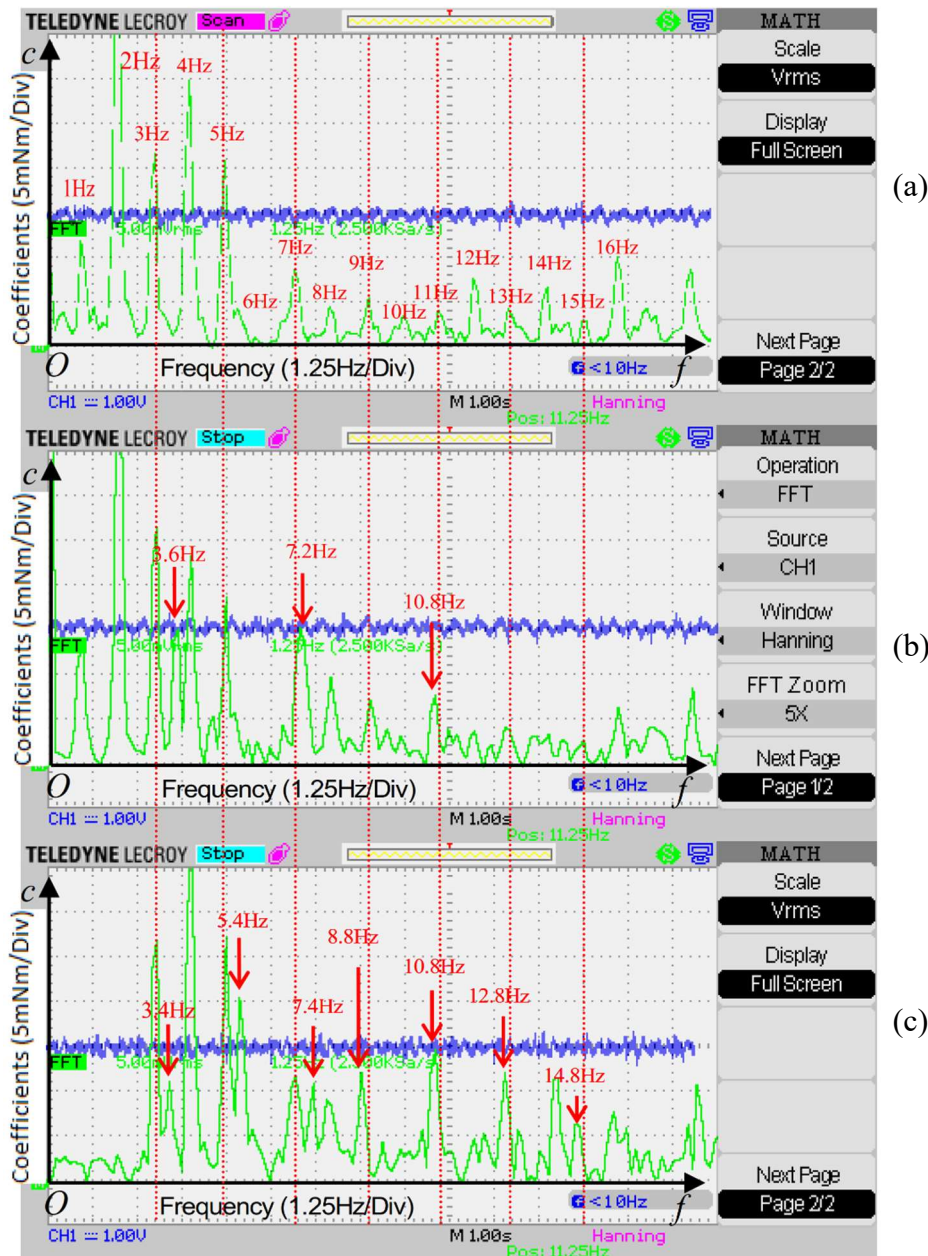
Fig 7.40. Delta torque (blue line) and its Fourier coefficients
(green line): a) healthy bearing; b) outer raceway faulty bearing; c)
inner raceway faulty bearing

The crank was also driven at 60 min^{-1}, or $f_n = 1\ Hz$. From (6.18), the characteristic fault frequency $f_{ORF} = 3.6\ Hz$. The spectrum belonging to the healthy bearing shown in Fig 7.40(a) serves as the baseline for the comparison to defective lines. Fig 7.40(b) clearly shows large differences between the two lines at f_{ORF} and its multiples. This phenomenon is similar to that as illustrated in Fig 7.30.

For the inner raceway defect $f_{IRF} = 5.4\ Hz$ is computed according to (6.19). Fig 7.40(c) shows that the coefficient related to f_{IRF} and its multiples are larger than those in the baseline. In addition, the sideband effect is also visibly recognized, especially at frequencies corresponding to $i = 2$ in (7.9). It can be concluded that the windowing method also provides a promising solution for the detection of the bearing fault. Both the single-point defects and generalized roughness fault in the bearing whose faulty level is located in level C according to the ISO 10816 standard can be detected.

### 7.6.2 Diagnosis of the bearing faults based on harmonic speed controller

As already mentioned, the harmonic speed controller brings an alternative solution for the load torque estimation. Fig 7.14 demonstrates the load torque estimation while healthy bearings were installed on either load side or motor side. The estimated load torque is used in the next experiment with the aim of detecting single-point defects. The preparation for desirable faulty bearings as well as the performance of the diagnostic procedure were conducted in a similar manner as it was presented in section 7.6.1.

Fig 7.41(a),(b),(c) show the load torque, the estimated torque and the delta torque corresponding to a healthy bearing, an outer raceway faulty bearing and an inner raceway faulty bearing. The spectra of the delta torque corresponding to the three bearings are illustrated in Fig 7.43 and Fig 7.43. It can be seen in Fig 7.43 that the outer raceway fault can be detected as there are significant differences between the baseline and the faulty line observed at the outer raceway characteristic fault frequency $f_{ORF} = 36\ Hz$ and its multiples. The results coincide with those illustrated in Fig 7.30. Furthermore, the inner raceway defect can also be detected by analyzing the spectra shown in Fig 7.43. In addition to the clear differences at the inner characteristic fault frequency and it multiples $f_{IRF}^k = (54\ Hz, 108\ Hz\ ...)$, the sideband effects are also noticeable.

In summary, the single-point bearing defects were successfully detected by the identification of the load torque based on the harmonic speed controller.
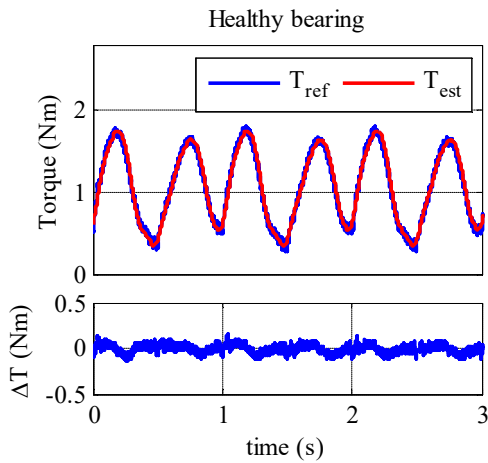
(a)
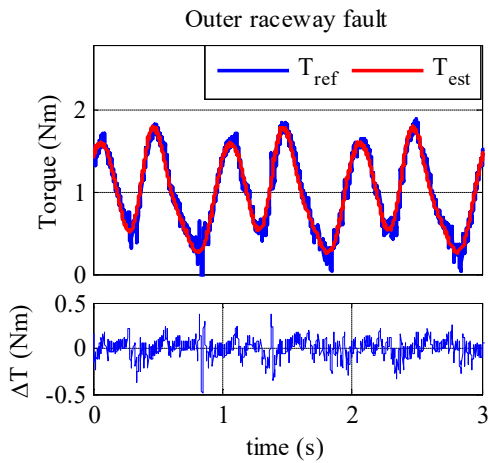
(b)
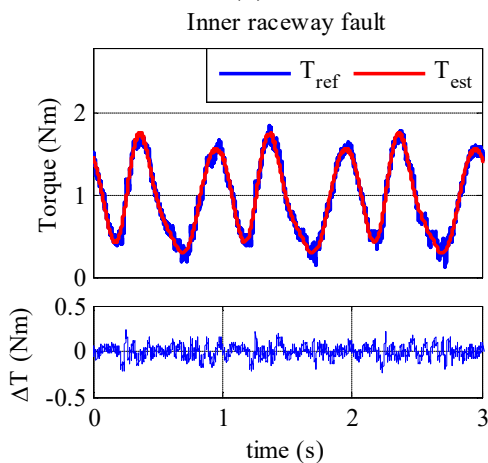
(c)

Fig 7.41. Reference torque, estimated torque, delta torque corresponding to: a) a healthy bearing; b) an outer raceway faulty bearing; c) and an inner raceway faulty bearing
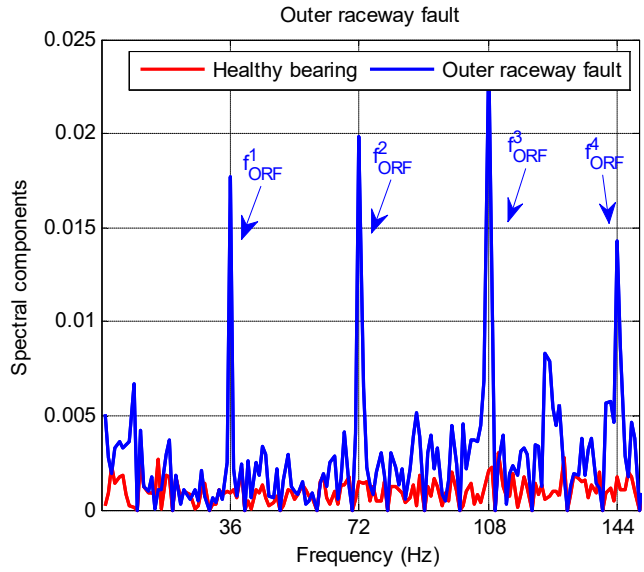
Fig 7.42 Spectrum of the delta torque corresponding to a healthy bearing and an outer raceway faulty bearing
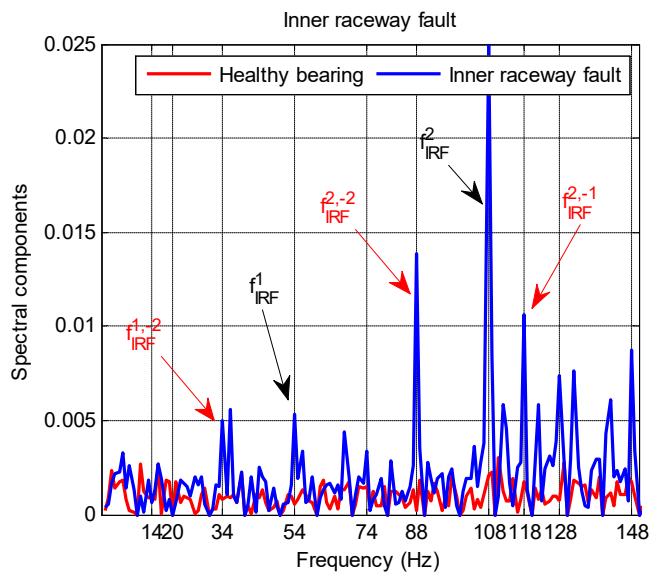
Fig 7.43. Spectrum of the delta torque corresponding to a healthy bearing and an inner raceway faulty bearing

7.6.3 Diagnosis of the bearing faults based on sensorless control of the drive

The last experiment is related to the detection of the bearing faults by using the sensorless control of the drive. The load torque utilized in the diagnostic procedure is obtained by conducting a sensorless harmonic speed control [73].

To prepare the desirable faulty bearings, the combined field angle estimator was used to drive the PMSM at the high speed region. Fig 7.44(a) shows the speed response at 1000 min^{-1}. Fig 7.44(b) illustrates the vibration velocity measured on the housing of the bearing with an artificial outer raceway defect. The RMS value of the vibration velocity shows that the faulty bearing is in level C according to the ISO 10816 standard.
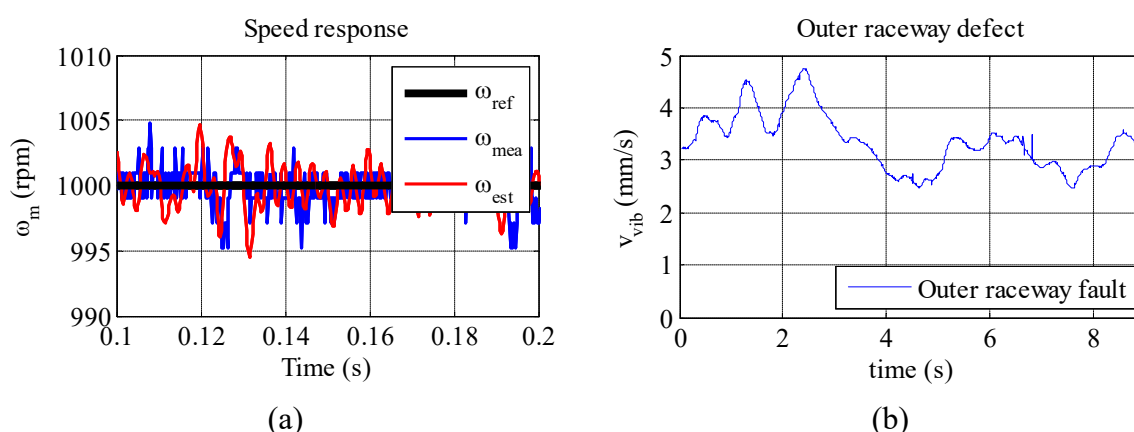
Fig 7.44. High-speed sensorless control for the electric drive: a) speed response in the steady state; b) vibration velocity with an outer raceway faulty bearing

In Fig 7.45, the reference torque, the estimated torque, and the delta torque corresponding to a healthy bearing, an outer raceway faulty bearing, and an inner raceway faulty bearing are presented. The spectra of the delta torque corresponding to the outer raceway and inner raceway faulty bearings are depicted in Fig 7.46 and Fig 7.47, respectively. It can be seen that the spectra have rich harmonics because of the reference load torque ripples originated from the ripples of the estimated speed. However, signatures for the diagnosis of the outer and of the inner raceway defects are still visible and detectable at the characteristic fault frequencies and its multiples.

Fig 7.46. The spectrum of the delta torque corresponding to a healthy bearing and an outer raceway faulty bearing
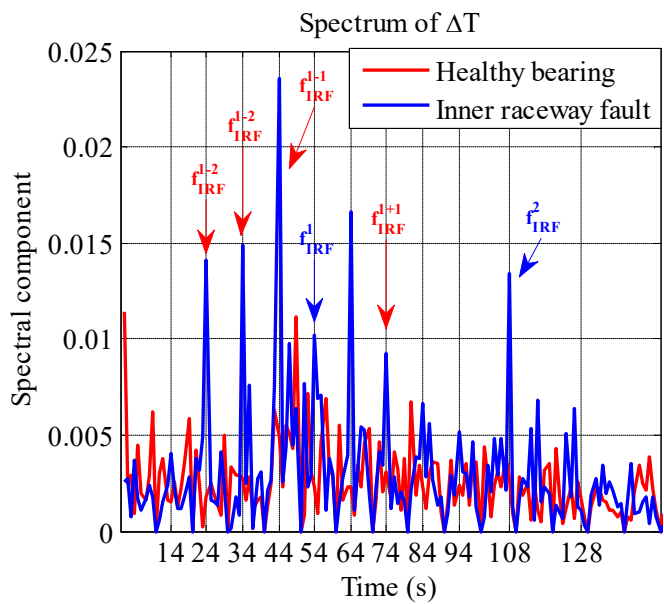
Fig 7.47. The spectrum of the delta torque corresponding to a healthy bearing and an inner raceway faulty bearing.

Fig 7.45. Reference torque, estimated torque and delta torque: a) healthy bearing; b) outer raceway faulty bearing; c) inner raceway faulty bearing

7.7   Summary of the chapter

In this chapter, the theoretical analysis and proposals for the optimization of the electric drive and the diagnosis of the bearing faults in a slider-crank mechanism were validated.

The first experiment was dedicated toward the load torque estimation, from which the estimated load torque can be used in a feed-forward control scheme to improve the speed response quality or in a diagnostic procedure to detect the presence of bearing faults. The three most commonly found types of the bearing faults were successfully detected, including the outer raceway defect, the inner raceway defect, and the generalized roughness fault.

Harmonic speed control for the improvement of the speed response quality was tested. It was proven that both the PI-R speed controller and the harmonic speed controller can enhance the reference speed tracking possibility of the drive.

The last experiment concerning the sensorless control of the drive was conducted. Experimental results show that the PMSM can be driven at low-speed region, including standstill, as well as high-speed region by following the injection technique and the enhanced voltage model, respectively. The harmonic speed control and the diagnosis of the bearing faults were also confirmed with the sensorless control of the drive.

8 Conclusions

The main objective of the present work was the identification of the production cycle of drives for the purpose of optimal control and of the diagnosis of mechanical failures. The new ideas are related to the two methods for the load torque estimation, the procedure for the detection of the bearing faults and the use of harmonic control for the speed control loop. To implement and to improve the proposed methods, a sensorless operation of the drive was developed and evaluated.

In the first step, the load torque in a horizontal slider-crank mechanism, an example of repetitive mechanical systems, was identified by using Fourier interpolation. The estimation of the load torque was conducted via the evaluation of the Fourier coefficients by applying either a phenomenological method or an empirical look-up table based method. The estimated load torque can be used for two purposes. First, it was added to the output of the speed controller and acted as a compensation signal in a feed-forward control scheme. It was successfully proven that the load torque compensation improved the speed response quality not only in the steady state but also in the dynamic mode. Subsequently, the estimated load torque was used in a new approach for the detection of the bearing faults. As the load torque contains information of the characteristic fault frequencies associated with each type of the bearing faults, the spectrum analysis of the load torque can be used as an indicator for the presence of the faults. Both single-point defects and generalized roughness, the two most commonly failures found in bearing of industrial installations, were successfully diagnosed by the proposed method. In addition, the diagnostic procedure does not require any additional sensors.

Besides the load torque compensation for the improvement of the speed response qualities, harmonic control is an alternative solution. In such method, each harmonic in the speed error can be manipulated by an individual controller. It can be a resonant part in case of PI-R speed controller or a PI controller in case of harmonic speed controllers. In either cases, experiments showed that the reference speed tracking was improved by considerably canceling the speed oscillation originated from the cyclic load torque.

The final experiments were extended to the operation of the system without the use of an angular transducer used for the measurement of the rotor angle and rotor speed. The sensorless control for the PMSM was implemented in a wide speed range, in which a

combined field angle estimator was proposed to drive smoothly the machine between the low-speed and the high-speed regions. The ideas on the load torque estimation, the bearing fault detection, and the harmonic control were successfully experimentally validated in the sensorless control of the drive.

9 Appendix

9.1 Parameters of the PMSM

Table 9.1. Parameters of the driven machine

Parameters	Value	Unit
Machine Model	ABB SDM 101-005N8-115	
Nominal Power	1.54	kW
Nominal Voltage	360	V
Nominal Velocity	3000	min^{-1}
Nominal Torque	4.9	Nm
Number of pole Pairs	3	
Winding Resistance R_{UV}	6.4	Ω
Winding Inductance L_{UV}	21.8	mH
Moment of Inertia	0.0006	$kg \cdot m^2$

9.2 Kinetic analysis of the horizontal slider-crank mechanism

The moment of inertia of the horizontal slider-crank mechanism referred to the shaft of the driven machine can be obtained from the kinetic energy analysis.

(a)
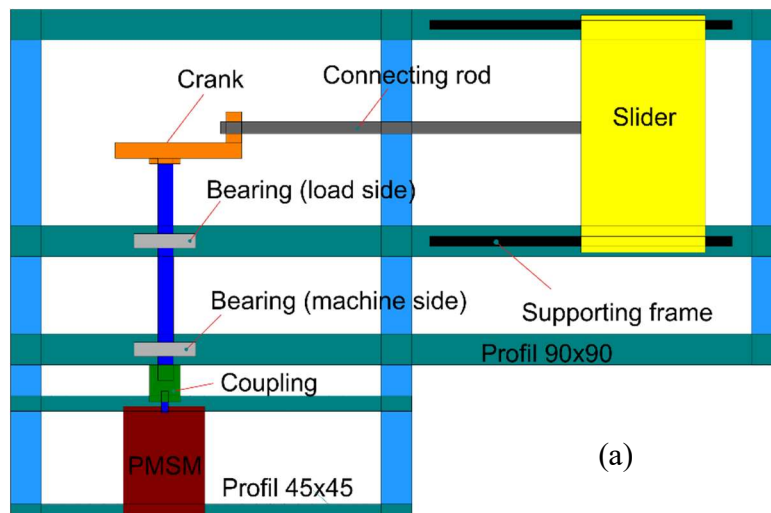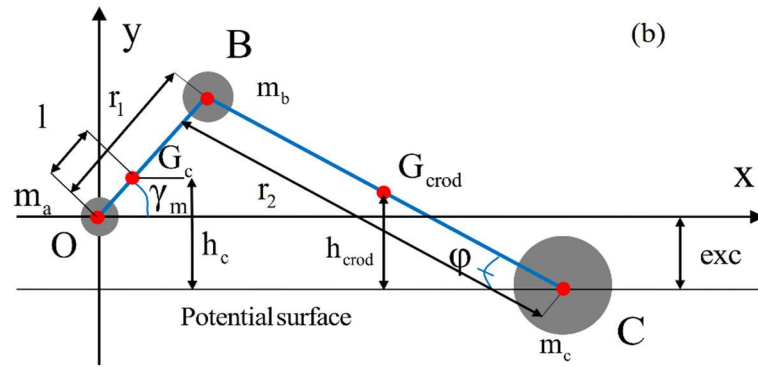
Fig 9.1. Horizontal slider-crank mechanism: a) mechanical structure; b) reduced model

The parameters of the mechanism are given in the following table:

Table 9.2. Parameters of the slider-crank mechanism

Name	Symbol	Values
Mass of the crank	m_{crank}	$0.345\ kg$
Mass of the connecting rod	m_{crod}	$0.229\ kg$
Mass of the slider	m_{slider}	$4.295\ kg$
OB	r_1	$50\ mm$
BC	r_2	$340\ mm$
OG	l	$13.5\ mm$
Distance from x-axis to the sliding surface	exc	$30\ mm$

The masses in the reduced model depend on the masses in the mechanism. A detail calculation procedure for the equivalent masses in the reduced model can be found in [74].

$$m_a = \frac{4}{5} \cdot m_{crank}$$

$$m_b = \frac{1}{5} \cdot m_{crank} + \frac{1}{2} \cdot m_{crod} \tag{9.1}$$

$$m_c = \frac{1}{2} \cdot m_{crod} + m_{slider}$$

where m_{crank}, m_{crod}, and m_{slider} are the masses of the crank, the connecting rod, and the slider, respectively.

Denoting $\dot{x} = dx/dt$ the derivation with respect to time of variable x, the total kinetic energy is given by:

$$E_k = \frac{1}{2} \cdot m_b \cdot \left(r_1 \cdot \dot{\gamma}_m \right)^2 + \frac{1}{2} m_c \left(\dot{x}^2 + \dot{y}^2 \right)^2 \tag{9.2}$$

where $(x; y)$ is the position of mass m_c in the Oxy coordinate system.

Since mass m_c moves on the horizontal axis, its vertical position is time-independent. As a result, the following equation holds:

$$\dot{y} = 0 \tag{9.3}$$

Geometric relations associated with the reduced model ensure:

$$x = r_1 \cdot \cos \gamma_m + r_2 \cdot \cos \varphi \tag{9.4}$$

$$r_2 \cdot \sin \varphi = r_1 \cdot \sin \gamma_m + exc \tag{9.5}$$

The expression of φ can be obtained from (9.5)

$$\varphi = \arcsin \frac{r_1 \cdot \sin \gamma_m + exc}{r_2} = \arcsin \left(\lambda \cdot \sin \gamma_m + k \right) \tag{9.6}$$

with $= r_1/r_2; k = exc/r_2$.

The derivation of equations (9.4) and (9.6) yields:

$$
\begin{aligned}
\dot{x} &= -r_1 \cdot \dot{\gamma}_m \cdot \sin \gamma_m - r_2 \cdot \dot{\varphi} \cdot \sin \varphi \\
&= -r_1 \cdot \dot{\gamma}_m \cdot \sin \gamma_m - r_2 \cdot \left(\lambda \cdot \sin \gamma_m + k \right) \frac{\lambda \cdot \dot{\gamma}_m \cdot \cos \gamma_m}{\sqrt{1 - \left(\lambda \cdot \sin \gamma_m + k \right)^2}} \\
&= -r_1 \cdot \Omega_m \cdot \left[\sin \gamma_m + \cos \gamma_m \cdot \frac{\left(\lambda \cdot \sin \gamma_m + k \right)}{\sqrt{1 - \left(\lambda \cdot \sin \gamma_m + k \right)^2}} \right]
\end{aligned}
\tag{9.7}
$$

where $\Omega_m = d\gamma_m/dt$.

Let $u = (\lambda \cdot sin\gamma_m + k)$. A function $f(u)$ is defined as:

$$f(u) = \frac{u}{\sqrt{1-u^2}} \tag{9.8}$$

Normally $\lambda \ll 1$ and $k \ll 1$, therefore $(\lambda \cdot sin\gamma_m + k) \ll 1$. Therefore, the function $f(u)$ can be approximated by a Taylor series around zero:

$$f(u) = f(0) + f'(u)\big|_{u=0} \cdot (u-0) + 0(u) \approx u \tag{9.9}$$

By substituting (9.9) into (9.7), the time derivation of x can be calculated as:

$$
\begin{aligned}
\dot{x} &= -r_1 \cdot \Omega_m \cdot \left[\sin\gamma_m + \cos\gamma_m \cdot (\lambda \cdot \sin\gamma_m + k) \right] \\
&= -r_1 \cdot \Omega_m \cdot \left[\sin\gamma_m + \frac{1}{2}\lambda \cdot \sin 2\gamma_m + k \cdot \cos\gamma_m \right]
\end{aligned}
\tag{9.10}
$$

Combining (9.2), (9.3) and (9.10), the kinetic energy is given by:

$$E_k = \frac{1}{2} \cdot m_b \cdot r_1^2 \cdot \Omega_m^2 + \frac{1}{2} \cdot m_c \cdot r_1^2 \cdot \Omega_m^2 \cdot \left(\sin\gamma_m + \frac{1}{2} \cdot \lambda \cdot \sin 2\gamma_m + k \cdot \cos\gamma_m \right)^2 \tag{9.11}$$

The reduced moment of inertia of the mechanism $J_{mechanism}$ is defined as:

$$E_k = \frac{1}{2} \cdot J_{mechanism} \cdot \Omega_m^2 \tag{9.12}$$

By comparing (9.11) and (9.12), the moment of inertia of the mechanism referred to the shaft of the driven machine is:

$$J_{mechanism} = m_b \cdot r_1^2 + m_c \cdot r_1^2 \cdot \left(\sin\gamma_m + \frac{1}{2} \cdot \lambda \cdot \sin 2\gamma_m + k \cdot \cos\gamma_m \right)^2 \tag{9.13}$$

If terms related to the multiplication of the two small constants λ and k are ignored while simplifying (9.13), the reduced moment of inertia is finally defined by:

$$J_{mechanism}(\gamma_m) = m_b \cdot r_1^2 + m_c \cdot r_1^2 \cdot \left(\sin^2\gamma_m + \lambda \cdot \sin\gamma_m \cdot \sin 2\gamma_m + 2 \cdot k \cdot \sin\gamma_m \cdot \cos\gamma_m \right) \tag{9.14}$$

9.3   Derivations of the load torque components

Under the assumption that the crank is operated at a constant angular velocity, the load torque demanded by the slider-crank mechanism contains three components, including the torque due to the change of inertia, the potential energy, and the friction forces:

$$T_{load} = \frac{1}{2} \cdot \frac{dJ_{total}}{d\gamma_m} \cdot \left(\frac{d\gamma_m}{dt} \right)^2 + \frac{dW_p}{d\gamma_m} + F_{total} \cdot \frac{dx_{slider}}{d\gamma_m} \tag{9.15}$$

9.3.1   The inertia torque

The torque due to the change of inertia is defined by:

$$T_{inertia} = \frac{1}{2} \cdot \frac{dJ_{total}}{d\gamma_m} \cdot \left(\frac{d\gamma_m}{dt} \right)^2 \tag{9.16}$$

where J_{total} is given by (9.14) and $\Omega_m = d\gamma_m / dt = const.$

The inertia torque can be determined by the following equation:

$$T_{inertia} = \frac{1}{2} \cdot m_c \cdot r_1^2 \cdot \left(\sin 2\gamma_m - \frac{1}{2} \cdot \lambda \cdot \sin \gamma_m + \frac{3}{2} \cdot \lambda \cdot \sin 3\gamma_m + 2 \cdot k \cdot \cos 2\gamma_m \right) \cdot \Omega_m^2 \tag{9.17}$$

9.3.2   The potential torque

The potential torque comes from the change of the potential energy with respect to the shaft angle of the driven machine:

$$T_p = \frac{dW_p}{d\gamma_m} \tag{9.18}$$

where W_p is defined by (5.4).

$$T_p = \frac{dW_p}{d\gamma_m} = \frac{d}{d\gamma_m} \left[m_{crank} \cdot g \cdot (l \cdot \sin \gamma_m + exc) + m_{crod} \cdot g \cdot \frac{1}{2} \cdot (r_1 \cdot \sin \gamma_m - exc) \right]$$
$$= \left(m_{crank} \cdot l + \frac{1}{2} \cdot m_{crod} \cdot r_1 \right) \cdot g \cdot \cos \gamma_m \tag{9.19}$$

9.3.3   The friction torque

Friction forces, including the Coulomb friction and the viscous friction, contribute a significant component to the load torque. The component is named friction torque and given by:

$$T_{fric} = F_{total} \cdot \frac{dx_{slider}}{d\gamma_m} = \left[K_c \cdot \text{sgn}\left(v_{slider}\right) + K_v \cdot v_{slider} \right] \frac{dx_{slider}}{d\gamma_m} \tag{9.20}$$

The velocity of the slider v_{slider}, or the time-derivative of the position, is given in (9.10).

$$v_{slider} = -r_1 \cdot \Omega_m \cdot \left(\sin\gamma_m + \frac{1}{2}\lambda \cdot \sin 2\gamma_m + k \cdot \cos\gamma_m \right) \tag{9.21}$$

In addition, the following equation is hold:

$$\frac{dx_{slider}}{d\gamma_m} = \frac{dx_{slider}}{dt} \cdot \frac{dt}{d\gamma_m} = -r_1 \cdot \Omega_m \cdot \left(\sin\gamma_m + \frac{1}{2}\lambda \cdot \sin 2\gamma_m + k \cdot \cos\gamma_m \right) \cdot \frac{1}{\Omega_m}$$

$$= -r_1 \cdot \left(\sin\gamma_m + \frac{1}{2}\lambda \cdot \sin 2\gamma_m + k \cdot \cos\gamma_m \right) \tag{9.22}$$

By combining (9.20), (9.21) and (9.22), the friction torque is composed of two terms. One is due to the Coulomb friction, and the other is because of the viscous friction.

$$T_{fric} = T_{Coulomb} + T_{viscous} \tag{9.23}$$

where

$$T_{Coulomb} = K_c \cdot r_1 \cdot \left| \sin\gamma_m + \frac{1}{2}\lambda \cdot \sin 2\gamma_m + k \cdot \cos\gamma_m \right| \tag{9.24}$$

$$T_{viscous} = K_v \cdot r_1^2 \cdot \Omega_m^2 \left(\sin\gamma_m + \frac{1}{2}\lambda \cdot \sin 2\gamma_m + k \cdot \cos\gamma_m \right)^2 \tag{9.25}$$

10 References

[1] K. Ohnishi, M. Shibata, und T. Murakami, „Motion control for advanced mechatronics", *IEEEASME Trans. Mechatron.*, Bd. 1, Nr. 1, S. 56–67, März 1996.

[2] Z. Q. Zhu und D. Howe, „Electrical Machines and Drives for Electric, Hybrid, and Fuel Cell Vehicles", *Proc. IEEE*, Bd. 95, Nr. 4, S. 746–765, Apr. 2007.

[3] S. Nandi, H. A. Toliyat, und X. Li, „Condition monitoring and fault diagnosis of electrical motors-a review", *IEEE Trans. Energy Convers.*, Bd. 20, Nr. 4, S. 719–729, Dez. 2005.

[4] R. R. Schoen, T. G. Habetler, F. Kamran, und R. G. Bartfield, „Motor bearing damage detection using stator current monitoring", *IEEE Trans. Ind. Appl.*, Bd. 31, Nr. 6, S. 1274–1279, Nov. 1995.

[5] J. R. Stack, T. G. Habetler, und R. G. Harley, „Fault classification and fault signature production for rolling element bearings in electric machines", in *4th IEEE International Symposium on Diagnostics for Electric Machines, Power Electronics and Drives, 2003. SDEMPED 2003*, 2003, S. 172–176.

[6] H. Zoubek, S. Villwock, und M. Pacas, „Frequency Response Analysis for Rolling-Bearing Damage Diagnosis", *IEEE Trans. Ind. Electron.*, Bd. 55, Nr. 12, S. 4270–4276, Dez. 2008.

[7] J. R. Stack, T. G. Habetler, und R. G. Harley, „Fault signature modeling and detection of inner race bearing faults", in *2005 IEEE International Conference on Electric Machines and Drives*, 2005, S. 271–277.

[8] S. E. Saarakkala und M. Hinkkanen, „Identification of two-mass mechanical systems in closed-loop speed control", in *IECON 2013 - 39th Annual Conference of the IEEE Industrial Electronics Society*, 2013, S. 2905–2910.

[9] I. C. Baik, K. H. Kim, und M. J. Youn, „Robust nonlinear speed control of PM synchronous motor using adaptive and sliding mode control techniques", *IEE Proc. - Electr. Power Appl.*, Bd. 145, Nr. 4, S. 369–376, Juli 1998.

[10] Y. Hori, H. Iseki, und K. Sugiura, „Basic consideration of vibration suppression and disturbance rejection control of multi-inertia system using SFLAC (state feedback and load acceleration control)", *IEEE Trans. Ind. Appl.*, Bd. 30, Nr. 4, S. 889–896, Juli 1994.

[11] N. Matsui, T. Makino, und H. Satoh, „Auto-compensation of torque ripple of DD motor by torque observer", in *, Conference Record of the 1991 IEEE Industry Applications Society Annual Meeting, 1991*, 1991, S. 305–311 Bd.1.

[12] D. Pavkovic, J. Deur, und I. Kolmanovsky, „Adaptive Kalman Filter-Based Load Torque Compensator for Improved SI Engine Idle Speed Control", *IEEE Trans. Control Syst. Technol.*, Bd. 17, Nr. 1, S. 98–110, Jan. 2009.

[13] T. Shi, Z. Wang, und C. Xia, „Speed Measurement Error Suppression for PMSM Control System Using Self-Adaption Kalman Observer", *IEEE Trans. Ind. Electron.*, Bd. 62, Nr. 5, S. 2753–2763, Mai 2015.

[14] S. E. Saarakkala und M. Hinkkanen, „State-Space Speed Control of Two-Mass Mechanical Systems: Analytical Tuning and Experimental Evaluation", *IEEE Trans. Ind. Appl.*, Bd. 50, Nr. 5, S. 3428–3437, Sep. 2014.

[15] ISO Standard 10816, „Mechanical Vibration-Elavuation of Machine Vibration by Measurement on Non-Rotating Parts- Part 3". .

[16] J. R. Stack, T. G. Habetler, und R. G. Harley, „Bearing fault detection via autoregressive stator current modeling", *IEEE Trans. Ind. Appl.*, Bd. 40, Nr. 3, S. 740–747, Mai 2004.

[17] J. Holtz, „Developments in Sensorless AC Drive Technology", in *2005 International Conference on Power Electronics and Drives Systems*, 2005, Bd. 1, S. 9–16.

[18] V. Berinberg und F. Götz, „Enhanced Voltage Model for Sensorless Control of a Permanent Magnet Synchronous Motor Drive". SPS IPC Drives, 2008.

[19] R. B. Sepe und J. H. Lang, „Real-time observer-based (adaptive) control of a permanent-magnet synchronous motor without mechanical sensors", *IEEE Trans. Ind. Appl.*, Bd. 28, Nr. 6, S. 1345–1352, Nov. 1992.

[20] Y.-D. Yoon, S.-K. Sul, S. Morimoto, und K. Ide, „High-Bandwidth Sensorless Algorithm for AC Machines Based on Square-Wave-Type Voltage Injection", *IEEE Trans. Ind. Appl.*, Bd. 47, Nr. 3, S. 1361–1370, Mai 2011.

[21] J. Holtz, „Acquisition of Position Error and Magnet Polarity for Sensorless Control of PM Synchronous Machines", *IEEE Trans. Ind. Appl.*, Bd. 44, Nr. 4, S. 1172–1180, Juli 2008.

[22] A. Piippo, M. Hinkkanen, und J. Luomi, „Sensorless control of PMSM drives using a combination of voltage model and HF signal injection", in *Conference Record of the 2004 IEEE Industry Applications Conference, 2004. 39th IAS Annual Meeting*, 2004, Bd. 2, S. 964–970 Bd.2.

[23] K. P. Kovacs und I. Racz, *Transiente Vorgänge in Wechselstrommaschinen*. Budapest: Verlag der Ungerishcen Akademie der Wissenschaften, 1959.

[24] J. Stepina, „Raumzeiger als Grundlage der Theorie der elektrischen Maschinen", *Electrotechnische Zeitschrift ETZ-A Archiv Bd.8*, S. 584–588, 1967.

[25] L. Serrrano-Lribarnegaray, „Ersetzen der Mathematischen durch die Physikalischen Raumzeiger zur Untersuchung stationärer und dynamischer Vorgänge in rotierenden elektrischen Maschinen", *ETZ Archiv Bd.8*, S. 347–352, 1986.

[26] J. Puranen, *Induction motor versus permanent magnet synchronous motor in motion control applications: a comparative survey*, Ph.D Thesis. Finland: Lappeenranta University of Technology, 2006.

[27] N. P. Quang und J.-A. Dittrich, *Vector Control of Three-Phase AC Machine*. Berlin, Heidelberg: Springer, 2008.

[28] R. C. Dorf, *The Engineering Handbook, Second Edition*. CRC Press, 2004.

[29] P. M. P. Palma, *Finite Set Model Predictive Control of the PMSM with Sine-Wave Filter*, Ph.D Thesis. Siegen-Germany: University of Siegen, 2015.

[30] F. Blaschke, „Das Prinzip der Feldorientierung, Grundlage für die Transvektor-Regelung von Drehfeldmaschinen", *Siemens-Zeischrift 45*, S. 757–760, 1971.

[31] K. Hasse, „Zum Dynamischen Verhalten der Asynchronmaschine bei Betrieb mit variabler Ständerspannung", *ETZ- Band 89*, S. 77–81, 1968.

[32] C. Grabner, „Conceptual Design of Power Electronics, Control Strategies and Electrical Machines within Variable Speed Drives", *Eng. Lett.*, Nov. 2008.

[33] J. W. Umland und M. Safiuddin, „Magnitude and symmetric optimum criterion for the design of linear control systems: what is it and how does it compare with the others?", *IEEE Trans. Ind. Appl.*, Bd. 26, Nr. 3, S. 489–497, Mai 1990.

[34] „Permanent Magnet Synchronous and Brushless DC Motor Drives", *CRC Press*, 25-Sep-2009. [Online]. Verfügbar unter: https://www.crcpress.com/Permanent-Magnet-Synchronous-and-Brushless-DC-Motor-Drives/Krishnan/p/book/9780824753849. [Zugegriffen: 25-Juli-2017].

[35] K. C. Phong, *Magnetic guidance for linear drives*, PhD Dissertation. Darmstadt, Germany: Technical university of Darmstadt, 2011.

[36] L. Harnefors, S. E. Saarakkala, und M. Hinkkanen, „Speed Control of Electrical Drives Using Classical Control Methods", *IEEE Trans. Ind. Appl.*, Bd. 49, Nr. 2, S. 889–898, März 2013.

[37] R. Teodorescu, F. Blaabjerg, U. Borup, und M. Liserre, „A new control structure for grid-connected LCL PV inverters with zero steady-state error and selective

harmonic compensation", in *Nineteenth Annual IEEE Applied Power Electronics Conference and Exposition, 2004. APEC '04*, 2004, Bd. 1, S. 580–586 Vol.1.

[38] H. Qin und J. W. Kimball, „Closed-Loop Control of DC #x2013;DC Dual-Active-Bridge Converters Driving Single-Phase Inverters", *IEEE Trans. Power Electron.*, Bd. 29, Nr. 2, S. 1006–1017, Feb. 2014.

[39] R. Teodorescu, F. Blaabjerg, M. Liserre, und P. C. Loh, „Proportional-resonant controllers and filters for grid-connected voltage-source converters", *IEE Proc. - Electr. Power Appl.*, Bd. 153, Nr. 5, S. 750–762, Sep. 2006.

[40] V. T. Phung und M. Pacas, „Harmonic Speed Control for Repetitive Mechanical Systems", in *PCIM Europe 2017; International Exhibition and Conference for Power Electronics, Intelligent Motion, Renewable Energy and Energy Management*, 2017, S. 1–8.

[41] U. A. Miranda, L. G. B. Rolim, und M. Aredes, „A DQ Synchronous Reference Frame Current Control for Single-Phase Converters", in *2005 IEEE 36th Power Electronics Specialists Conference*, 2005, S. 1377–1381.

[42] J. Kloeck und W. Schumacher, „Harmonic current control for transverse flux machines", in *Renewable Energy and Energy Management; Proceedings of PCIM Europe 2014; International Exhibition and Conference for Power Electronics, Intelligent Motion*, 2014, S. 1–8.

[43] S. Bolognani, L. Tubiana, und M. Zigliotto, „Extended Kalman filter tuning in sensorless PMSM drives", *IEEE Trans. Ind. Appl.*, Bd. 39, Nr. 6, S. 1741–1747, Nov. 2003.

[44] R. Dhaouadi, N. Mohan, und L. Norum, „Design and implementation of an extended Kalman filter for the state estimation of a permanent magnet synchronous motor", *IEEE Trans. Power Electron.*, Bd. 6, Nr. 3, S. 491–497, Juli 1991.

[45] S. Bolognani, R. Oboe, und M. Zigliotto, „Sensorless full-digital PMSM drive with EKF estimation of speed and rotor position", *IEEE Trans. Ind. Electron.*, Bd. 46, Nr. 1, S. 184–191, Feb. 1999.

[46] T. Aihara, A. Toba, T. Yanase, A. Mashimo, und K. Endo, „Sensorless torque control of salient-pole synchronous motor at zero-speed operation", *IEEE Trans. Power Electron.*, Bd. 14, Nr. 1, S. 202–208, Jan. 1999.

[47] S. Feuersänger und M. Pacas, „Sensorless control with online parameter adaption for the PMSM", in *IECON 2011 - 37th Annual Conference of the IEEE Industrial Electronics Society*, 2011, S. 2012–2017.

[48] J.-H. Jang, J.-I. Ha, M. Ohto, K. Ide, und S.-K. Sul, „Analysis of permanent-magnet machine for sensorless control based on high-frequency signal injection", *IEEE Trans. Ind. Appl.*, Bd. 40, Nr. 6, S. 1595–1604, Nov. 2004.

[49] M. Linke, R. Kennel, und J. Holtz, „Sensorless position control of permanent magnet synchronous machines without limitation at zero speed", in *IECON 02 [Industrial Electronics Society, IEEE 2002 28th Annual Conference of the]*, 2002, Bd. 1, S. 674–679 Bd.1.

[50] J.-H. Jang, S.-K. Sul, J.-I. Ha, K. Ide, und M. Sawamura, „Sensorless drive of surface-mounted permanent-magnet motor by high-frequency signal injection based on magnetic saliency", *IEEE Trans. Ind. Appl.*, Bd. 39, Nr. 4, S. 1031–1039, Juli 2003.

[51] D. Nguyen, R. Dutta, und M. F. Rahman, „Investigation of sensorless direct torque control using high frequency injection apply to a fractional-slot concentrated winding interior PMSM", in *2013 IEEE 10th International Conference on Power Electronics and Drive Systems (PEDS)*, 2013, S. 1312–1317.

[52] H. Dresig und F. Holzweißig, *Dynamics of Machinery*. Berlin, Heidelberg: Springer Berlin Heidelberg, 2010.

[53] K. K. Mohindroo, *Basic Principles of Physics*. Pitambar Publishing, 1997.

[54] I. Claudiu, I. Faycal, und R. Jose, *Identification of a system with dry friction*. IOC-DT-P-2005-20, 2005.

[55] C. T. Johnson und R. D. Lorenz, „Experimental identification of friction and its compensation in precise, position controlled mechanisms", *IEEE Trans. Ind. Appl.*, Bd. 28, Nr. 6, S. 1392–1398, Nov. 1992.

[56] K. K. Tan, T. H. Lee, S. N. Huang, und X. Jiang, „Friction modeling and adaptive compensation using a relay feedback approach", *IEEE Trans. Ind. Electron.*, Bd. 48, Nr. 1, S. 169–176, Feb. 2001.

[57] Armstrong-Hétlouvry B., P. Dupont, und C. Canudas de Wit, „A survey of models, analysis tools and compensation methods for the control of machines with friction". Automatica, 1994.

[58] Y. Kligerman und M. Varenberg, „Elimination of Stick-Slip Motion in Sliding of Split or Rough Surface", *Tribol. Lett.*, Bd. 53, Nr. 2, S. 395–399, Feb. 2014.

[59] R. Isermann, *Identifikation dynamischer Systeme 2*. Berlin, Heidelberg: Springer Berlin Heidelberg, 1992.

[60] S. D. Ochoa, *Diagnosis of Rotor Asymmetries in Inverter Fed Induction Machine*, Ph.D Thesis. Siegen-Germany: University of Siegen, 2012.

[61] V. T. Phung und M. Pacas, „Load Torque Estimation in Repetitive Mechanical Systems by Using Fourier Interpolation", in *PCIM Europe 2016; International Exhibition and Conference for Power Electronics, Intelligent Motion, Renewable Energy and Energy Management*, 2016, S. 1–8.

[62] „ISO 15:2011 - Rolling bearings: Radial bearings, Boundary dimensions, general plan", *ISO*, März-2011. [Online]. Verfügbar unter: http://www.iso.org/iso/catalogue_detail.htm?csnumber=55216. [Zugegriffen: 07-Okt-2016].

[63] NTN Global, „Classification and Characteristics of Rolling Bearings". .

[64] R. Stribeck, „Ball Bearings for Various Loads", *Cent. Lab. Sci. Tech. Investig. Transl. KW Van Treuren Al*, Nr. 420–463.

[65] Fred B. Oswald, Erwin V. Zaretsk, und Joseph V. Poplawski, „Effect of Internal Clearance on Load Distribution and Life of Radially Loaded Ball and Roller Bearings", *NASATM—2012-217115*, Nr. 65th Annual Meeting and Exhibition sponsored by the Society of Tribologists and Lubrication Engineers (STLE), S. 1–39, Apr. 2012.

[66] Barden precision bearings, „Bearing Failures: Causes and Cures". .

[67] R. R. Obaid, T. G. Habetler, und J. R. Stack, „Stator current analysis for bearing damage detection in induction motors", in *4th IEEE International Symposium on Diagnostics for Electric Machines, Power Electronics and Drives, 2003. SDEMPED 2003*, 2003, S. 182–187.

[68] R. Rubini und U. Meneghetti, „Application of the envelope and wavelet transform analyses for the diagnosis of incipient faults in ball bearings", *Mech. Syst. Signal Process.*, Bd. 15, Nr. 2, S. 287–302, März 2001.

[69] B. Li, M. Y. Chow, Y. Tipsuwan, und J. C. Hung, „Neural-network-based motor rolling bearing fault diagnosis", *IEEE Trans. Ind. Electron.*, Bd. 47, Nr. 5, S. 1060–1069, Okt. 2000.

[70] M. E. H. Benbouzid, „A review of induction motors signature analysis as a medium for faults detection", in *Proceedings of the 24th Annual Conference of the IEEE Industrial Electronics Society, 1998. IECON '98*, 1998, Bd. 4, S. 1950–1955 Bd.4.

[71] V. T. Phung und M. Pacas, „Detection of bearing faults in repetitive mechanical systems by identification of the load torque", in *2016 IEEE 8th International Power Electronics and Motion Control Conference (IPEMC-ECCE Asia)*, 2016, S. 3089–3095.

[72] S. Petre und M. Randolph, *SPECTRAL ANALYSIS OF SIGNALS*. New Jersey: Prentice Hall, 2005.

[73] V. T. Phung und M. Pacas, „Sensorless harmonic speed control and detection of bearing faults in repetitive mechanical systems", in *2017 IEEE 3rd International Future Energy Electronics Conference and ECCE Asia (IFEEC 2017 - ECCE Asia)*, 2017, S. 1646–1651.

[74] A. Ghosh und A. K. Mallik, *Theory of Mechanisms and Machines*. Affiliated East-West Press, 1988.